AD/A-007 070

DESIGN STUDY FOR A SENSOR UTILIZING AN ELECTROSTATIC CAMERA. VOLUME II, APPENDICES

Richard O. Johnson, et al

CBS Laboratories

Prepared for:

Space and Missile Systems Organization
Advanced Research Projects Agency

December 1974

DESIGN STUDY FOR A SENSOR UTILIZING AN ELECTROSTATIC CAMERA

SAMSO TR 75-36
VOLUME II
APPENDICES

Robert A. Botticelli
Richard O. Johnson
Daniel Galburt
et al

CBS Laboratories, A Division
of CBS, Inc.

December, 1974

Sponsored by: Advanced Research Projects Agency
ARPA Order No. 2643

DEPARTMENT OF THE AIR FORCE
HEADQUARTERS SPACE AND MISSILE SYSTEMS ORGANIZATION (AFSC)
LOS ANGELES AIR FORCE STATION, P.O. BOX 92960
WORLDWAY POSTAL CENTER
LOS ANGELES, CALIFORNIA 90009

NOTICE

When Government drawings, specifications, or other data are used for any purpose other than in connection with a definitely related Government procurement operation, the United States Government thereby incurs no responsibility nor any obligation whatsoever; and the fact that the government may have formulated, furnished, or in any way supplied the said drawings, specifications, or other data, is not to be regarded by implication or otherwise as in any manner licensing the holder or any other person or corporation, or conveying any rights or permission to manufacture, use, or sell any patented invention that may be related thereto.

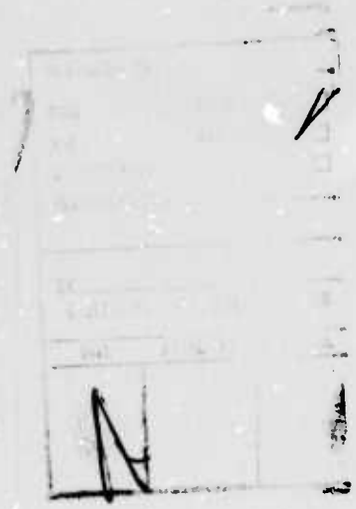

Copies of this report should not be returned unless return is required by security considerations, contractual obligations, or notice on a specific document.

DESIGN STUDY FOR A SENSOR

UTILIZING AN ELECTROSTATIC CAMERA

SAMSO TR 75-36
VOLUME II

APPENDICES

ARPA Order Number:	2643
Program Code Number:	4E20
Contract Number:	F04701-74-C-0262
Name of Contractor:	CBS Laboratories, a Division of CBS, Inc.
Effective Date of Contract:	74 Feb. 18
Contract Expiration Date:	74 Dec. 31
Short Title of Work:	Design Study for a Sensor Utilizing an Electrostatic Camera

Principal Investigators: Richard O. Johnson
Daniel N. Galburt
Phone No.: (203) 327-2000

Project Engineer: Robert A. Botticelli
Phone No.: (203) 327-2000

FOREWORD

This research was jointly supported by the Advanced Research Projects Agency of the Department of Defense and Space and Missile Systems Organization, Air Force Systems Command, under Contract F04701-74-C-0262. The research was conducted by CBS Laboratories, a Division of CBS, Incorporated, Stamford, Connecticut, under Project 5076, "Design Study for a Sensor Utilizing an Electrostatic Camera". The Electron Optics Branch, headed by Mr. Frank Cook of the Applied Physics Department, was responsible for the effort. The principal investigator for CBS Laboratories was Mr. Robert A. Botticelli, senior project engineer.

The authors acknowledge the assistance of Dr. Holger Luther, Gerald Wallmark, Thomas Lynch, Bruce Mathews, and Michael Antico for their help in carrying out the experimental work and design analysis presented in this report.

The research was started in February 1974, and was completed in December 1974.

Warren M Lee.

WARREN M. LEE, Capt., USAF
Project Officer/DYAJ/31737
Space Surveillance Program

(Unclassified) ABSTRACT

A sensor utilizing an electrostatic storage camera is studied for use in an autonomous space surveillance system. The Teal Amber I target and background parameters and search fan are used to characterize the system sensitivity and data acquisition method. A detailed telescope and mount analysis and camera design analysis are performed based on both panoramic and step-and-stare scan modes. A conceptual design of a data processing system utilizing starfield cancellation followed by streak detection is analyzed. The system survivability and reliability are discussed. A cost-effective laboratory demonstration system is presented. The recommended space surveillance system is described and performance predictions are made based on the Teal Amber target parameters.

TABLE OF CONTENTS

APPENDIX I

PERKIN-ELMER

ELECTRO-OPTICAL DIVISION
NORWALK, CONNECTICUT

REPORT NO. 11984

TEAL AMBER I

FINAL REPORT

PREPARED FOR

CBS LABORATORIES

DATE: 26 JULY 1974

TABLE OF CONTENTS

TABLE OF CONTENTS (Continued)

LIST OF ILLUSTRATIONS

LIST OF ILLUSTRACTIONS (Continued)

SECTION 1

INTRODUCTION

Perkin-Elmer has been engaged in a study program for a large aperture telescope and gimbal assembly dedicated to satellite detection. The primary system investigator of the TEAL-AMBER program is CBS, under whom Perkin-Elmer is subcontracted. This report summarizes the conclusions reached during the course of study. Investigations were concentrated in two areas: (1) a gimbal design that allows the telescope to scan the appropriate pattern in the heavens and (2) a telescope design that focuses light from solar illuminated satellites on to the CBS camera.

Both of the above functions have requirements that differ from those of a standard astronomical telescope. Specifically: (1) The gimbal must scan the telescope at rates of degrees per second in a saw tooth oscillation motion with a constant velocity varying less than 1 part in 10,000; and (2) the telescope must be a very fast optical system (faster than f/1.5) with a large FOV (degrees) and high resolution (arc-second) over a considerable spectral bandwidth.

This report offers a preferred telescope gimbal system design for the TEAL-AMBER application and describes the various approaches that were explored during the course of the investigation. Details are included in the appendices.

SECTION II

SYSTEM SCANNING APPROACHES

2.1 SYSTEM SCANNING APPROACHES

2.1.1 Preferred Scan Pattern

The basic requirement of the gimbal system is to continuously scan (not in discrete steps) the telescope's FOV through a volume in space that includes the intersection of the equatorial plane and the sphere descriptive of the satellites of interest. This is shown in Figure 1. The motion at the telescope will, of course, cause the image of stars and the solar illuminated satellite to move with respect to coordinates fixed in the telescope.

If the image is recorded or detected on a media that is driven in unison with the moving image, there would be no degradation in the image quality due to unwanted motion of the real image relative to the recorded image. Therefore, the degrees of freedom permitted in the focal plane determine the scan patterns that can be achieved without image motion. In the TEAL-AMBER I camera, only one degree of motion is permitted in the focal plane, and this limits the scan volume to those whose optical axis describes a great circle on the celestial sphere. The proof of this statement can be found later in this report (see paragraph 2.1.3). Having determined that only great circles can be scanned, one must consider how to implement such a scan; there are two obvious methods -- move the entire telescope or move a mirror in front of a stationary telescope. Both concepts are discussed in the subsequent sections and the conclusion reached is that moving the telescope is simpler.

2.1.2 Image Motion in the Focal Plane

Figure 2 shows a recording medium or detector on rollers in the focal plane of the telescope. A coordinate system is assumed (fixed in the focal plane) with one axis parallel to the roller axis. Three in-plane image

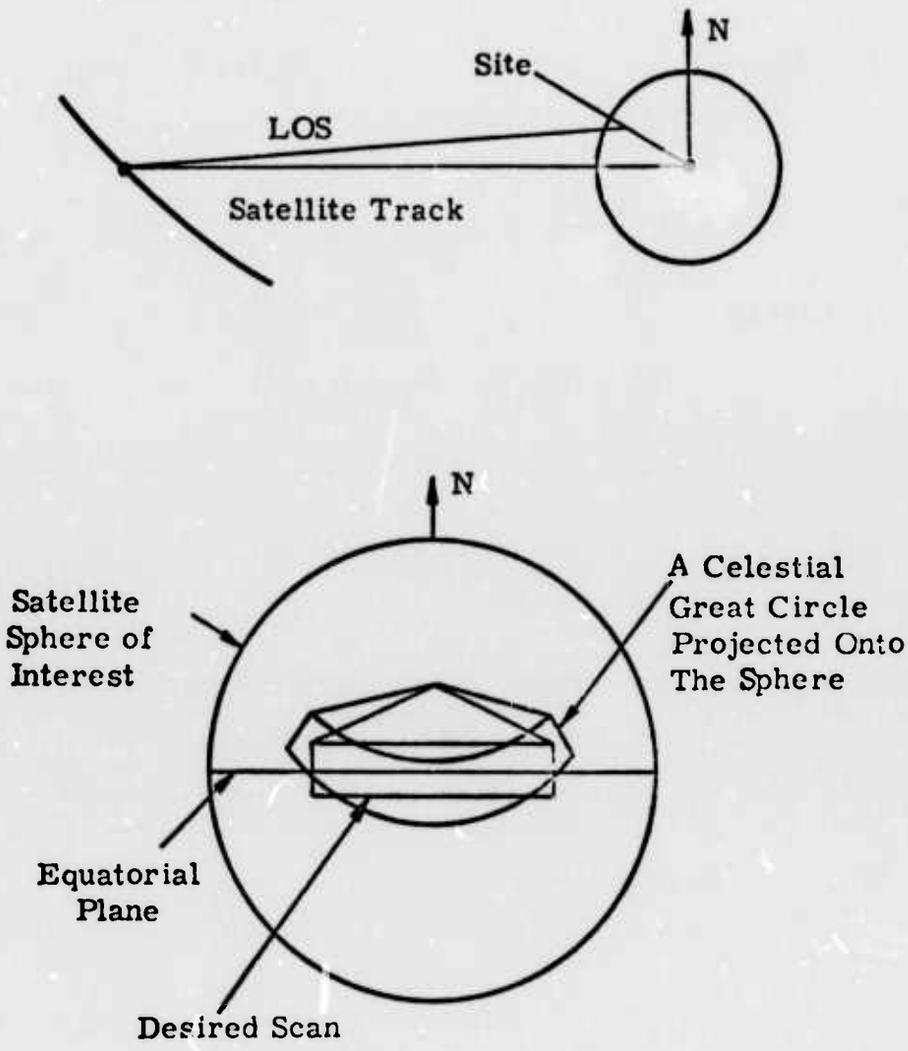

Figure 1. Preferred Scan Pattern

POSSIBLE IN-PLANE IMAGE MOTIONS RELATIVE
TO ROLLER AXIS REFERENCE

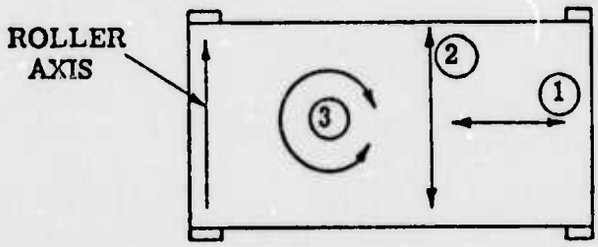

TYPE 1 CAN BE COMPENSATED BY BELT MOTION AROUND THE ROLLERS

TYPE 2 WOULD REQUIRE TRANSVERSE ROLLER MOTION WHICH IS ASSUMED TO BE UNAVAILABLE

TYPE 3 WOULD REQUIRE IN-PLANE BELT DISTORTION AND IS THEREFORE NOT ACCEPTABLE

Figure 2. Possible In-Plane Image Motions Relative to Roller Axis Reference

motions are possible: (1) parallel to the roller axis (2) normal to the roller axis, and (3) rotation relative to the roller axis. The medium could be moved in unison with the first two by rotation of the rollers and by roller translation along the roller axis, respectively.

The third motion, image rotation, cannot be compensated because the detector would be required to simultaneously have different velocities in different parts of the field. This is not possible with a rigid, translating detector.

It is also true that roller translation is not available as an option. Therefore, the only image motion allowable is motion normal to the roller axis. It is important to remember that the coordinate system, in which this statement is true, has one axis parallel to the roller axis.

2.1.3 Coverage Limitations

Figure 3 shows the detector and focal-plane rollers projected through the telescope onto the celestial sphere. If the projected focal plane is scanned over the sphere, image motions will result. If image motion is restricted to displacement normal to the rollers, as described above, the projected optic axis must remain in-plane and the rollers must remain normal to the scan plane. Any deviations from the scan pattern will result in unwanted image motion as follows:

a. Optical axis moves out of plane → image motion along-roller axis.

b. Roller axis not normal to scan plane → image motion along roller axis.

c. Roller axis angle not constant → image rotation relative to rollers. (This problem is discussed in Appendix B for the particular scan implementation concept.)

Therefore, if it is desired that the telescope scan a series of targets (e.g., stars) that do not happen to lie on a great circle on the celestial sphere, the transverse field width will have to be large enough to capture all of the desired targets during a scan.

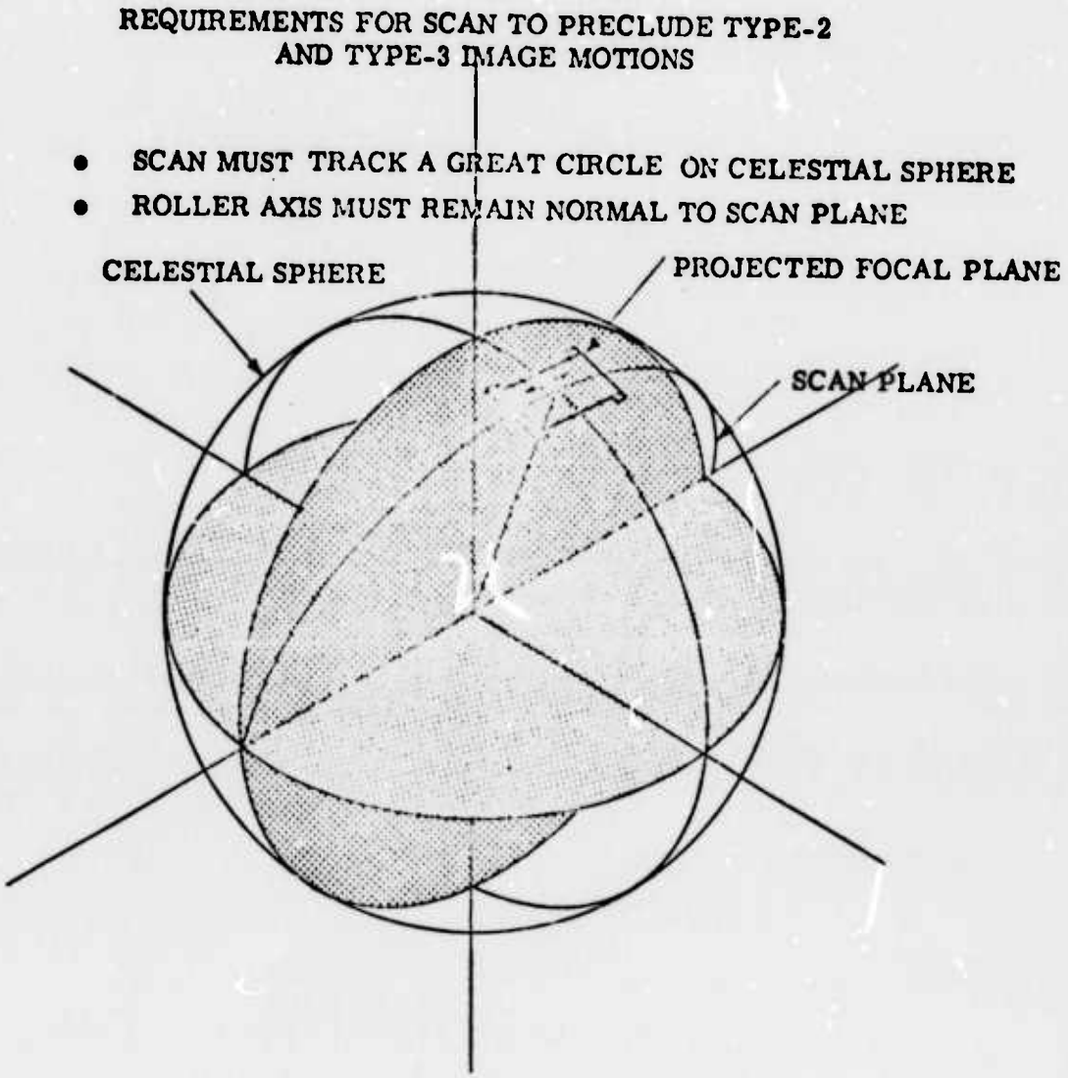

Figure 3. Detector and Focal Plane Rollers

This also means that if a particular satellite orbit is to be scanned, in general, it will not be possible to keep the orbit centralized in the FOV. This is because, in general, the satellite track on the celestial sphere, when viewed from a point on the earth's surface, will not be a great circle.

Note that these restrictions on coverage are a result of the image motion compensations available. If, for instance, the detector could be translated along the roller axis, paths other than the great circle could be tracked as long as the detector was wide enough to remain in the field. Note also that the coverage restrictions discussed above are independent of the mechanism used to procedure the scan motion.

2.1.4 Other Parameters

In addition to the scanning geometry, there exist other constraints on the gimbal systems. These constraints are dependent on the total system design and were supplied by CBS. The table below lists the additional requirements.

Axis	Total Rotation	Scan Rate
Scan	±75°	1/4 to 5° deg/sec
Elevation	±30°	1/4 to 1°
Polar	±15° (for sidereal correction)	15 arc-sec/sec

The scan axis must be capable of a slew rate and damping such that the retrace time is less than 10 seconds. Retrace time is the time to go from the scan velocity at the end of scan to the scan velocity at the beginning of scan. In other words, it includes slew time, velocity changing time and damping.

2.2 IMPLEMENTING THE SCAN MOTION

2.2.1 Gimbal Scan

The simplest way to scan the optic-axis so that it remains in-plane is to rotate the telescope about a gimbal axis normal to the optic axis. As long as the gimbal axis is fixed in the celestial sphere, i.e.,

inertial space, the optic-axis will scan a plane as desired. For a ground-based telescope, a second gimbal axis would be required to cancel the rotation of the earth so that the scan axis will remain fixed in the celestial sphere as required.

Such a two-axis system would permit scanning of a limited portion of the heavens. However, addition of a third axis would enable the telescope to scan any great circle desired. Therefore, three gimbal axes represent the minimum required to provide complete sky coverage. Figure 4 shows a three-gimbal system that would provide complete sky coverage from any earth site with earth-rate compensation.

2.2.2 Mirror Scan

The required scan motion could also be accomplished using an earth-fixed telescope and a flat scanning mirror that would deflect the optic-axis as desired. Figure 5 shows how this is done.

At any instant, the mirror-normal is positoned so that it bisects the angle between the desired position of the optic axis and its actual position. Of course this requires complete freedom to point the mirror normal in any desired direction. This means that two degrees of freedom, i.e., gimbal axes, will be needed on the mirror. The effect of earth-rate is to move the telescope slowly in inertial space. As long as this motion is accounted for in the computation of the desired positon of the mirror, earth rotation will be compensated automatically. Figure 5 shows that, in order to keep the reflected roller axis oriented properly (always normal to the scan plane), the roller assembly and detector must rotate about the optic axis.

To accomplish an in-plane scan of constant velocity requires simultaneous rotation about the two mirror axes and the optic axis. The equations of motion involve trigonometric functions dictating nonconstant velocities for mirror and telescope rotation. These equations are developed in Appendix A.

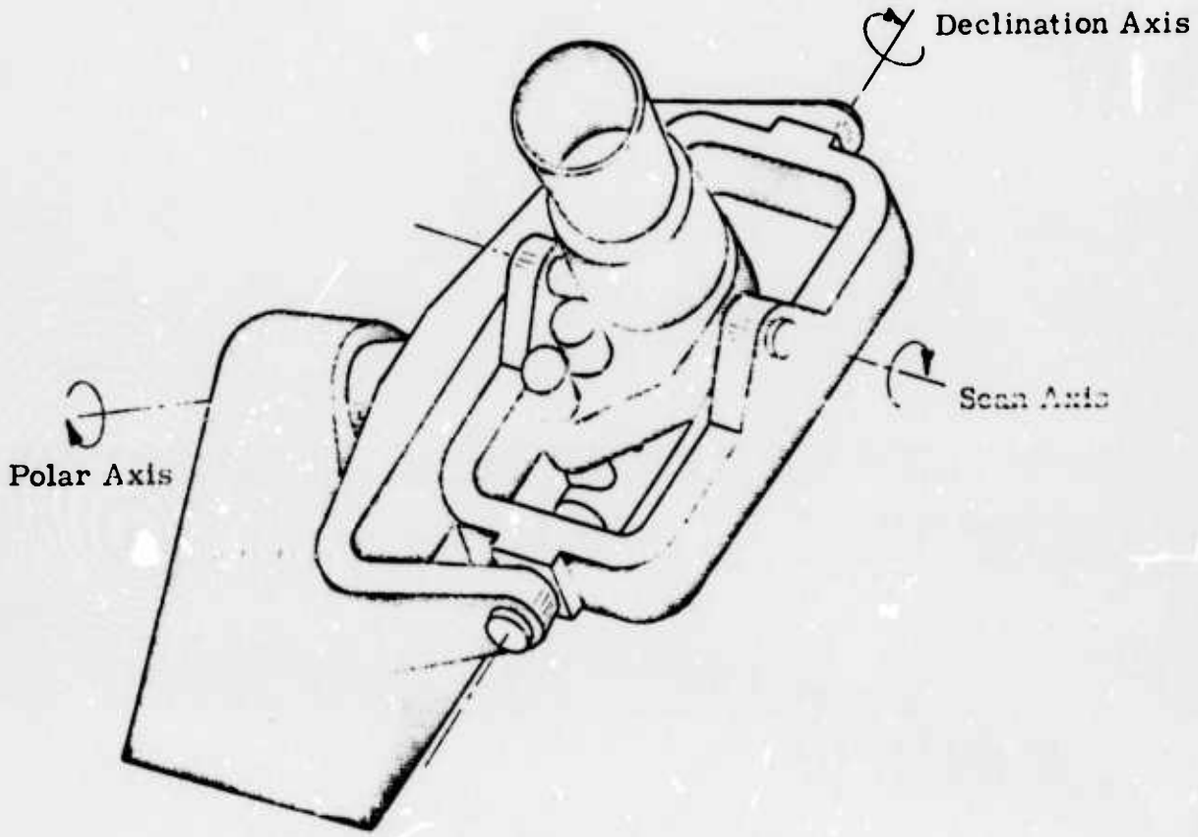

Figure 4. Three-Gimbal System

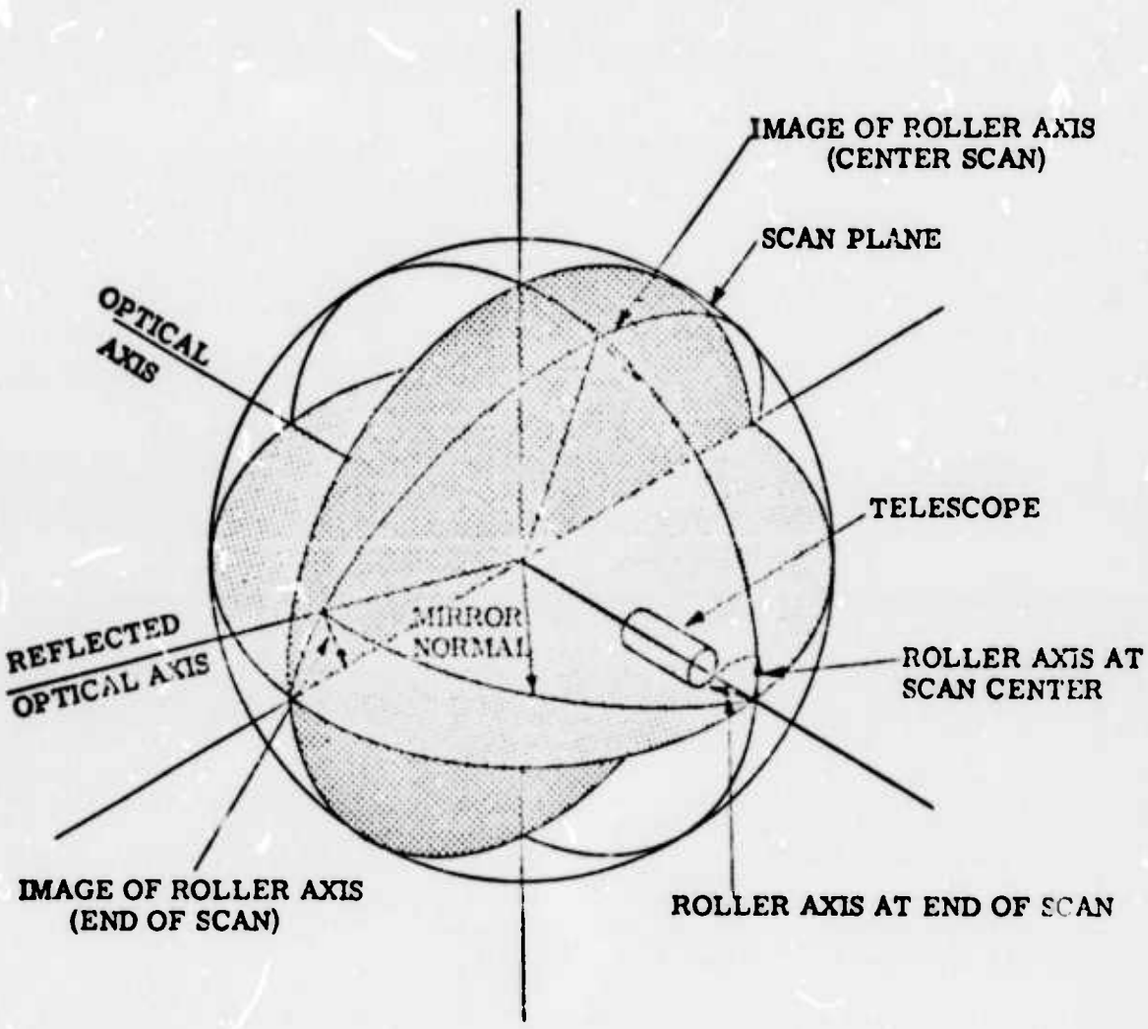

Figure 5. Plane-Scan Image Geometry on the Celestial Sphere

2.2.3 Comparision of Mirror Scan and Gimbal Scan

Figure 6a shows the geometrical relationship of the telescope and scanning mirror originally proposed to do the scanning.

Figure 6b shows the time-phased motions for three axes and Table I summarizes the comparisons between the two concepts for scanning.

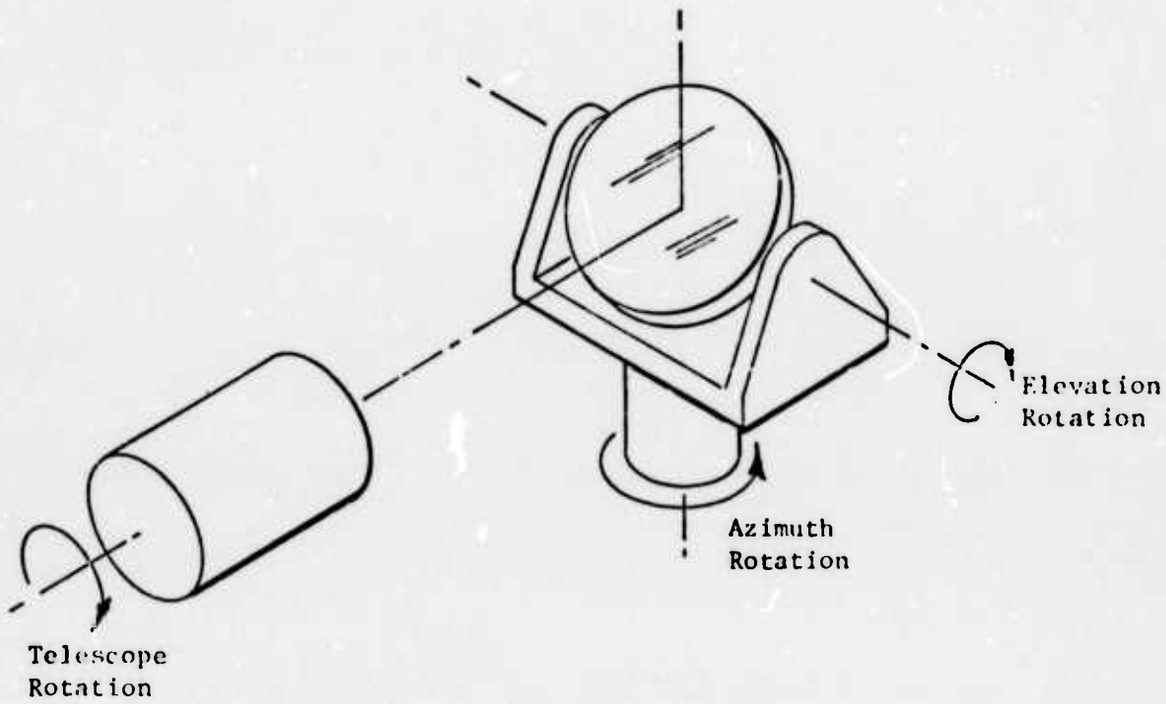

Figure 6a. Mirror Scan Geometry

Note elevation axis rotates with Azmuith angle.

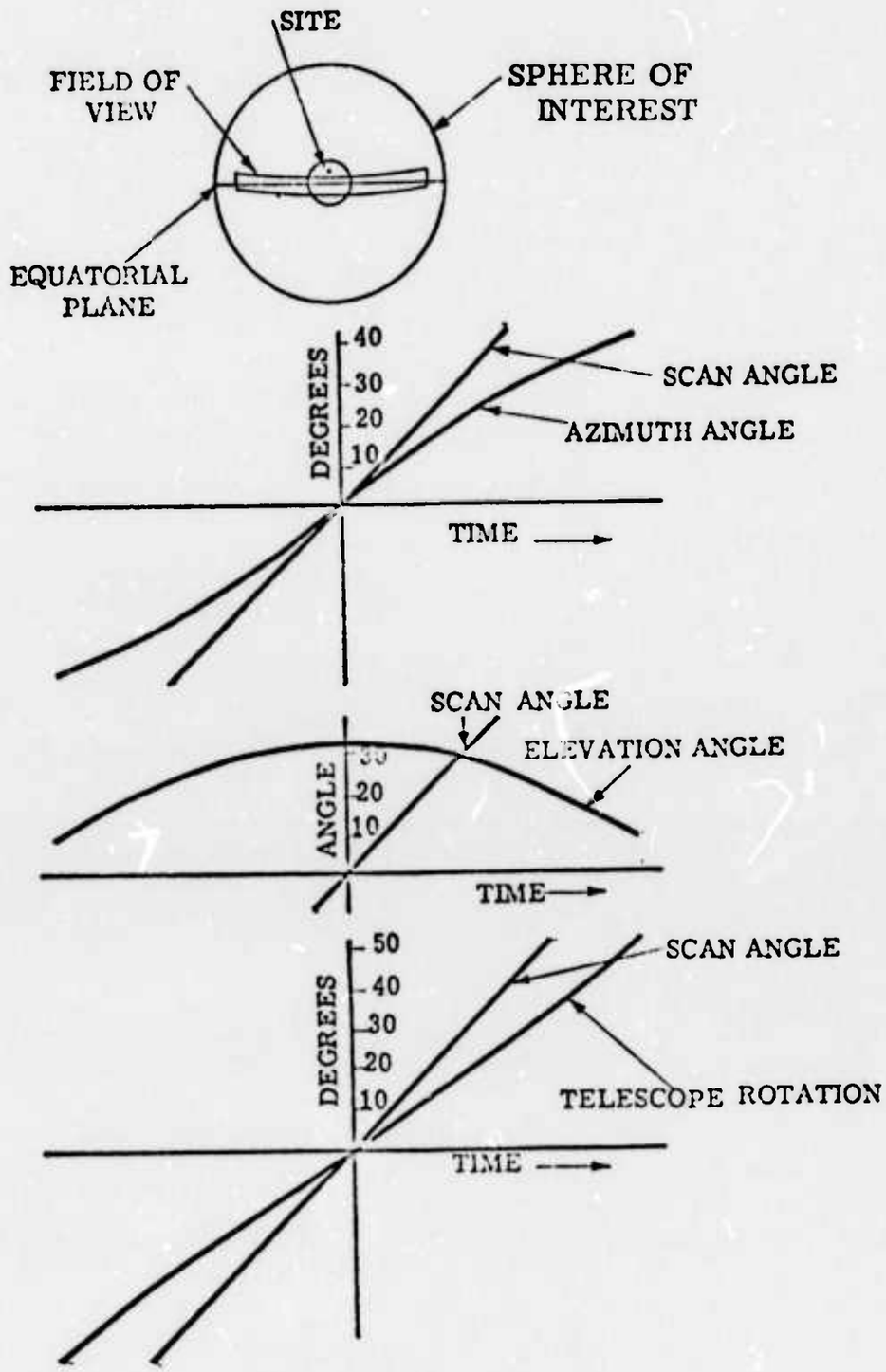

Figure 6b. Scan Motions for Mirror System at a Particular Site

TABLE 1. COMPARISON OF MIRROR SCAN AND GIMBAL SCAN

	Mirror Scan	Gimbal Scan
Residual Earth Rate Errors	None	None
Number of Servo-Coupled Variables	Velocity and Position Of: Azimuth Angle Elevation Angle Telescope Rotation Belt Displacement	Velocity and Position Of: Gimbal Angle Belt Displacement
Is Telescope Motion Required?	Yes (About Optical Axis Only)	Yes (About Gimbal (Scan) Axis Only)
Can all Target of Interest be Centered in FOV During Scan?	No	No
What Would be Required to do so?	Capability For Transverse Belt Motion And Wider Belt	
What is Required to Center Specific Viewing Angles in Field of View?	Different Azimuth/Elevation Rotation Program for a Different Great Circle Scan	Operated Second Gimbal Axis
Constant Velocity Scan	Yes	Yes
Constant Velocity Gimbal Motion	No	Yes
Effect of Significant Moments of Inertia	Detremental-Means Must Supply Significant Acceleration Torques to Achieve Scan	Helpful-Tends to Hold Scan Velocity Constant-Servo Need Only Cancel Disturbing Torques
Rapid Flyback Considerations	Significant Inertias Will Require High Driving Torques Four Variables Must Initialized Prior to Each Scan	Gimbal Inertia is Greater Requiring Still Greater Torque Only Two Variables Need to be Initialized

SECTION III

THREE-AXIS GIMBAL

3.1 BASIC GIMBAL REQUIREMENTS AND DESIGN APPROACHES

The overriding requirement of the gimbal was that it be capable of scanning great circle having a general east-west direction. This was further refined to:

a) Scanning ±75° scan the zenith along a great circle

b) Moving the scan pattern on the elevation axis (generally north-south) ±75° scan zenith

c) Supply sidereal compensation plus ±30° motion on this polar oriented axis.

with the hierarachy of mounting being mount to sideael to elevation to scan. There was one additional constraint at the beginning, that being the entire gimbal/telescope would have to fit within a 16-foot diameter astronomical observatory dome.

In the first investigation, the internal clearance within the dome and the openings available that would provide an unobstructed field of view for the telescope took precedence over the specified gimbal axis freedom. For this investigation, we used a standard closed-loop structure for the supporting yokes (see Figure 7). The rotational freedom of the individual gimbal axes were limited (see Table 2 for the system identified as Figure 7). The available freedom was severly limited to ±40 degrees in elevation and +60, -50 in scan. Since the deflection angles were severely limited by the dome size, the decision was reached to design the dome around the gimbal, which could achieve the desired angular coverage. The required size for the dome for this gimbal configuration appears to be 20 feet in diameter. The size and location of the doors are shown in Figure 8 with appropriate comments in Table 2.

There is another configuration that looks simpler and less gross dimensionally. It is shown in Figure 9. This design will provide almost

unlimited coverage of the heavens from horizon to horizon along with the capability of scanning east/west, north/south or any combination thereof. However, it also requires a 20-ft. dome. The two gimbal design concepts are discussed in the following section and the basic features are compared.

3.1.1 Gimbal Configuration Tradeoffs

The proposed configurations for the TEAL-AMBER I gimbal and telescope are shown in Figures 7, 8, and 9. There are two basic gimbal configurations, one utilizing an elevation yoke and scan ring assembly with the load centered between the supports, and the other having two of the three axes cantilevered off the support structure.

3.1.2 Loads, Stiffness and Coverage

The configuration shown in Figures 7 and 8 has the load centered between the bearings, thereby reducing the bearing load and bearing friction torque and increasing the overall stiffness of the mounting structure (see Table 3). The limitation to this design is the angular freedom or sky coverage available before the support structure infringes upon the telescope field of view (FOV).

The second basic configuration is shown in Figure 9. This design has two of the three axes cantilevered off the support structure and the third (scan) axis utilizing the double support arrangement. The allowable angular freedom (sky coverage) of this design is basically unlimited

By using the sidereal axis, one can orient the elevation axis at any angle relative to the horizon. For example, by positioning the elevation axis parallel with the horizon, an east/west scan can be generated, and the scan declination can be varied by the elevation axis. Actually, the poles for the grid pattern generated by the scan motion and elevation motion are at the horizon, or the equator goes through the zenith. The other extreme position would be to rotate the elevation axis (via the sidereal axis) to be perpendicular to the horizon (vertical), then by rotating the scan axis support yoke (or elevation axis), any great circle from east/west to north/south can be scanned. The pole of the grid pattern is effectively at zenith. However, this concept suffers from lower structural stiffness, lower natural resonance frequency, and higher bearing loads when compared

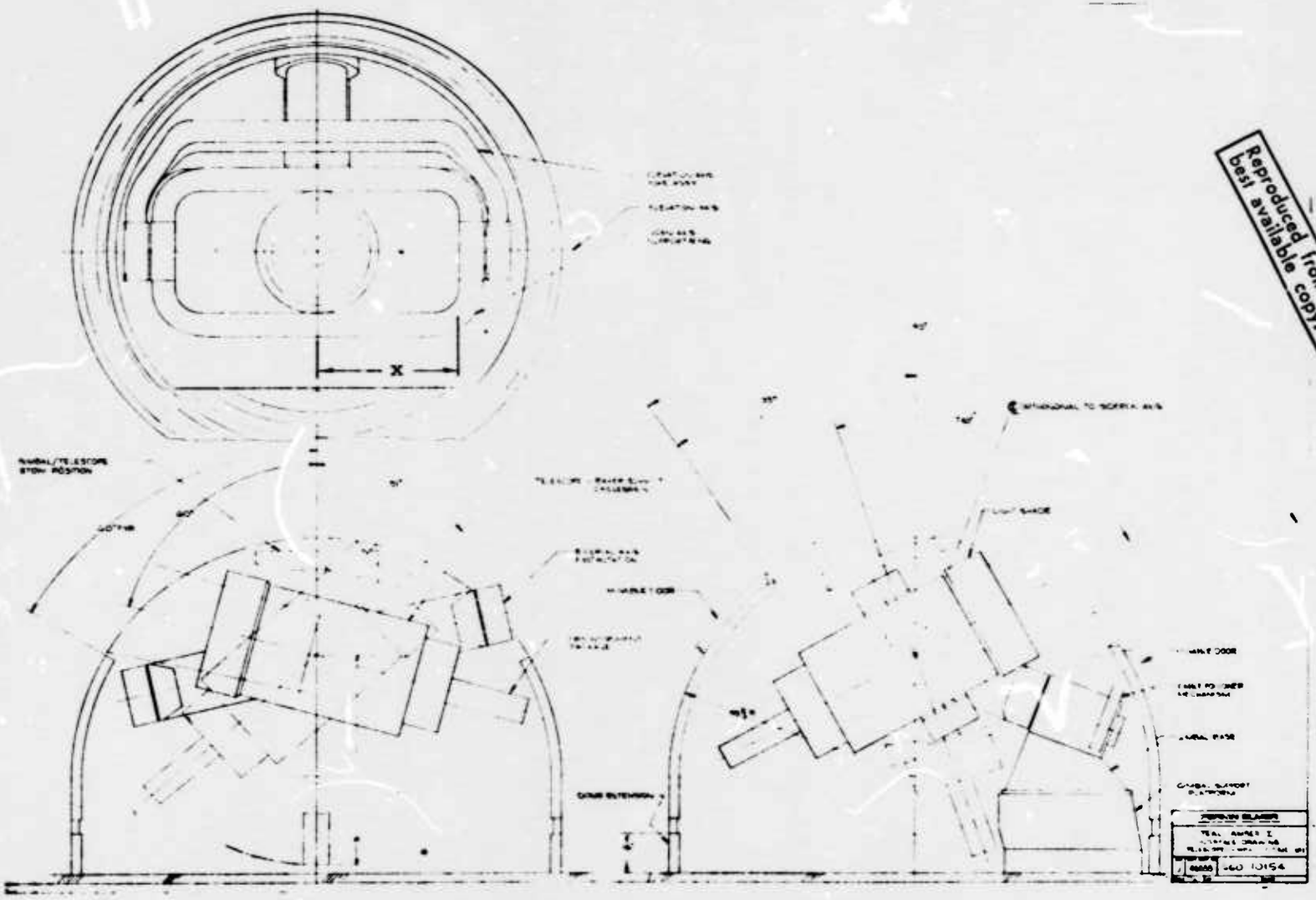

Figure 7. TEAL-AMBER I Telescope Gimbal Configuration, Load Centered Between Bearings, 16-Foot Dome

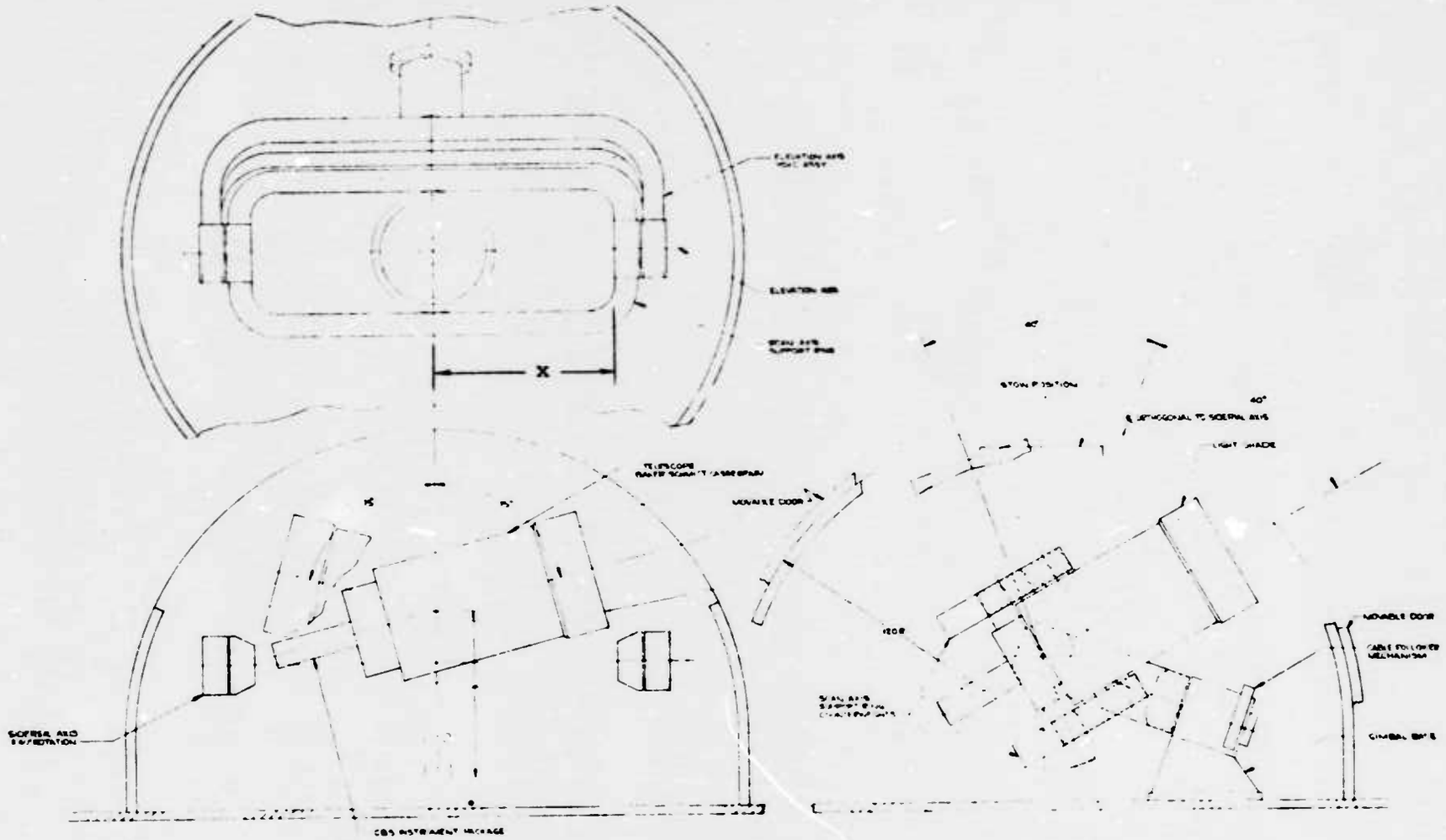

Figure 8. TEAL-AMBER I Telescope Gimbal Configuration, Load Centered Between Bearings, 20-Foot Dome

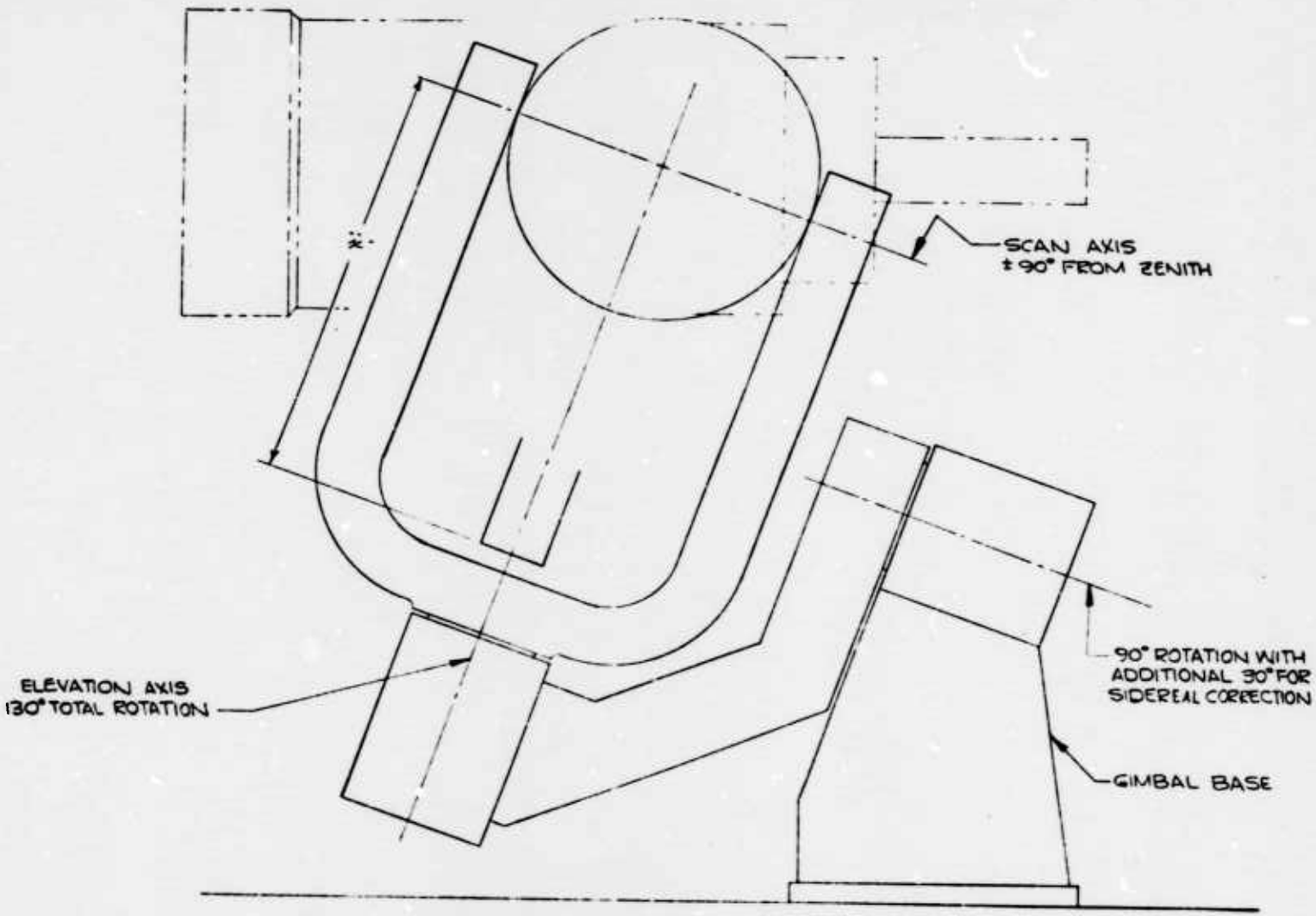

Figure 9. TEAL-AMBER I Telescope Gimbal Configuration, Cantilevered Axes, Unlimited Freedom

TABLE 2. GIMBAL ANGULAR COVERAGE

Gimbal Configuration	Dome Size	Specified Min. Angular Coverage	Available Angular Coverage	Comments
Per Figure 7	16 Feet	Scan ± 75° Elevation ± 75° Sidereal ±100°	+60 -50 (from zenith) ±40 (orthogonal to sidereal axis) ±30 (greater if req'd up to ±100)	Limited by dome openings and allowable size of gimbal that fits within the dome
Per Figure 8	20 Feet	Scan ± 75 Elevation ± 75 Sidereal ±100	±75 (from zenith) +40 -75 (orthogonal to sidereal axis) ±30* (greater if req'd up to ±100)	*Limited by height from pad to support structure - can be increased by the addition of a raised support
Per Figure 9	20 Feet	Scan ± 75 Elevation ± 75 Sidereal ±100	±90* (from zenith) ±75* ±30 (greater up to ±100 if req'd)	*Greater if required and dome openings are available

to the configuration shown in Figures 7 and/or 8 (see Table 3).

3.1.3 Size

The physical size of the gimbal was predicated by three basic parameters -- the outside diameter of the telescope tube, the overall length of the telescope and instrument package, and the angular freedom that is required to subtend the desired coverage of the sky. This is true for all configurations. However, the configuration in Figure 9 allows for a greater angular freedom since the telescope FOV is not limited by the portion of the support ring eliminated by this design for similar gimbal sizes, but coverage cannot be traded for gimbal size since size is also a structural consideration.

In both cases, the length of the elevation axis support arms (the large size item) is dependent upon the distance from the center of gravity of the telescope and instrument packages to the extreme end of the instrument (distance x, see Figures 7, 8, and 9). This distance can be changed by the addition of counterweights as desired, but the rewards are not too fruitful.

By reducing x, the length of the support structure is reduced a like amount; however, as counterweights are added to the telescope, the strength of the support structure must be increased, and the drive system is impacted by a larger mass moment of inertia. For example, to shift the center of gravity of the telescope and instrument package a distance of ten inches would require approximately 800 pounds of counterweight located at the extreme end of the instrument. This increases the mass moment of inertia by approximately fifty percent and will require a stiffer support structure.

This indicates that although it is possible to shift the center of gravity of the telescope and instrument package by adding counterweights, it is not practical in the overall sense.

There are other alternate methods to reduce the size of the x dimension. Another conventional method at counteracting the unbalance, as a result of not rotating about the center of gravity, is to use torsion bars. However, they are not adaptable to gimbals of these configurations. This results from the gravity vector being a variable dependent on the orientation of the sidereal and/or elevation axes.

TABLE 3. GIMBAL CONFIGURATIONS

Characteristic Feature	Double Support (Figure 8)	Cantilever (Figure 9)
Structural Consideration	>10X Stiffer For Given Cross Section	Larger Cross Section Required To Produce Equal Stiffness
Bearing Capacity and Friction Torque	Load = w/2 Torque ≈ 30 ft#	Load ≈ 3W Torque > 200 ft#
Telescope Scan Coverage	Limited in N/South Direction	Basically Unlimited
Mount Resonant Frequency	>5Hz	>1Hz
Dome Dimensions	20'	20' Dome + 3' Cylindrical Extension

Another alternative to achieve shorter support arms is to fold the instrument package so that its length lies parallel with the back surface of the primary mirror. This will foreshorten the overall length of the telescope and instrument package; however, the outside dimensions of the telescope tube will increase, and certain problem areas within the instrument package preclude this approach.

The last alternate considered is unique to the three-axis system. This approach uses the sidereal and/or elevation axes to extend the angular coverage of the scan axis under certain conditions. This would be done by constantly moving the yoke out of the way of the scanning telescope during scan. This requires monitoring all the axes and a nonlinear scan motion coupled with angular velocities on the sidereal and/or elevation axes in the vicinity of the scan velocities. This approach adds a degree of control complexities that is not considered prudent for the TEAL-AMBER system.

3.1.4 Gimbal Selection

The recommended choice for a gimbal configuration that will best fulfill all the system requirements without the possibility of serious degradation to the performance is that shown in Figure 8.

This is due primarily to the elimination of the cantilevered construction of the elevation axis associated with the design shown in Figure 9. The double support of Figure 8 reduces the bearing loads and drive torque on the elevation axis and primarily increases the structural rigidity and natural frequency of the gimbal assembly.

The reduction in bearing loads will reduce the torque requirements for the elevation motor and, subsequently, the motor size and weight. A larger motor would imply a system with a lower natural frequency for the same stiffness. The system that is stiffer and has a high natural frequency should have smaller amplitude variations of motions induced by seismic causes or telescope turnaround transients. Thus, the system shown in Figure 8 will have less unwanted image motion due to mechanical disturbances than that in Figure 9. However, if scan versatility is the major consideration, the configuration of Figure 9 is best suited, but the primary TEAL-AMBER I scan pattern is met by the configuration of Figure 8. Figure 7 has been eliminated because of limited field coverage.

3.1.5 Special Design Considerations

The areas of the three-axis gimbal mounts that will require special attention during the design phase are as follows.

3.1.5.1 Servo System and Resonant Frequencies

The servo drive system, including loop bandwidth, gimbal accelerations, and settling times, along with the resonant frequency of the gimbal structure and seismic mount, will all affect pointing accuracy. Since each of these is inter-dependent upon the other, their fundamental characteristics should be established prior to the design phase so that during the gimbal design, any natural frequency associated with the seismic mount can be avoided insofar as the gimbal structure is concerned.

3.1.5.2 "g" Loading on Components During Turnaround

The ends of travel on all three gimbal axes will require shock absorbers to absorb the inertia of the gimbal plus the propelling force (drive motor) in the event a limit switch fails. The initial design swing radii for the instrument package and telescope correctors indicate that a limit acceleration not exceeding $250°/sec^2$ will produce "g" loading on the components less than 1.0g. This holds for components located at the farthest point from the axis of rotation; for those components located at a lesser radius, the "g" loading will be less by the ratio of the extreme radii to that of the specific component.

3.1.5.3 Control of Cables

Cable wrap mechanisms should be provided on all three gimbal axes. This is especially important on the sidereal and scan axes to provide adequate cable length without adding torque fluctuations to the drive train.

To effectively eliminate the drive torque fluctuations, each of the cable wrap mechanisms should have a separate closed-loop servo drive to supply the quantity of cable necessary to rotate through the required look angle. This is required because, as the cable is wrapped tighter, the frictional force between cable and cable drum increases, thereby changing the required torque as a function of look angles and direction of rotation (wind vs unwind).

3.1.5.4 Drive Train

The severe acceleration requirements for a gimbal of this size coupled with the necessary pointing accuracy will necessitate special drive train techniques. Since each axis is bidirectional, the first impulse is to employ a direct drive motor to the gimbal axis. With the motor directly coupled to the gimbal axis, all backlash that is a major drawback with any single-drive motor gear train is eliminated. The disadvantage of the direct coupled motor is the ripple torque inherent in its design. The ripple can occur up to 150 times per second for motors comparable in size to the TEAL-AMBER requirements. The magnitude of ripple torque (average to peak) is approximately four percent. This is not compatible with the servo requirements as far as linearity and jitter are concerned.

The standard gear train without preloaded gears presents a problem in that the backlash inherent in the design creates a deadband in any bidirectional system. To eliminate this, the proposed design will use two drive motors and two pinions. During periods of peak acceleration where the gear tooth and motor loads are at a maximum, both motors will drive in the same direction and share the load. Once the gimbal has achieved the required velocity, one motor will be driven in the opposite direction at some predetermined torque level to remove all the backlash from the gear train. This will accomplish two things -- it will provide higher acceleration rates with minimum gear loading and will eliminate the deadband associated with gear backlash.

3.1.5.5 Telescope Mounting

The gimbal scan axis will have structural integrity independent of the telescope structure. This will reduce the loading on the telescope housing since it will not be subjected to bearing eccentricity, thermal loading, or buffer stop engagement.

By providing a separate telescope mount on the gimbal, the size, weight, and inertia of the telescope can be duplicated with a mass model. This will accelerate both delivery dates since neither is dependent on the other during their fabrication and test phases.

3.2 GIMBAL SPECIFICATIONS

3.2.1 Item Definition

The gimbal subsystem will support, align, point, and scan the telescope (defined in Paragraph 2.2). There will be two scanning modes -- constant velocity and discrete steps. There will be three gimbal axes in the order of sidereal, elevation, and scan (see Figure 1). The gimbal subsystem consists of two major subassemblies -- the gimbal subassembly and the servo electronics package. The gimbal subassembly consists of the base including the sidereal axis, the elevation yoke assembly, the scan axis supporting-ring assembly, and the telescope/gimbal interface structure. The servo electronics package consists of the electronics required to operate the gimbal subsystem in any mode specified herein including all controls, cabling, and displays. The controls and displays shall be mounted within a console to provide for remote operation of the gimbal subsystem. The gimbal subsystem will be designed for instaliation at the Haleakala Observatory in Maui, Hawaii.

3.2.2 Interface Characteristics

3.2.2.1 Mounting

The gimbal subassembly shall be hard mounted to a seismic isolation pad (GFE) through a kinematic design, i.e., the design will be such that motion caused by expansion will produce negligible stresses in the gimbal subassembly.

3.2.2.2 Telescope Characteristics

Weight:	2300 lbs.
Inertias:	X = 120 lb-ft-sec^2
	Y = 300 lb-ft-sec^2
	Z = 300 lb-ft-sec^2

3.2.2.3 Telescope Mounting Surface

A surface will be provided on the scan gimbal for mating with the telescope. The reference surface will be parallel to the scan axis with a maximum error of one arc-minute.

3.2.2.4 Gimbal Weight

< 20,000 lbs

3.2.2.5 Gimbal Power Consumption

< 4.5 kw average

< 7.5 kw peak

3.2.2.6 Generated EMI (Mil Spec TBD)

3.2.2.7 Overall Dimensions

The gimbal with the telescope mounted shall be stowed in a 20-foot diameter, hemispherical astronomical observatory dome.

3.2.3 Gimbal Specifications

3.2.3.1 Angular Excursions

	Configuration* (1 & 2)	Configuration* (3)
Sidereal Axis	±40° from nominal**	150*
Elevation Axis	±40° from nominal	135
Scan Axis	±75° from nominal	± 90 (Constant velocity on five discrete steps of 5°)

The nominal position is when the telescope's optical axis is parallel to the local vertical and perpendicular to the elevation axis.

---

* Configurations 1, 2 & 3 are those shown in Figure 7, 8, & 9 respectively.

** Greater if desired.

3.2.3.2 Axis Alignment

a. Sidereal Axis Alignment - Alignment of the sidereal axis with respect to the earth's axis of rotation will not deviate more than 15 arc-seconds.

b. Elevation Axis Alignment - The elevation axis will be perpendicular to the sidereal axis with a maximum error of 2 arc-minutes for the total excursions along the sidereal axis.

c. Scan Axis Alignment - The scan axis will be perpendicular to the elevation axis for the total excursions along the elevation axis to a maximum error of 2 arc-minutes. The scan axis will be parallel with the sidereal axis to a maximum error of 2 arc-minutes for 0° elevation angle.

3.2.3.3 Scan Axis

a. Constant Velocity Scan - Scan rates shall be variable from 0.25 to 5.0 degrees per second. The gimbal response time to these scan rate inputs will be defined as the time between the instant when constant velocity is commanded to the instant when the gimbal settles to a rate that maintains the rate sensor at the commanded velocity with the maximum error not to exceed 1 arc-second per second.

b. Slew Rate - The scan axis slew rate input shall be variable from 0.5 to 20 degrees per second.

c. Retrace Period - The scan axis drive system will be capable of reversing the direction of rotation of the telescope from a velocity of 5 degrees/second, then rotating the telescope through an angle up to 150 degrees with velocities up to 20 degrees/second, again reversing the direction of the telescope and accelerating to a velocity not to exceed 5 degrees per second and settling to the specified rate and tolerance all within ten seconds.

d. Step Scan - The scan axis system will be capable of stepping the telescope through discrete angles of 5° ± 0.05°. The time to move from one position to the next and damp out to less than 5 arc-seconds will be less than 1 second.

3.2.3.4 Elevation Axis

a. Scan Rate - Not required.

b. Slew Rate - The elevation axis slew rate input will be variable from 0.25 to 2.0 degrees per second.

3.2.3.5 Sidereal Axis

a. Track Rate - The track rate input to the sidereal axis will be 15 arc-seconds per second. The axis will settle to a rate of 15 arc-seconds/second plus or minus one percent.

b. Slew Rate - The slew rate input to the sidereal axis will be variable from 0.5 to 3.0 degrees per second.

3.2.4 Servo Performance Requirements

3.2.4.1 Rate Linearity

The angular rate on each axis will be a linear function of command voltage. The maximum rms deviation from linearity will be:

Scan Axis Linearity	≤ 1.0 arc-sec/sec (scan mode only)
Sidereal Axis Linearity	≤ 0.15 arc-sec/sec (track mode only)
Elevation Axis Linearity	Not applicable

3.2.4.2 Jitter

Jitter is the instantaneous difference between the rate corresponding to the input command and the actual rate of the gimbal axis.

a. Scan Axis - The amplitude of the one sigma instantaneous rate jitter will be equal to or less than one arc-second.

b. Sidereal Axis - The amplitude of the one sigma instantaneous rate jitter will be equal to or less than 0.15 arc-second.

c. Elevation Axis - Not applicable.

3.2.5 Gimbal Axis Encoders

Each axis will be provided with a natural binary encoder, and the data output will be in serial format. The encoder resolution will be:

Scan Axis	21 bit or $\pm$0.62 sec
Sidereal Axis	21 bit or $\pm$0.62 sec
Elevation Axis	18 bit or +5.0 sec

3.2.6 Caging

The servo electronics control panel will have provisions for remote caging and uncaging the gimbal axes. The cage positions will be as follows.

3.2.6.1 Scan Axis

The scan axis will have two cage positions -- one at 0° and the other at 60° relative to a line through the center of rotation of the elevation axis.

3.2.6.2 Sidereal Axis

The sidereal axis will have two cage positions -- one at 0° and the other at -30° (zero corresponds to the central position where the elevation yoke is horizontal).

3.2.6.3 Elevation Axis

The elevation axis will be capable of being stowed at any position throughout its travel.

3.2.7 Mechanical Stops

Soft mechanical stops and means for limiting angular velocity, if required, will be provided such that peak acceleration (negative) is limited to 250°/sec^2 under any operating condition or in the event of failure to the control system (to limit "g" load to < 1.5g).

3.2.8 Limit Switch

Six electrical limit switches will be provided at ±40° (sidereal axis), ±40° (elevation), and ±75° in scan. Actuation of the limit switches will remove power to the drive motors and will provide console indicators to alert the operator. Provisions will be made for external reset.

3.2.9 Electrical Cable Feedthrough

In addition to the cabling required for the gimbal, the system will provide three 24-pin cables for instrumentation on the telescope. The method of providing adequate length commensurate with gimbal axis freedom will be through a cable wrap mechanism. The wrap mechanism, if required, will have an independent drive system consisting of motor, synchro, and closed-loop servo control to eliminate torque variations that could affect gimbal axis performance.

SECTION IV

TELESCOPE

4.1 RECOMMENDED SYSTEM SUMMARY

Table 4 shows the desired range of telescope specifications and the set of parameters established by CBS for their preferred design. These values were used to excerise the various design options for the telescope. The conclusions reached were that : (1) a form of the Baker-Schmidt Cassegrain would be the optiminum form for the telescope, and (2) the Baker-Nunn Camera is not appropriate for the application. The form of Cassegrain recommended for the TEAL-AMBER system is an all-spherical system using one type of glass throughout. The design is similar to the one used in the TRIM lens system manufactured by Perkin-Elmer for many years. A layout of the system is shown in Figure 10.

4.2 APPLICABILITY OF THE BAKER-NUNN TELESCOPE FOR THE TEAL-AMBER I TELESCOPE

As part of the TEAL-AMBER I Telescope Study contract, Perkin-Elmer was required to analyze and evaluate the existing Baker-Nunn telescope for possible use in the program. The conclusions reached were negative. The Baker-Nunn telescope as it exists today would not satisfy the TEAL-AMBER I requirements. In fact, it is questionable, even with extensive rework and modifications, that it could be used and was, therefore, found inappropriate for this application. This section outlines the reasoning used to reach this conclusion.

4.2.1 Desired Telescope Specifications

Table 4 shows the desired range of telescope specifications. These values are compatible with the moving tape concept, the present system sensitivity requirements, and the present CBS camera configuration. The desired aperture will be closer to 36", and the image format requirement in the 2.6" to 5.2" range will result in an impossible optical design, therefore

TABLE 4. DESIRED TELESCOPE SPECIFICATIONS

	Possible Range of Values	CBS Preferred System
Aperture	20 to 36 inches	30 inches
Focal Length	30 to 45 inches	45 inches
f/No.	Faster than f/1.5	f/1.5
Focal Surface		
- Contour	Flat	Flat
- Position	Accessible in one hemisphere	6 inches behind last optical element
Spectral Region	4000Å to 6500Å	S-20 photo-cathode
FOV	5° x 10° max.	1 x 5°
Image Format	(2.6 x 5.2 in.) - (3.9 x 7.8 in.)	0.78 x 3.9 inches
Diameter for 80% of Energy	Between 4 arc-sec and 8 arc-sec	4 to 8 arc-sec
Distoriton	Selectable to minimize star motion	Minimize star motion
Optical Efficiency	>55%	>55%

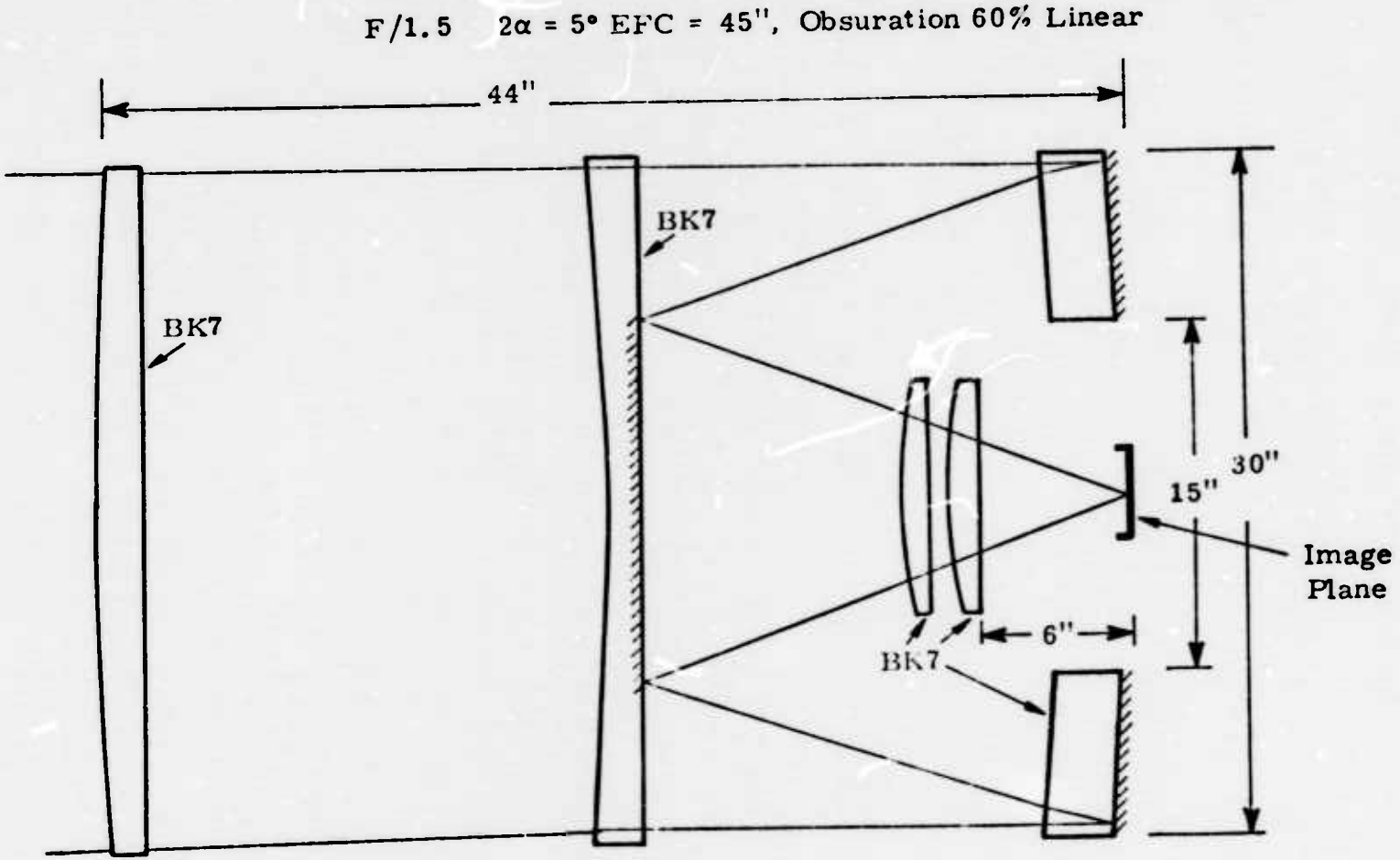

Figure 10. System D (Recommended System)
All-Spherical System

requiring eventual system tradeoffs. However, the above values will be used to evaluate the B/N telescope since cost is also a major consideration.

4.2.2 Baker-Nunn Telescope in Present Configuration

Table 5 shows the existing B/N optical characteristics. The major shortcomings are mainly in the position and contour of the focal surface. We may consider effectively replacing the film strip with the CBS camera, thus not requiring hemispherical accessibility at the focal plane. However, the camera uses an electron imaging section, which requires a uniform magnetic field. Under these conditions, the photocathode area (active image format) is small relative to the envelope size of the image section (in the 1:5 to 1:10 linear ratio region), and there is considerable length to the camera, thus increasing the central obscuration to unacceptable levels. Also, the electron optics require a flat photocathode or optical image surface to transfer the photoelectron image onto the flat tape with high resolution. Therefore, the present design is not appropriate and would have to be modified to bring the image surface out of the incoming energy and to make the optical focal surface flat.

4.2.3 Methods to Make the Focal Surface Accessible

Several modifications to the B/N have been suggested to make the focal surface accessible. They are: (1) to use relay optics, (2) to use a folding flat (two configurations), and (3) to convert the telescope into a Cassegrain.

4.2.3.1 Relay Optic

It is conceivable to transfer the image outside the telescope by using a relay lens system. However, the system would have to work over a large format at f/1 in order to transfer the large field angles. This requirement is created by the fact that the first optical element along the fold mirror must be close to the focal plane or the obscuration would increase to an intolerable condition (see Figure 11). Under these circumstances of high optical power and large image format, high resolution is doubtful if not impractical. In addition, the system would still require field flattening; therefore, this concept is considered impractical.

TABLE 5. BAKER-NUNN OPTICAL SYSTEM CHARACTERISTICS

Aperture	Limited at correctors to 20 inches
Focal Length	20 inches
f/No.	1
Focal Surface	
- Contour	Spherical
- Position	Incoming energy
Spectral Region	4000Å to 6500Å
FOV	5 ° x 30°
Image Format	~1.75" x 10.5"
Diameter for 80% of Energy	8 to 10 arc-seconds previous 6 arc-seconds modified (P-E)*
Distortion	= stop at correctors
Optical Efficiency	0.55 to 0.68

(Original) (Updated)*

*Based on study made in 1969 to upgrade the B/N

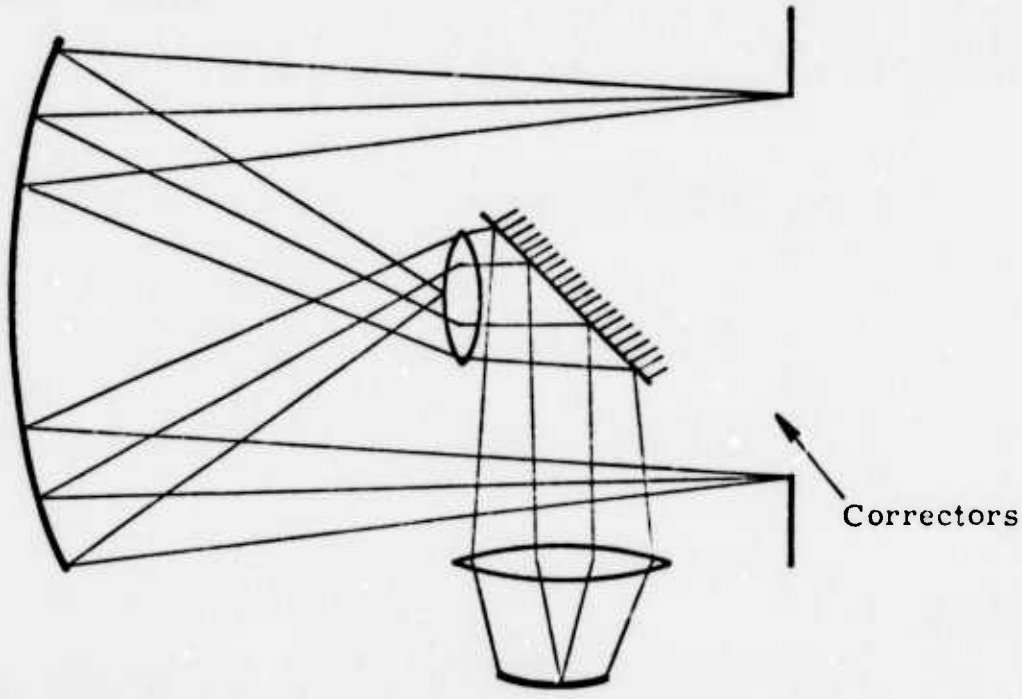

Figure 11. Relay Optics Concept

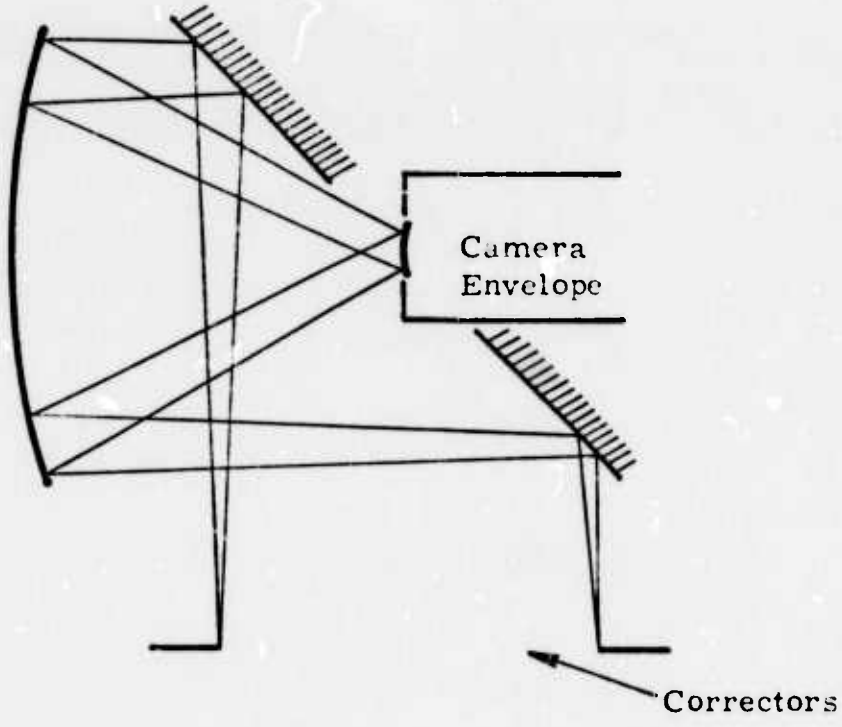

Figure 12. Folding Flat Between Correctors and Primary

4.2.3.2 Folding Flats

a. Folding Flat Between Correctors and Primary - In this configuration, the focal surface is somewhat accessible (see Figure 12). However, there exist the following problems: (1) The amount of obscuration is dependent on the actual camera size and positions of the folding mirror, probably on the order of 30% area obscuration (2) The field is still convex and additional optical elements will be required to flatten the field. In order to achieve the flattening and still maintain high resolution, all the basic curvatures will most likely require reoptimization, thus, implying considerable optical rework. (3) The stop for the system is at the corrector plates and cannot be varied for distortion correction without losing aperture diameter. (4) Finally there is a major modification of the housing and mechanical parts.

Based on the above arguments, this configuration has a low probability of satisfying all the requirements for the TEAL-AMBER I telescope even after considerable rework and design effort.

b. Folding Flat Between Image Surface and Primary Mirror (see Figure 13) - In order to make the focal surface accessible, the mirror must be moved rather close to the primary. This has two effects that can be traded against each other -- central obscuration and vignetting at large field angles, depending on the size of the fold mirror. This is shown by the two mirror sizes in Figure 13. In either case, the useful aperture area will be small. In addition, the system still suffers from the same problems of field curvature and stop position discussed in the previous section. Thus, this configuration is also not a favorable solution to the problem.

4.2.3.3 Cassegrain (see Figure 14)

The Cassegrain arrangement does make the focal surface accessible; the secondary curvature, coupled with changing the other basic curvatures, could most likely be used to eliminate the requirement for field flattening refractors. However, the system f/no. will be on the order of f/1.7 to f/2 since the primary is not fast enough to accomplish both image surface

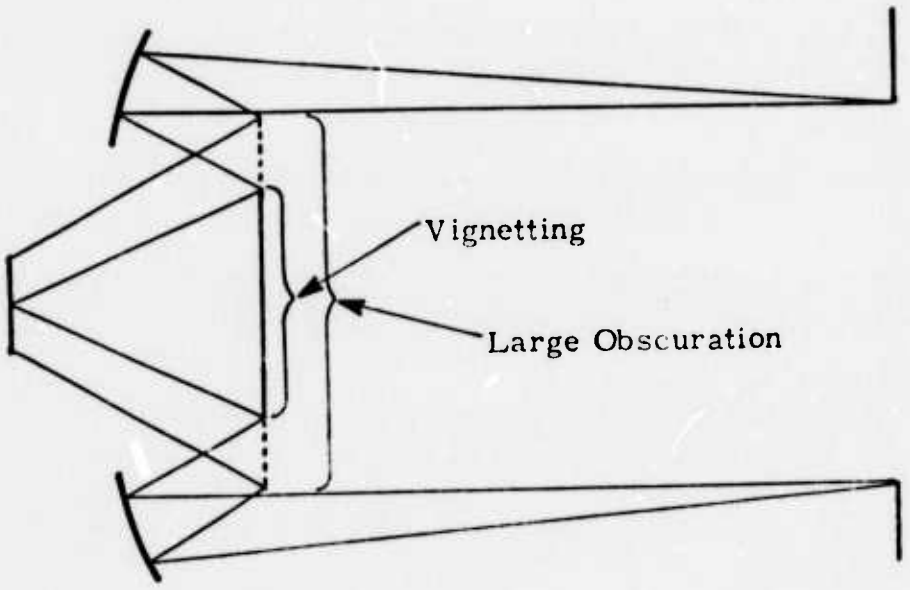

Figure 13. Folding Flat Between Image Surface and Primary Mirror

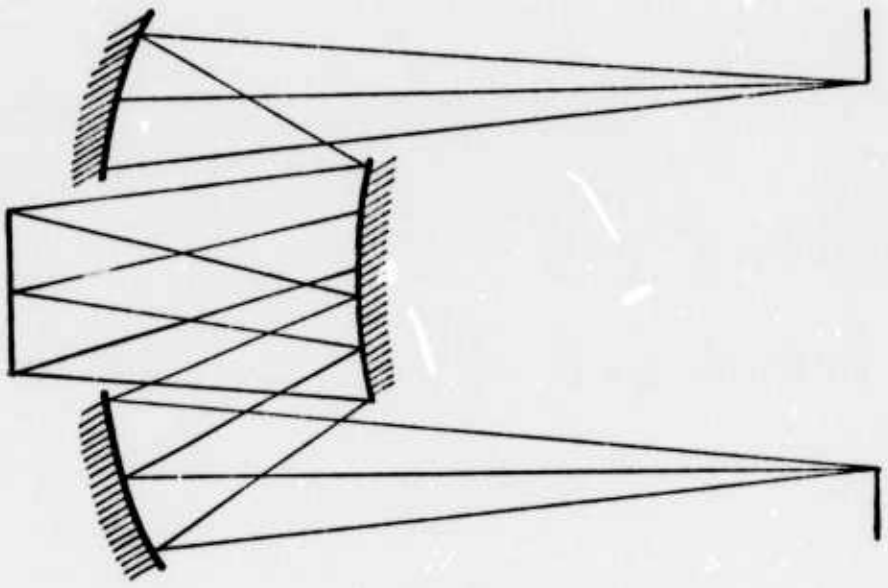

Figure 14. Cassegrain

accessibility and moderate obscuration (36% area obscuration). This implies a large focal surface format than a 20" f/1.5 system.

This system cannot be tuned for a specific distortion requirement without losing aperture since the stops are again at the correctors. Of all the forms of the B/N modifications, this is the best candiate. However, the maximum aperture that can be obtained is a 20" diameter, and the end design will probably be something less when the distortion requirements are defined. Of course, the central obscuration will increase in percentage as the aperture diameter is reduced.

4.2.4 Basic Shortcomings of Using and Existing B/N Telescope

The major shortcomings of all the B/N concepts are summarized below:

a. It requires additional elements to flatten the field and move it out of the incoming energy.

b. The aperture is limited at the correctors to a maximum of 20" diameter.

c. The stop for the system is at the correctors, and distortion control will probably reduce the aperture.

d. Basic curvatures of the optical elements will most likely have to be reoptimized for the new set of conditions.

e. Mechanical modifications will have to be made to the housing.

4.3 CASSEGRAIN SYSTEMS

As implied in the Baker-Nunn telescope tradeoff, the most promising optical form was the Cassegrain. This concept was further explored without the physical constraints of the actual B/N (like optic size, radii, obscuration). Two forms of the Cassegrain were examined, and the results are presented in the following paragraphs.

4.3.1 Baker-Schmidt Cassegrain (see Figure 15)

The first optical system explored was one made of flat-field anastigmats as described by J.G. Baker.* In this system, a concave mirror

* J.G. Baker, J. Amer. Phil. Soc., 82,339 (1940)

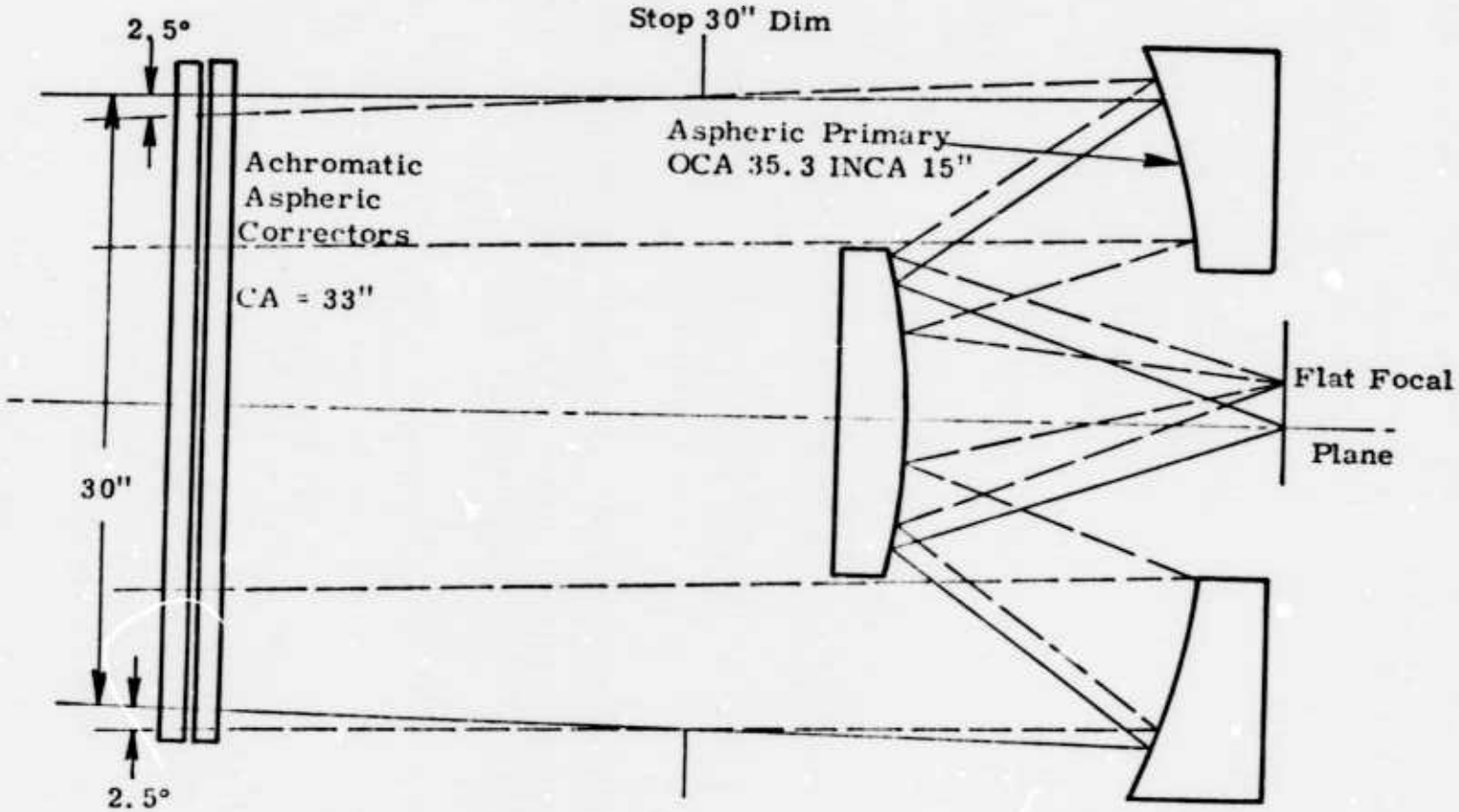

Figure 15. Baker Schmidt Cassegrain, EFL 45" F/1.5, 5° x 1° (5.1° Diag.) System A

and a convex mirror of substantially the same curvature are used. A refractor correcting plate is located between the centers of curvature of the two mirrors. With this arrangement, Baker obtained the wide field coverage of a Schmidt on a flat focal surface. The spectral range of this optical system is extended by making the refracting corrector plates achromatic In the version explored for the TEAL-AMBER I application, both mirrors are made aspheric. This is necessary if the system is to have a prescribed distortion.

A monochromatic study was made for two systems having different back focal lengths. System A had the focal surface 3.5" from the vertex of the primary mirror (see Figure 15). System B had the focal surface 6" from the primary vertex. The modulation transfer functions of both system are shown in the following figures and tables. These are monochromatic and show the effects in two directions, radial and tangential, with respect to the optical axis or center of the FOV. One should note that in the computer printout table for system A, the spatial frequency must be reduced by 2/3 because the run was for a 20" aperture and we are considering 30" apertures. Also shown as THEOR is the limiting MTF due to the diffraction effects of the highly obscured aperture and two reference MTFs for point spread functions, which have a Gaussion shape and 80% of the energy within a diameter of 4 arc-sec and 8 arc-sec. It should be noted that the accessibility of the focal plane requirement does not permit the system to work at its optimum. These systems like the focus very close to the vertex of the primary mirror.

While the monochromatic MTF's look acceptable, the wide spectral response causes the image to degrade. This degradation takes the form of chromatic variation of the spherical aberration. In system with the stop situated between plate and primary mirror, color coma and color astigmatism are also found. In order to correct these aberrations, it is necessary to use a three-element corrector, the two outside surfaces of which are spherical while the four inner surfaces are aspherical. However, the first and fourth are alike, as well as the second and third.

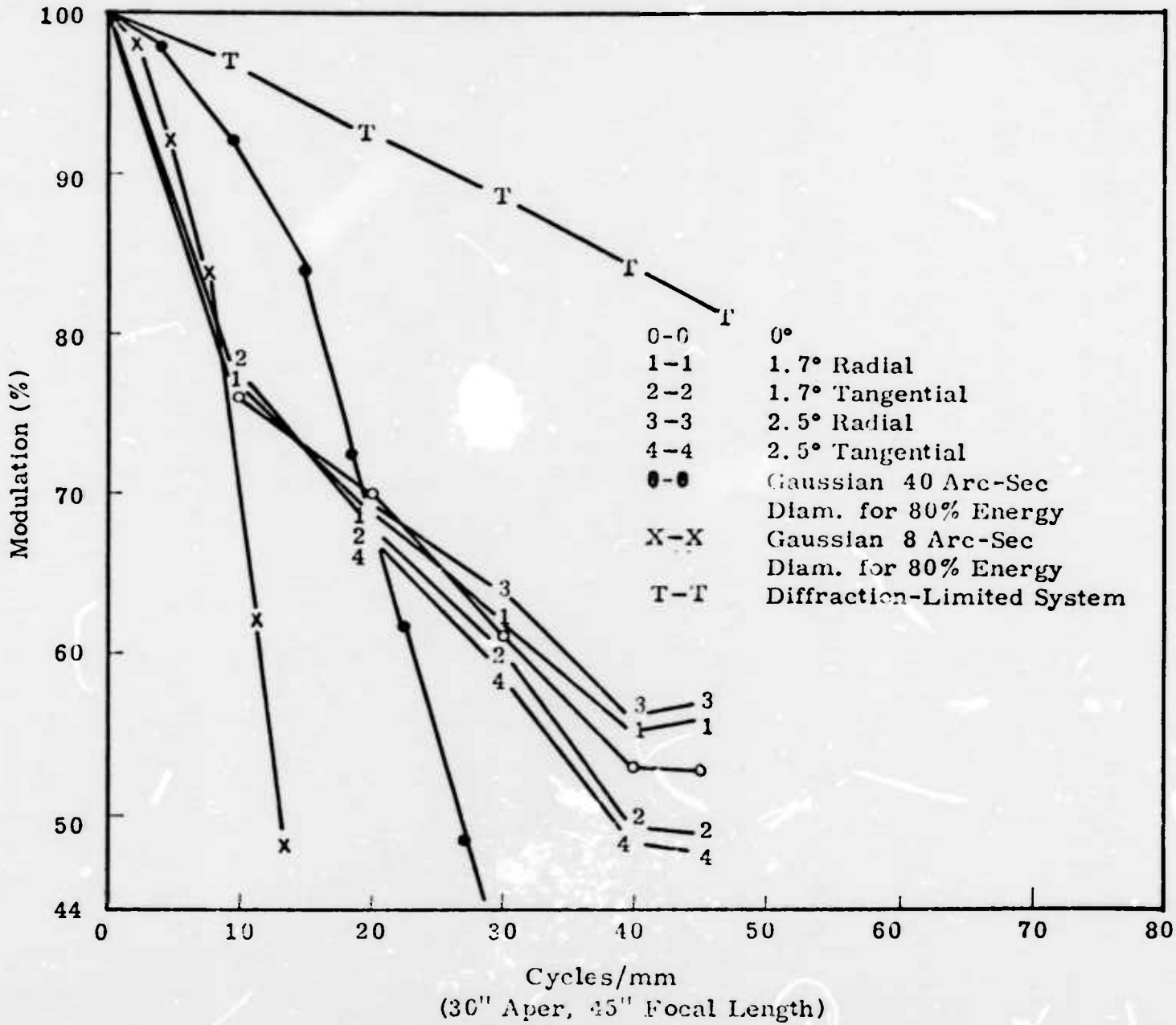

Fig e 16. Modulation Transfer Function, System A

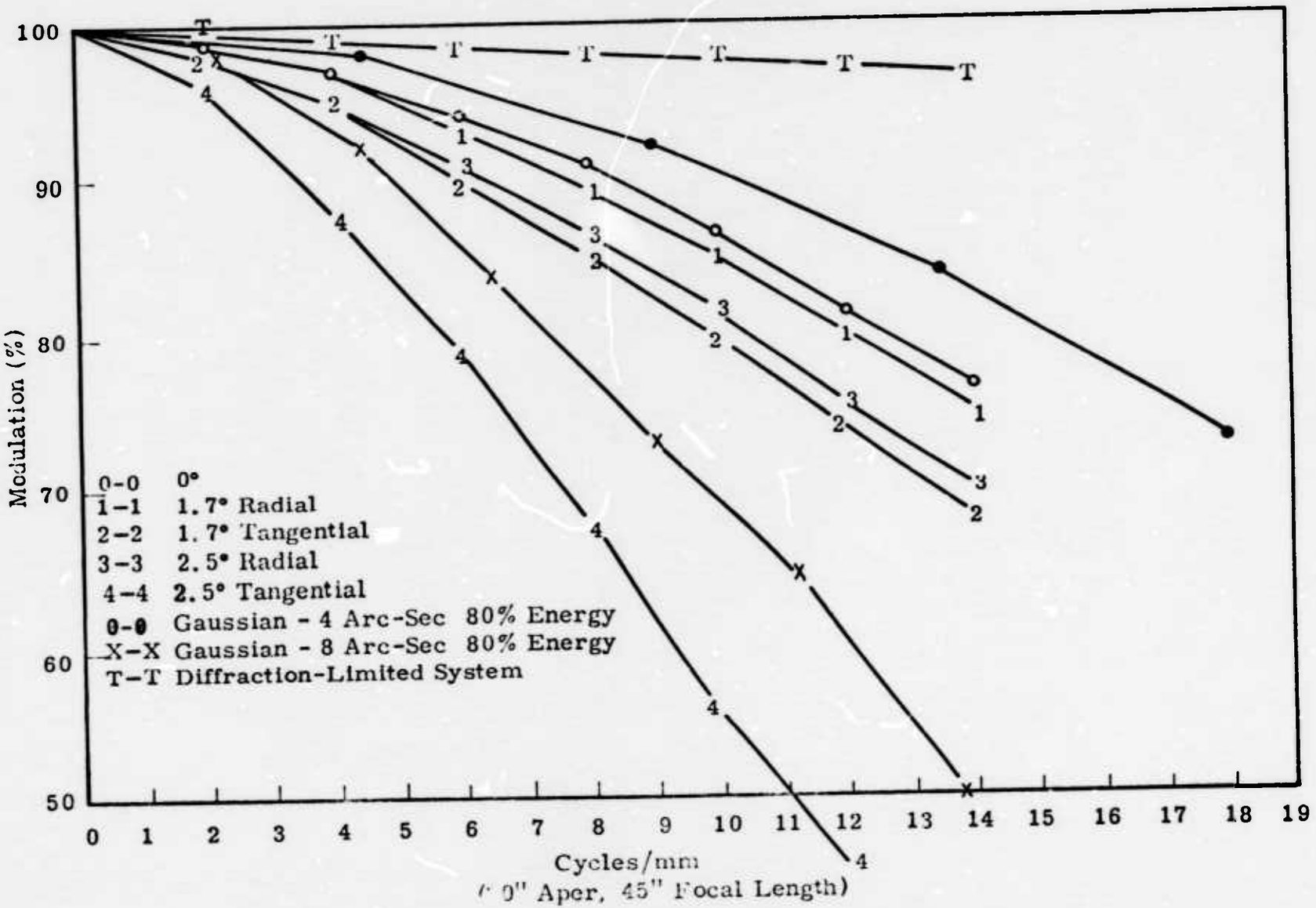

Figure 17. Monochromatic Modulation Transfer Function, System B

[illegible] ORIGINAL [illegible]
CYCLE 0

[illegible] TIC O.T.F.

WAVELENGTH 0.000[illegible] FIELD 0.0 0.0

LINES PARALLEL TO [illegible]

*FREQ	[illegible]	MTF	[illegible]	[illegible]	PHASE
2.	[illegible]	[illegible]	[illegible]	0.0	0.0
4.	[illegible]	[illegible]	[illegible]	0.0	0.0
6.	[illegible]	[illegible]	[illegible]	0.0	0.0
8.	[illegible]	[illegible]	[illegible]	0.0	0.0
10.	[illegible]	[illegible]	[illegible]	0.0	0.0
12.	[illegible]	[illegible]	[illegible]	0.0	0.0
14.	[illegible]	[illegible]	[illegible]	0.0	0.0
16.	[illegible]	[illegible]	[illegible]	0.0	0.0
18.	[illegible]	[illegible]	[illegible]	0.0	0.0
20.	[illegible]	[illegible]	[illegible]	0.0	0.0
22.	[illegible]	[illegible]	[illegible]	0.0	0.0
24.	[illegible]	[illegible]	[illegible]	0.0	0.0
26.	[illegible]	[illegible]	[illegible]	0.0	0.0
28.	[illegible]	[illegible]	[illegible]	0.0	0.0
30.	[illegible]	[illegible]	[illegible]	0.0	0.0
32.	[illegible]	[illegible]	[illegible]	0.0	0.0
34.	[illegible]	[illegible]	[illegible]	0.0	0.0
36.	[illegible]	[illegible]	[illegible]	0.0	0.0
38.	[illegible]	[illegible]	[illegible]	0.0	0.0
40.	[illegible]	[illegible]	[illegible]	0.0	0.0
42.	[illegible]	[illegible]	[illegible]	0.0	0.0
44.	[illegible]	[illegible]	[illegible]	0.0	0.0
46.	[illegible]	[illegible]	[illegible]	0.0	0.0
48.	[illegible]	[illegible]	[illegible]	0.0	0.0
50.	[illegible]	[illegible]	[illegible]	0.0	0.0
52.	[illegible]	[illegible]	[illegible]	0.0	0.0
54.	[illegible]	[illegible]	[illegible]	0.0	0.0
56.	[illegible]	[illegible]	[illegible]	0.0	0.0
58.	[illegible]	[illegible]	[illegible]	0.0	0.0
60.	[illegible]	[illegible]	[illegible]	0.0	0.0
62.	[illegible]	[illegible]	[illegible]	0.0	0.0
64.	[illegible]	[illegible]	[illegible]	0.0	0.0
66.	[illegible]	[illegible]	[illegible]	0.0	0.0

*The spatial frequencies are for a 20" aperture, 30" focal length. Therefore, multiply by 2/3 for a 30" aperture, 45" focal length.

AMBER ORIGINAL RAUL SYSTEM A MTF 11:33:31 06/14/74
CYCLE 0

MONOCHROMATIC O.T.F.

WAVELENGTH 0.0005875 FIELD 1.70 0.0

	LINES PARALLEL TO RADIAL DIR.						LINES PARALLEL TO TANGENTIAL DIR.				
* FREQ	THEOR	MTF	REAL	IMAG	PHASE		THEOR	MTF	REAL	IMAG	PHASE
2.	0.985	0.972	0.972	0.0	0.0	*	0.972	0.970	0.970	-0.033	-0.034
4.	0.940	0.917	0.917	0.0	0.0	*	0.940	0.916	0.917	-0.038	-0.041
6.	0.884	0.835	0.835	0.0	0.0	*	0.884	0.874	0.874	-0.029	-0.032
8.	0.819	0.733	0.733	0.0	0.0	*	0.819	0.841	0.841	-0.019	-0.023
10.	0.747	0.646	0.646	0.0	0.0	*	0.747	0.815	0.815	-0.013	-0.017
12.	0.669	0.796	0.796	0.0	0.0	*	0.669	0.797	0.797	-0.010	-0.013
14.	0.588	0.773	0.773	0.0	0.0	*	0.588	0.783	0.782	-0.010	-0.013
16.	0.504	0.751	0.751	0.0	0.0	*	0.502	0.754	0.754	-0.013	-0.017
18.	0.419	0.730	0.730	0.0	0.0	*	0.418	0.730	0.730	-0.016	-0.021
20.	0.334	0.714	0.714	0.0	0.0	*	0.334	0.713	0.713	-0.018	-0.025
22.	0.248	0.725	0.725	0.0	0.0	*	0.248	0.730	0.724	-0.020	-0.027
24.	0.161	0.718	0.718	0.0	0.0	*	0.161	0.717	0.717	-0.021	-0.029
26.	0.074	0.704	0.704	0.0	0.0	*	0.074	0.704	0.704	-0.021	-0.031
28.	0.013	0.542	0.542	0.0	0.0	*	0.013	0.542	0.542	-0.021	-0.031
30.	0.021	0.630	0.630	0.0	0.0	*	0.021	0.630	0.630	-0.020	-0.030
32.	0.116	0.653	0.653	0.0	0.0	*	0.116	0.653	0.653	-0.019	-0.028
34.	0.211	0.657	0.657	0.0	0.0	*	0.211	0.657	0.657	-0.017	-0.025
36.	0.305	0.654	0.654	0.0	0.0	*	0.305	0.647	0.647	-0.015	-0.023
38.	0.401	0.650	0.650	0.0	0.0	*	0.400	0.637	0.638	-0.012	-0.020
40.	0.495	0.647	0.647	0.0	0.0	*	0.495	0.627	0.625	-0.010	-0.017
42.	0.590	0.639	0.639	0.0	0.0	*	0.590	0.617	0.617	-0.009	-0.014
44.	0.685	0.630	0.630	0.0	0.0	*	0.685	0.607	0.607	-0.007	-0.011
46.	0.780	0.622	0.622	0.0	0.0	*	0.779	0.597	0.597	-0.005	-0.009
48.	0.874	0.613	0.613	0.0	0.0	*	0.874	0.588	0.588	-0.003	-0.006
50.	0.969	0.605	0.605	0.0	0.0	*	0.969	0.578	0.578	-0.004	-0.006
52.	1.064	0.596	0.596	0.0	0.0	*	0.964	0.569	0.569	-0.003	-0.005
54.	1.159	0.588	0.588	0.0	0.0	*	0.959	0.559	0.559	-0.002	-0.004
56.	1.253	0.579	0.579	0.0	0.0	*	1.053	0.549	0.549	-0.001	-0.002
58.	1.348	0.571	0.571	0.0	0.0	*	1.048	0.539	0.539	-0.000	-0.001
60.	1.443	0.562	0.562	0.0	0.0	*	1.043	0.489	0.489	-0.006	-0.012
62.	1.538	0.551	0.551	0.0	0.0	*	1.138	0.484	0.484	-0.007	-0.015
64.	1.632	0.539	0.539	0.0	0.0	*	1.232	0.483	0.483	-0.009	-0.019
66.	1.727	0.527	0.527	0.0	0.0	*	1.327	0.480	0.480	-0.010	-0.021

*See Note on Pg. 44

SHIFT ORIGINAL ADJ SYSTEM A MTF 11:33:31 06/14/74
CYCLE 0

MONOCHROMATIC O.T.F.

WAVELENGTH 0.000-875 FIELD 2.50 0.0

LINES PARALLEL TO RADIAL DIR.

*FREQ	THEOR	MTF	REAL	IMAG	PHASE
2.	0.993	0.989	0.989	0.0	0.0
4.	0.970	0.956	0.956	0.0	0.0
6.	0.940	0.909	0.909	0.0	0.0
8.	0.904	0.858	0.858	0.0	0.0
10.	0.863	0.804	0.804	0.0	0.0
12.	0.819	0.746	0.746	0.0	0.0
14.	0.773	0.773	0.773	0.0	0.0
16.	0.724	0.750	0.750	0.0	0.0
18.	0.673	0.748	0.748	0.0	0.0
20.	0.622	0.737	0.737	0.0	0.0
22.	0.572	0.720	0.720	0.0	0.0
24.	0.523	0.719	0.719	0.0	0.0
26.	0.476	0.707	0.707	0.0	0.0
28.	0.431	0.695	0.695	0.0	0.0
30.	0.389	0.680	0.680	0.0	0.0
32.	0.350	0.662	0.662	0.0	0.0
34.	0.314	0.643	0.643	0.0	0.0
36.	0.281	0.625	0.625	0.0	0.0
38.	0.251	0.601	0.601	0.0	0.0
40.	0.224	0.584	0.584	0.0	0.0
42.	0.200	0.567	0.567	0.0	0.0
44.	0.179	0.548	0.548	0.0	0.0
46.	0.160	0.534	0.534	0.0	0.0
48.	0.143	0.527	0.527	0.0	0.0
50.	0.128	0.520	0.520	0.0	0.0
52.	0.115	0.513	0.513	0.0	0.0
54.	0.103	0.508	0.508	0.0	0.0
56.	0.093	0.500	0.500	0.0	0.0
58.	0.084	0.493	0.493	0.0	0.0
60.	0.076	0.490	0.490	0.0	0.0
62.	0.069	0.484	0.484	0.0	0.0
64.	0.062	0.477	0.477	0.0	0.0
66.	0.057	0.473	0.473	0.0	0.0

LINES PARALLEL TO TANGENTIAL DIR.

	THEOR	MTF	REAL	IMAG	PHASE
*	0.993	0.989	0.989	-0.045	-0.047
*	0.970	0.956	0.956	-0.053	-0.055
*	0.940	0.909	0.909	-0.048	-0.049
*	0.904	0.858	0.858	-0.043	-0.049
*	0.863	0.804	0.804	-0.043	-0.053
*	0.819	0.746	0.746	-0.042	-0.057
*	0.773	0.702	0.702	-0.042	-0.053
*	0.724	0.707	0.707	-0.042	-0.059
*	0.673	0.711	0.711	-0.042	-0.059
*	0.622	0.735	0.735	-0.042	-0.057
*	0.572	0.741	0.740	-0.043	-0.058
*	0.523	0.727	0.725	-0.043	-0.059
*	0.476	0.714	0.713	-0.043	-0.060
*	0.431	0.701	0.700	-0.043	-0.062
*	0.389	0.684	0.683	-0.043	-0.063
*	0.350	0.665	0.664	-0.043	-0.065
*	0.314	0.645	0.644	-0.043	-0.067
*	0.281	0.625	0.624	-0.043	-0.068
*	0.251	0.601	0.601	-0.043	-0.071
*	0.224	0.584	0.583	-0.043	-0.073
*	0.200	0.567	0.566	-0.043	-0.075
*	0.179	0.548	0.547	-0.043	-0.078
*	0.160	0.534	0.533	-0.043	-0.080
*	0.143	0.527	0.526	-0.043	-0.082
*	0.128	0.520	0.519	-0.043	-0.084
*	0.115	0.513	0.512	-0.043	-0.086
*	0.103	0.508	0.507	-0.043	-0.088
*	0.093	0.500	0.499	-0.043	-0.090
*	0.084	0.493	0.492	-0.043	-0.092
*	0.076	0.490	0.489	-0.043	-0.094
*	0.069	0.484	0.483	-0.043	-0.096
*	0.062	0.477	0.476	-0.043	-0.098
*	0.057	0.473	0.472	-0.043	-0.100

*See Note on Pg. 44

PAUL AMBER
CYCLE 26 16:03:30 06/06/7

MONOCHROMATIC O.T.F. SYSTEM B

WAVELENGTH 0.0005876 FIELD 0.0 0.0

LINES PARALLEL TO RADIAL DIR.

FREQ	THEOR	MTF	REAL	IMAG	PHASE
2.	0.995	0.990	0.990	0.0	0.0
4.	0.990	0.971	0.971	0.0	0.0
6.	0.985	0.943	0.943	0.0	0.0
8.	0.980	0.908	0.908	0.0	0.0
10.	0.975	0.865	0.865	0.0	0.0
12.	0.970	0.816	0.816	0.0	0.0
14.	0.966	0.761	0.761	0.0	0.0

WAVELENGTH 0.0005876 FIELD 1.70 0.0

LINES PARALLEL TO RADIAL DIR.

FREQ	THEOR	MTF	REAL	IMAG	PHASE
2.	0.995	0.989	0.989	0.0	0.0
4.	0.990	0.965	0.965	0.0	0.0
6.	0.985	0.933	0.933	0.0	0.0
8.	0.980	0.893	0.893	0.0	0.0
10.	0.975	0.849	0.849	0.0	0.0
12.	0.970	0.803	0.803	0.0	0.0
14.	0.965	0.754	0.754	0.0	0.0

LINES PARALLEL TO TANGENTIAL DIR.

THEOR	MTF	REAL	IMAG	PHASE
0.995	0.982	0.979	-0.089	-0.090
0.990	0.948	0.934	-0.161	-0.171
0.985	0.904	0.877	-0.219	-0.244
0.980	0.855	0.813	-0.266	-0.317
0.975	0.801	0.741	-0.305	-0.391
0.970	0.743	0.663	-0.335	-0.469
0.965	0.681	0.581	-0.356	-0.549

WAVELENGTH 0.0005876 FIELD 2.50 0.0

LINES PARALLEL TO RADIAL DIR.

FREQ	THEOR	MTF	REAL	IMAG	PHASE
2.	0.995	0.984	0.984	0.0	0.0
4.	0.990	0.949	0.949	0.0	0.0
6.	0.985	0.906	0.906	0.0	0.0
8.	0.980	0.861	0.861	0.0	0.0
10.	0.975	0.816	0.816	0.0	0.0
12.	0.970	0.769	0.769	0.0	0.0
14.	0.965	0.721	0.721	0.0	0.0

LINES PARALLEL TO TANGENTIAL DIR.

THEOR	MTF	REAL	IMAG	PHASE
0.995	0.961	0.957	-0.083	-0.087
0.990	0.883	0.873	-0.134	-0.152
0.985	0.788	0.769	-0.172	-0.219
0.980	0.678	0.647	-0.204	-0.305
0.975	0.562	0.513	-0.224	-0.419
0.970	0.450	0.377	-0.247	-0.581
0.965	0.357	0.245	-0.259	-0.814

In order to achieve a truly apochromatic system, a combination of unusual glasses must be used, such as KzFS-2 and SK14. With all these considerations, the final system will have six aspheric surfaces a three-glass element corrector. The estimated optical efficiency less the obsuration effects is shown in Figure 18 as a function of wavelength with the anticipated spectral content of the signal.

4.3.2 Variation #1 of Baker-Schmidt Cassegrain

Due to the complexity of the above system and the use of special glasses, we tried a completely new approach as shown in Figure 19. As the first step, we replaced the three-element corrector of the previous system with an afocal doublet of the same common glass (BK-7) that fulfills the achromatic condition:

ϕ_1 and ϕ_2 power of the elements

ν_1 and ν_2 disperstion (glass)

$$\frac{\phi 1}{Y1} + \frac{\phi 2}{Y2} = 0$$

Therefore, there is no chromatic aberration, but we have the possibility of compensating for the spherical aberration and coma of the primary mirror.

The second corrector is also designed in such a way that the marginal ray coming from the secondary mirror is aimed at the first principal point; therefore, the outcoming ray is parallel to the previous one. That condition does not affect the spherical and longitudinal color correction but, because of the exit pupil position it allows us the correction of the residual astigmatism and lateral color. The general distribution of power is also established in such a manner that the Petzval condition is corrected.

A system with these characteristics will naturally have some loss in transmission as compared to the first system (Figure 15) but, at the same time, it will have the manufacturing advantage of not having aspherical surfaces and of using a common glass for all elements which should be easier to procure in large diameters.

Again, two different back focal lengths were investigated, one with a 3" separation between the last optical element (field flattener) (System C, see Figure 19) one with a 6" separation (System D, see Figure 10).

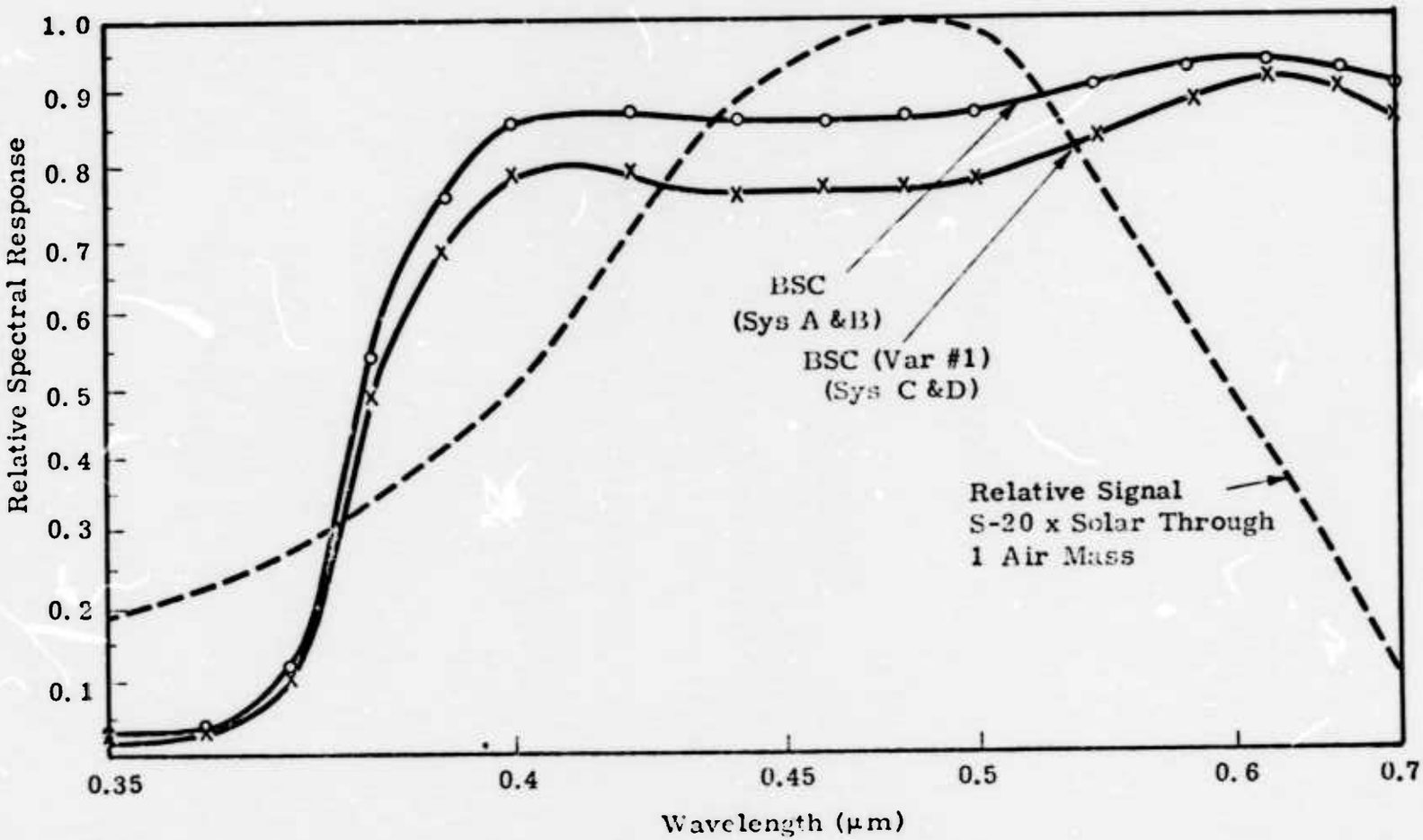

Figure 18. Estimated System Spectral Response

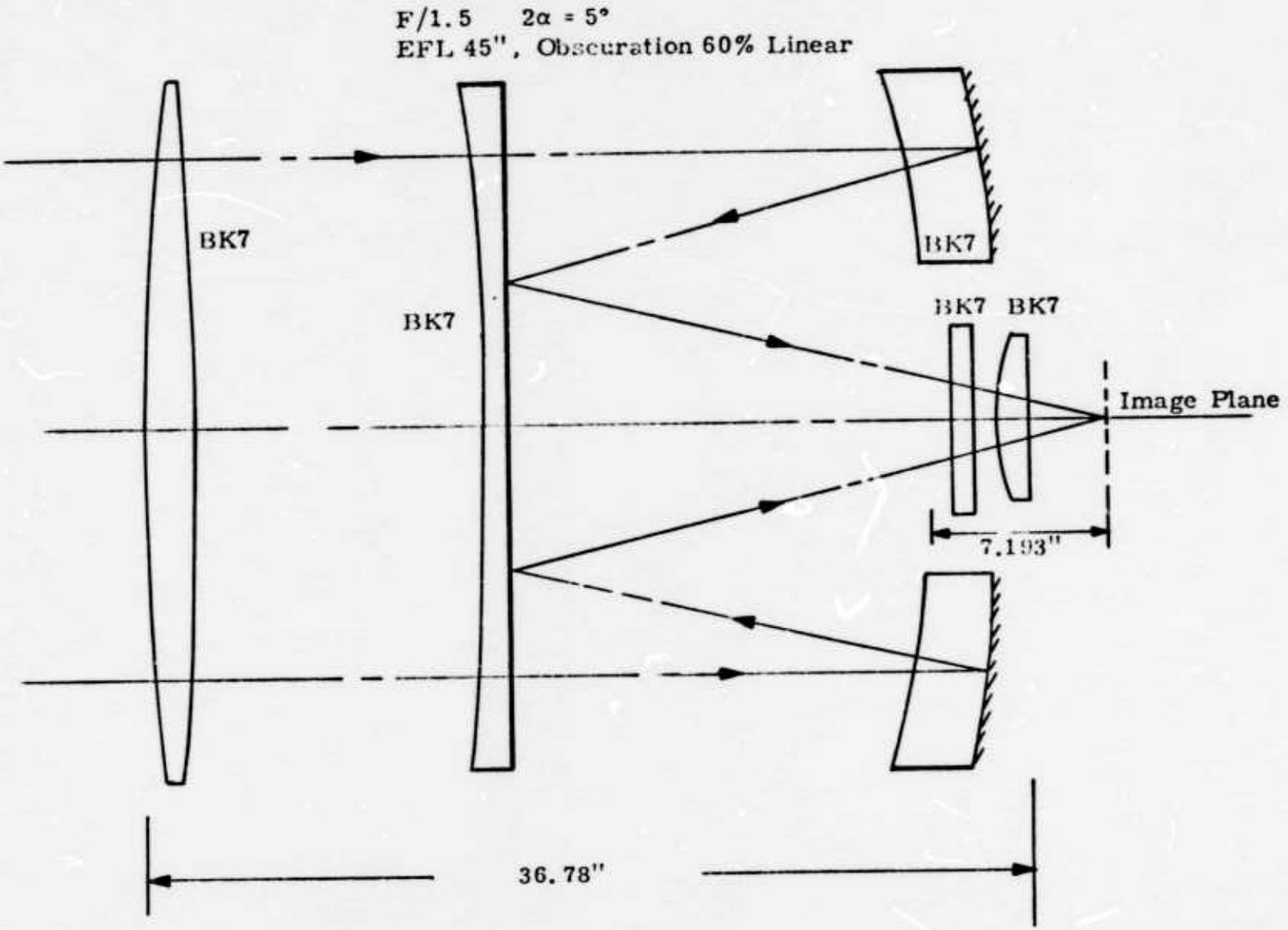

Figure 19a. System C

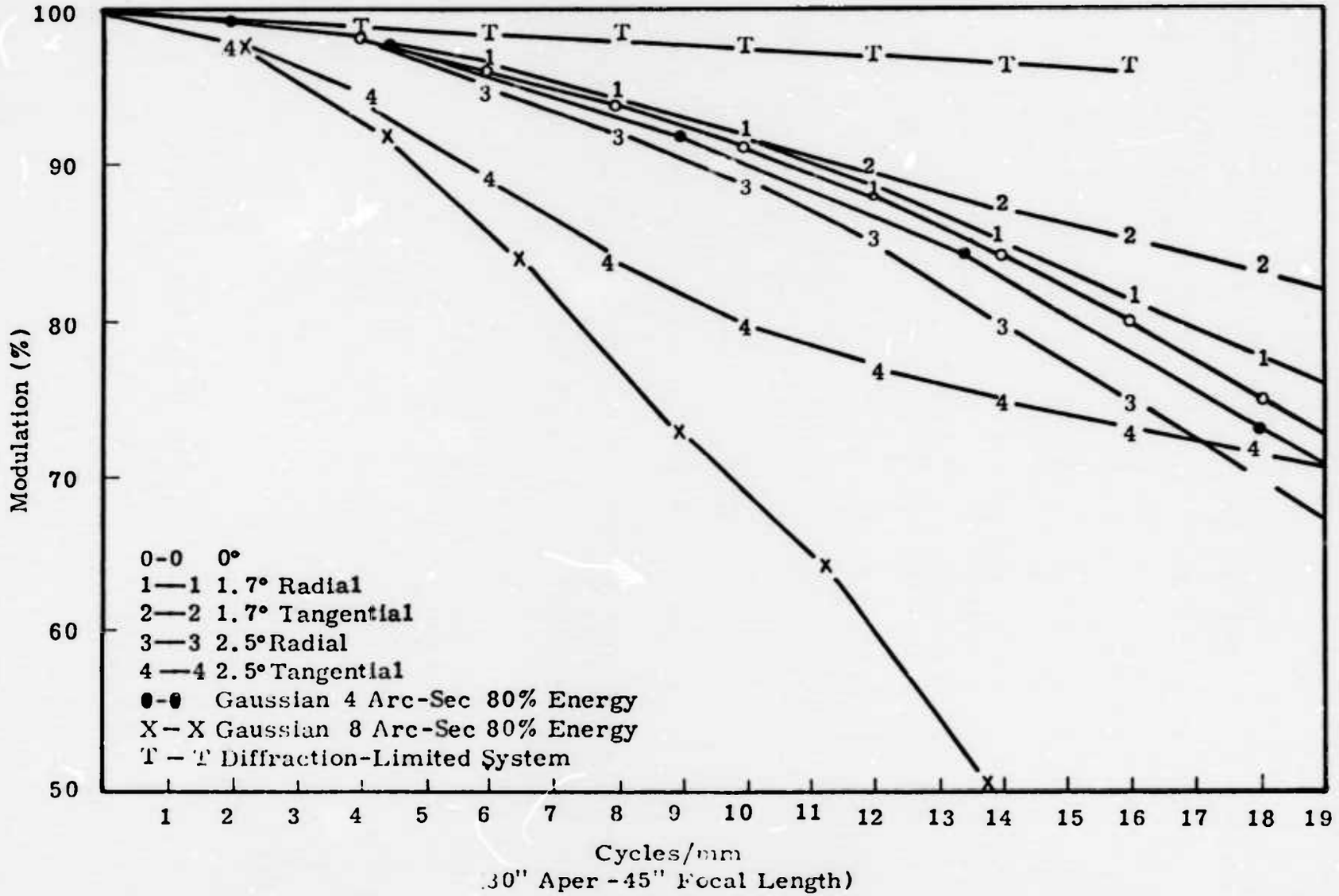

Figure 19b. Monochromatic Modulation Transfer Function, System C

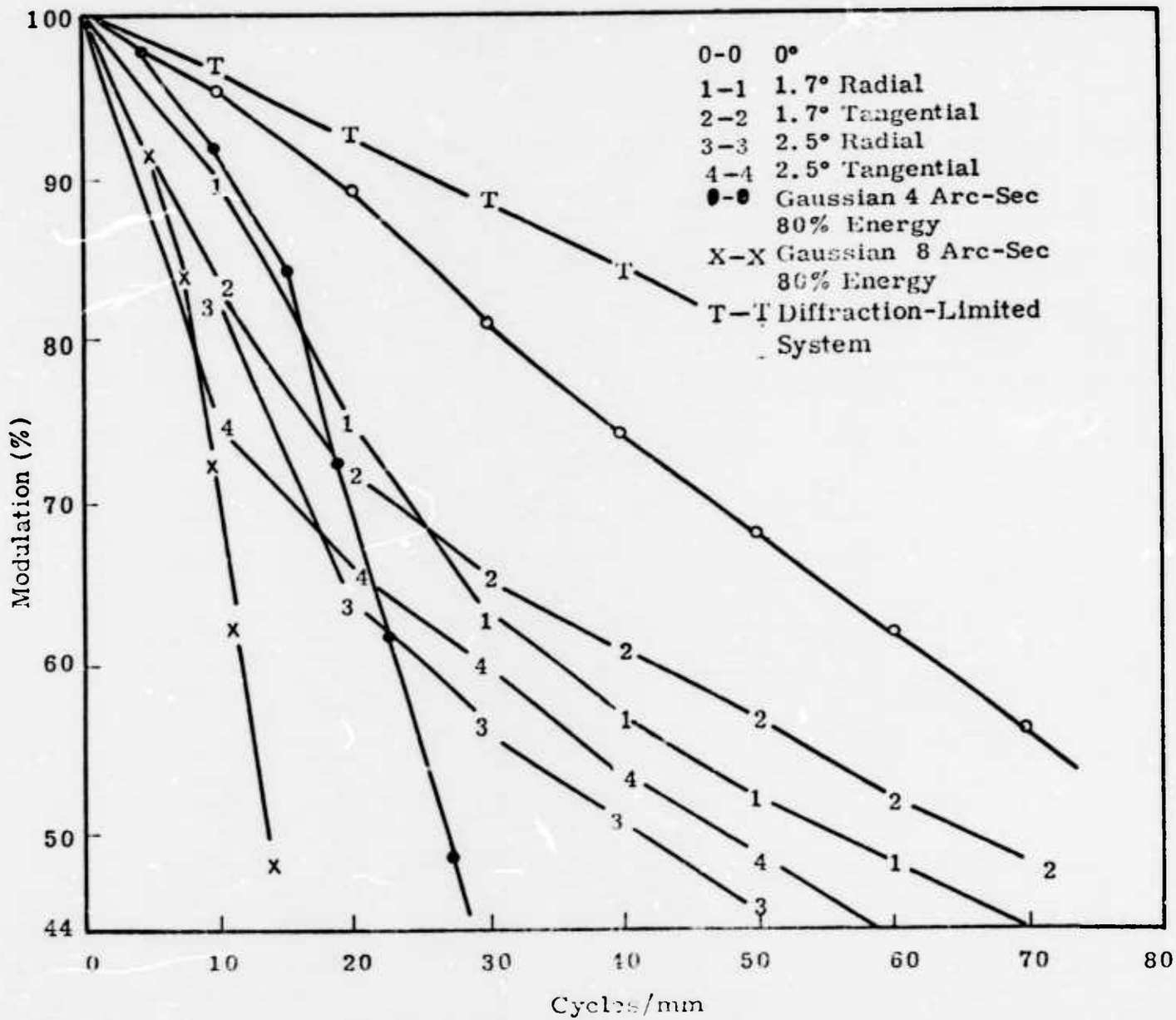

Figure 20. Modulation Transfer Function, System D

In addition to the monochromatic OTF, System C was explored for the OTF at two other wavelengths. Appropriate tables follow.

4.3.3 Line Spread Functions

In addition to the MTF responses, line spread functions were computed for systems A (Figure 21) and D (Figure 22). These plots show the response of the convolution of the image of a point source with a slit considerabily smaller than the image. Thus, this function is a measurement of the spot diameter or energy density in the focal plane. The convention and coordinate defintions are given in Figure 23 and the results are given in the following tables.

The high frequency ripple in the figures is the result of the digital form of the calculation and not a real phenomenon. For the tables, Z is the position in microns, I is the relative intensity with the volume defined by the slit and the spatial energy distribution, and DE is the percentage of the total energy contained within the slit volume and is defined by the two position points. It should be noted that in all cases, more than 80% of the energy is contained within the total slit investigated. This is shown by the energy scan number on the bottom of each table and is summarized below..

	% Within 22μ Slit Center On Point Image	
Line Spread Function	SYS A* For 30" Focal Length	SYS D For 45" Focal Length
0°	94	98
1.7°R	95	94
1.7°T	94	94
2.5°R	95	94
2.5°T	94	93

*For 45" Focal Length, This % of Energy is within a 33-μ Slit.

The first moment of energy is the centroid position of the energy relative to the geometric center.

RAUL
CYCLE 5

MONOCHROMATIC O.T.F. SYSTEM C

WAVELENGTH 0.0005876 FIELD 0.0 0.0

LINES PARALLEL TO RADIAL DIR.

FREQ	THEOR	MTF	REAL	IMAG	PHASE
2.	0.995	0.992	0.992	0.0	0.0
4.	0.980	0.979	0.979	0.0	0.0
6.	0.964	0.960	0.960	0.0	0.0
8.	0.979	0.937	0.937	0.0	0.0
10.	0.974	0.908	0.908	0.0	0.0
12.	0.969	0.875	0.875	0.0	0.0
14.	0.963	0.838	0.838	0.0	0.0
16.	0.958	0.797	0.797	0.0	0.0
18.	0.953	0.752	0.752	0.0	0.0
20.	0.948	0.705	0.705	0.0	0.0

WAVELENGTH 0.0005876 FIELD 1.70 0.0

	LINES PARALLEL TO RADIAL DIR.						LINES PARALLEL TO TANGENTIAL DIR.				
FREQ	THEOR	MTF	REAL	IMAG	PHASE		THEOR	MTF	REAL	IMAG	PHAS
2.	0.995	0.992	0.992	0.0	0.0	*	0.995	0.992	0.989	-0.085	-0.0
4.	0.980	0.980	0.980	0.0	0.0	*	0.984	0.977	0.969	-0.130	-0.13
6.	0.964	0.963	0.963	0.0	0.0	*	0.964	0.954	0.939	-0.195	-0.20
8.	0.979	0.942	0.942	0.0	0.0	*	0.979	0.937	0.900	-0.259	-0.2
10.	0.974	0.916	0.916	0.0	0.0	*	0.974	0.914	0.855	-0.322	-0.3
12.	0.969	0.887	0.887	0.0	0.0	*	0.968	0.890	0.804	-0.383	-0.4
14.	0.963	0.853	0.853	0.0	0.0	*	0.963	0.867	0.747	-0.441	-0.53
16.	0.958	0.817	0.817	0.0	0.0	*	0.958	0.845	0.686	-0.496	-0.62
18.	0.953	0.778	0.778	0.0	0.0	*	0.953	0.827	0.622	-0.545	-0.72
20.	0.948	0.736	0.736	0.0	0.0	*	0.947	0.810	0.554	-0.590	0.81

WAVELENGTH 0.0005876 FIELD 2.50 0.0

	LINES PARALLEL TO RADIAL DIR.						LINES PARALLEL TO TANGENTIAL DIR.				
FREQ	THEOR	MTF	REAL	IMAG	PHASE		THEOR	MTF	REAL	IMA	PHA
2.	0.995	0.991	0.991	0.0	0.0	*	0.995	0.982	0.979	-0.07	-0.07
4.	0.989	0.975	0.975	0.0	0.0	*	0.984	0.942	0.930	-0.151	-0.16
6.	0.964	0.951	0.951	0.0	0.0	*	0.964	0.892	0.860	-0.235	-0.25
8.	0.979	0.922	0.922	0.0	0.0	*	0.979	0.841	0.777	-0.323	-0.39
10.	0.974	0.896	0.896	0.0	0.0	*	0.973	0.799	0.686	-0.410	-0.53
12.	0.968	0.868	0.868	0.0	0.0	*	0.968	0.768	0.592	-0.490	-0.65
14.	0.963	0.800	0.800	0.0	0.0	*	0.963	0.747	0.495	-0.559	-0.84
16.	0.958	0.751	0.751	0.0	0.0	*	0.958	0.729	0.397	-0.612	-0.9
18.	0.953	0.700	0.700	0.0	0.0	*	0.952	0.713	0.297	-0.648	-1.1
20.	0.947	0.646	0.646	0.0	0.0	*	0.947	0.696	0.196	-0.668	-1.2

SYSTEM D

0°

LINES PARALLEL TO RADIAL DIR. X =

FREQ	THEOR	DIF	REAL	IMAG	PHASE
10.	0.076	0.000	0.000	0.0	0.0
20.	0.000	0.000	0.000	0.0	0.0
30.	0.021	0.014	0.014	0.0	0.0
40.	0.000	0.000	0.000	0.0	0.0
50.	0.000	0.001	0.001	0.0	0.0
60.	0.003	0.010	0.010	0.0	0.0
70.	0.017	0.005	0.005	0.0	0.0

1.7°

LINES PARALLEL TO RADIAL DIR.

FREQ	THEOR	DIF	REAL	IMAG	PHASE
10.	0.076	0.049	0.049	0.0	0.0
20.	0.000	0.000	0.000	0.0	0.0
30.	0.021	0.021	0.021	0.0	0.0
40.	0.000	0.007	0.007	0.0	0.0
50.	0.000	0.002	0.002	0.0	0.0
60.	0.003	0.000	0.000	0.0	0.0
70.	0.017	0.002	0.002	0.0	0.0

LINES PARALLEL TO TANGENTIAL DIR.

	THEOR	DIF	REAL	IMAG	PHASE
*	0.076	0.034	0.024	0.130	0.157
*	0.000	0.717	0.714	0.055	0.091
*	0.021	0.000	0.000	0.000	0.000
*	0.000	0.004	0.004	0.000	0.000
*	0.004	0.000	0.000	-0.009	-0.010
*	0.003	0.000	0.000	-0.017	-0.035
*	0.017	0.000	0.000	-0.025	-0.000

2.5°

LINES PARALLEL TO RADIAL DIR.

FREQ	THEOR	DIF	REAL	IMAG	PHASE
10.	0.076	0.052	0.052	0.0	0.0
20.	0.000	0.000	0.000	0.0	0.0
30.	0.021	0.000	0.000	0.0	0.0
40.	0.000	0.000	0.000	0.0	0.0
50.	0.000	0.000	0.000	0.0	0.0
60.	0.003	0.000	0.000	0.0	0.0
70.	0.017	0.000	0.000	0.0	0.0

LINES PARALLEL TO TANGENTIAL DIR.

	THEOR	DIF	REAL	IMAG	PHASE
*	0.076	0.000	0.000	0.052	0.000
*	0.000	0.000	0.000	-0.000	-0.000
*	0.021	0.000	0.000	-0.000	-0.000
*	0.000	0.000	0.000	-0.000	-0.000
*	0.000	0.000	0.000	-0.000	-0.000
*	0.003	0.000	0.000	-0.000	-0.000
*	0.017	0.000	0.000	-0.000	-0.000

JL 15:24:47 06/07/74
CLE 5

NOCHROMATIC O.T.F. SYSTEM C

VELENGTH 0.0004861 FIELD 0.0 0.0

LINES PARALLEL TO RADIAL DIR.

EQ	THEOR	MTF	REAL	IMAG	PHASE
2.	0.995	0.992	0.992	0.0	0.0
4.	0.991	0.979	0.979	0.0	0.0
6.	0.987	0.959	0.959	0.0	0.0
8.	0.983	0.935	0.935	0.0	0.0
10.	0.978	0.906	0.905	0.0	0.0
12.	0.974	0.874	0.874	0.0	0.0
14.	0.970	0.839	0.839	0.0	0.0
16.	0.965	0.802	0.802	0.0	0.0
18.	0.961	0.763	0.763	0.0	0.0
20.	0.957	0.724	0.724	0.0	0.0

AVELENGTH 0.0004861 FIELD 1.70 0.0

	LINES PARALLEL TO RADIAL DIR.						LINES PARALLEL TO TANGENTIAL DIR.				
EQ	THEOR	MTF	REAL	IMAG	PHASE		THEOR	MTF	REAL	IMAG	PHASE
2.	0.995	0.990	0.990	0.0	0.0	*	0.995	0.981	0.980	-0.048	-0.049
4.	0.991	0.970	0.970	0.0	0.0	*	0.991	0.939	0.933	-0.108	-0.110
6.	0.987	0.941	0.941	0.0	0.0	*	0.987	0.884	0.868	-0.168	-0.171
8.	0.983	0.906	0.905	0.0	0.0	*	0.983	0.824	0.792	-0.241	-0.246
10.	0.978	0.865	0.865	0.0	0.0	*	0.978	0.761	0.713	-0.316	-0.419
12.	0.974	0.821	0.821	0.0	0.0	*	0.974	0.746	0.635	-0.392	-0.553
14.	0.970	0.776	0.776	0.0	0.0	*	0.970	0.721	0.558	-0.457	-0.680
16.	0.965	0.730	0.730	0.0	0.0	*	0.965	0.701	0.481	-0.510	-0.814
18.	0.961	0.685	0.685	0.0	0.0	*	0.961	0.682	0.404	-0.550	-0.936
20.	0.957	0.641	0.641	0.0	0.0	*	0.956	0.663	0.325	-0.577	-1.055

AVELENGTH 0.0004861 FIELD 2.50 0.0

	LINES PARALLEL TO RADIAL DIR.						LINES PARALLEL TO TANGENTIAL DIR.				
EQ	THEOR	MTF	REAL	IMAG	PHASE		THEOR	MTF	REAL	IMAG	PHASE
2.	0.995	0.988	0.988	0.0	0.0	*	0.995	0.964	0.962	-0.066	-0.068
4.	0.991	0.960	0.960	0.0	0.0	*	0.991	0.885	0.872	-0.155	-0.176
6.	0.987	0.920	0.920	0.0	0.0	*	0.987	0.805	0.759	-0.265	-0.340
8.	0.983	0.871	0.871	0.0	0.0	*	0.982	0.752	0.645	-0.387	-0.541
10.	0.978	0.816	0.814	0.0	0.0	*	0.978	0.725	0.535	-0.490	-0.742
12.	0.974	0.758	0.758	0.0	0.0	*	0.974	0.705	0.422	-0.565	-0.930
14.	0.970	0.699	0.699	0.0	0.0	*	0.969	0.682	0.301	-0.612	-1.114
16.	0.965	0.642	0.642	0.0	0.0	*	0.965	0.654	0.173	-0.635	-1.305
18.	0.961	0.587	0.587	0.0	0.0	*	0.961	0.641	0.046	-0.639	-1.499
20.	0.957	0.535	0.535	0.0	0.0	*	0.956	0.627	-0.074	-0.623	-1.689

UL
CLE 5 SYSTEM C 15:24:47 06/07/74

NOCHROMATIC O.T.F.

AVELENGTH 0.0006563 FIELD 0.0 0.0

LINES PARALLEL TO RADIAL DIR.

FREQ	THEOR	MTF	REAL	IMAG	PHASE
2.	0.994	0.988	0.988	0.0	0.0
4.	0.988	0.962	0.962	0.0	0.0
6.	0.982	0.925	0.925	0.0	0.0
8.	0.977	0.877	0.877	0.0	0.0
10.	0.971	0.819	0.819	0.0	0.0
12.	0.965	0.753	0.753	0.0	0.0
14.	0.959	0.680	0.680	0.0	0.0
16.	0.953	0.602	0.602	0.0	0.0
18.	0.947	0.522	0.522	0.0	0.0
20.	0.942	0.441	0.441	0.0	0.0

ENGTH 0.0006563 FIELD 1.70 0.0

LINES PARALLEL TO RADIAL DIR.						LINES PARALLEL TO TANGENTIAL DIR.				
THEOR	MTF	REAL	IMAG	PHASE		THEOR	MTF	REAL	IMAG	PHASE
0.994	0.989	0.989	0.0	0.0	*	0.994	0.993	0.990	-0.073	-0.073
0.988	0.969	0.969	0.0	0.0	*	0.988	0.983	0.973	-0.144	-0.147
0.982	0.940	0.940	0.0	0.0	*	0.982	0.972	0.948	-0.215	-0.223
0.977	0.902	0.902	0.0	0.0	*	0.976	0.954	0.916	-0.282	-0.299
0.971	0.856	0.856	0.0	0.0	*	0.971	0.943	0.877	-0.347	-0.377
0.965	0.804	0.804	0.0	0.0	*	0.965	0.927	0.833	-0.408	-0.455
0.959	0.746	0.746	0.0	0.0	*	0.959	0.910	0.783	-0.464	-0.535
0.953	0.684	0.684	0.0	0.0	*	0.953	0.892	0.728	-0.515	-0.616
0.947	0.618	0.618	0.0	0.0	*	0.947	0.874	0.670	-0.561	-0.697
0.941	0.551	0.551	0.0	0.0	*	0.941	0.855	0.608	-0.601	-0.780

AVELENGTH 0.0006563 FIELD 2.50 0.0

LINES PARALLEL TO RADIAL DIR.						LINES PARALLEL TO TANGENTIAL DIR.				
FREQ	THEOR	MTF	REAL	IMAG	PHASE		THEOR	MTF	REAL	IMAG	PHASE
2.	0.994	0.989	0.989	0.0	0.0	*	0.994	0.987	0.984	-0.076	-0.078
4.	0.988	0.966	0.966	0.0	0.0	*	0.988	0.963	0.950	-0.154	-0.161
6.	0.982	0.934	0.934	0.0	0.0	*	0.982	0.930	0.901	-0.232	-0.252
8.	0.977	0.892	0.892	0.0	0.0	*	0.976	0.894	0.839	-0.310	-0.354
10.	0.971	0.842	0.842	0.0	0.0	*	0.970	0.859	0.768	-0.385	-0.465
12.	0.965	0.785	0.785	0.0	0.0	*	0.964	0.826	0.689	-0.455	-0.585
14.	0.959	0.722	0.722	0.0	0.0	*	0.959	0.794	0.606	-0.520	-0.709
16.	0.953	0.655	0.655	0.0	0.0	*	0.953	0.775	0.519	-0.575	-0.836
18.	0.947	0.586	0.586	0.0	0.0	*	0.947	0.755	0.431	-0.620	-0.963
20.	0.941	0.515	0.515	0.0	0.0	*	0.941	0.737	0.342	-0.653	-1.089

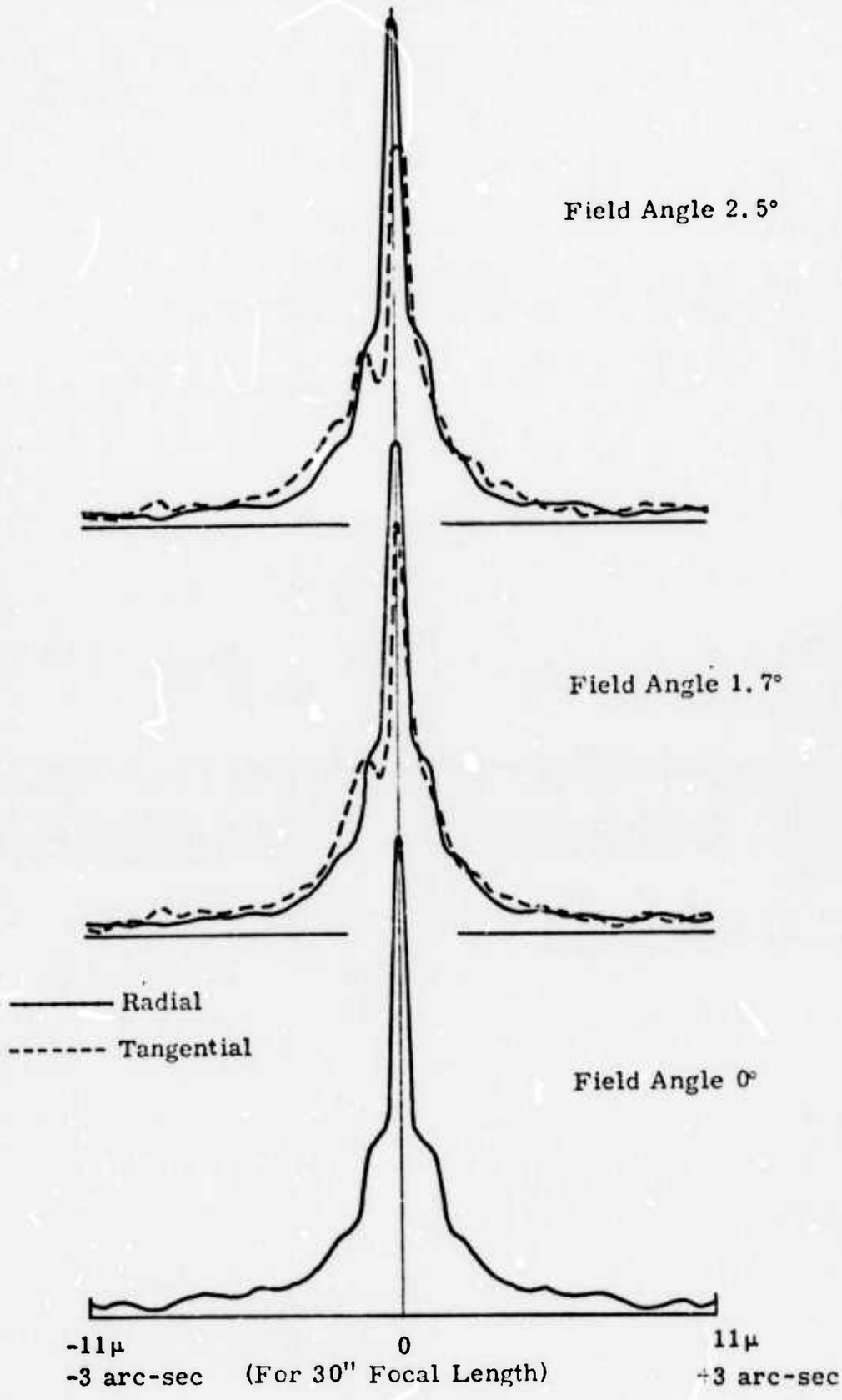

Figure 21. Line Spread Function for System A

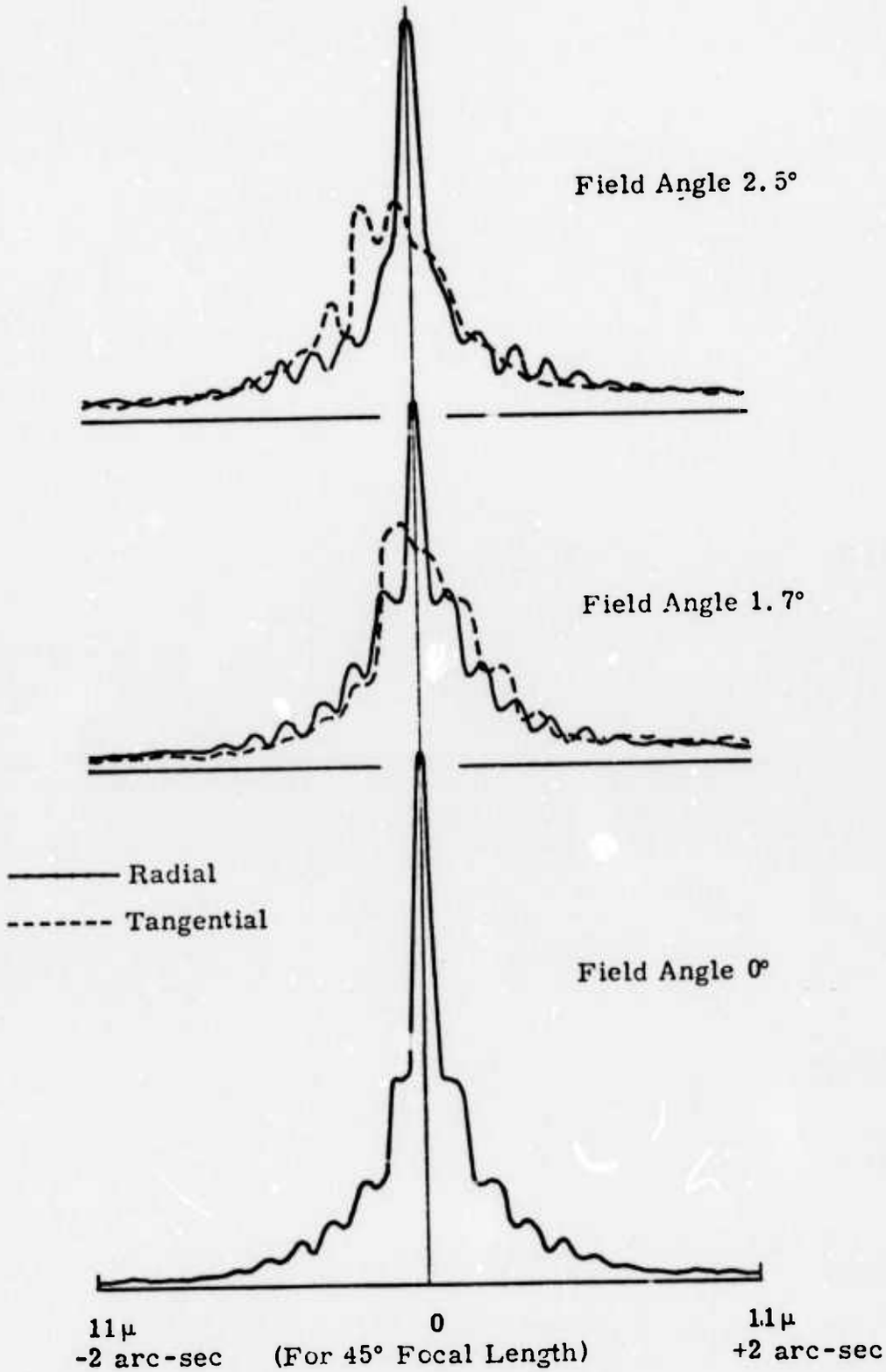

Figure 22 . Line Spread Functions for System D

MBER ORIGINAL HAUL SYS A 11:24:03 06/14/74
YCLE 0

INE SPREAD FUNCTION

AVELENGTH 0.0005876 E.F.L. 702.00 FIELD 0.0

IM. FREQ. 1134.62 CYCLES/MM NORMALIZING FACTOR 3.532

ANGENTIAL SCAN

NO.	Z	I	DE
-100	-0.01102	0.0199	0.0063
-95	-0.01047	0.0104	0.0038
-90	-0.00992	0.0171	0.0065
-85	-0.00936	0.0137	0.0034
-80	-0.00881	0.0077	0.0025
-75	-0.00826	0.0081	0.0047
-70	-0.00771	0.0172	0.0068
-65	-0.00716	0.0232	0.0095
-60	-0.00661	0.0267	0.0085
-55	-0.00606	0.0234	0.0087
-50	-0.00551	0.0259	0.0104
-45	-0.00496	0.0328	0.0114
-40	-0.00441	0.0305	0.0111
-35	-0.00386	0.0352	0.0145
-30	-0.00331	0.0431	0.0167
-25	-0.00275	0.0630	0.0309
-20	-0.00220	0.0930	0.0300
-15	-0.00165	0.1093	0.0624
-10	-0.00110	0.2043	0.0951
-5	-0.00055	0.2342	0.1547
0	0.0	0.5836	0.1547
5	0.00055	0.2342	0.0651
10	0.00110	0.2043	0.0624
15	0.00165	0.1093	0.0300
20	0.00220	0.0930	0.0309
25	0.00275	0.0630	0.0167
30	0.00331	0.0431	0.0145
35	0.00386	0.0352	0.0111
40	0.00441	0.0305	0.0114
45	0.00496	0.0328	0.0104
50	0.00551	0.0259	0.0087
55	0.00606	0.0234	0.0085
60	0.00661	0.0267	0.0095
65	0.00716	0.0232	0.0068
70	0.00771	0.0172	0.0047
75	0.00825	0.0081	0.0025
80	0.00881	0.0077	0.0034
85	0.00936	0.0137	0.0065
90	0.00992	0.0171	0.0038
95	0.01047	0.0104	0.0063
100	0.01102	0.0199	0.0056

IRST MOMENT OF ENERGY -0.0002 ENERGY SUM 0.9411

SYM

MBER ORIGINAL RAUL *Tangential Scan* 11:24:03 06/14/74
YCLE 0

INE SPREAD FUNCTION

AVELENGTH 0.0005876 E.F.L. 762.00 FIELD 1.70

IM. FREQ. 1134.13 CYCLES/MM NORMALIZING FACTOR 3.532

ANGENTIAL SCAN

NO.	Z	I	DE
-100	-0.01102	0.0163	0.0060
-95	-0.01047	0.0133	0.0046
-90	-0.00992	0.0159	0.0052
-85	-0.00937	0.0120	0.0050
-80	-0.00882	0.0167	0.0050
-75	-0.00827	0.0122	0.0050
-70	-0.00772	0.0144	0.0052
-65	-0.00716	0.0193	0.0052
-60	-0.00661	0.0215	0.0067
-55	-0.00606	0.0209	0.0084
-50	-0.00551	0.0240	0.0091
-45	-0.00496	0.0288	0.0049
-40	-0.00441	0.0256	0.0098
-35	-0.00386	0.0336	0.0142
-30	-0.00331	0.0424	0.0161
-25	-0.00276	0.0605	0.0301
-20	-0.00220	0.0919	0.0247
-15	-0.00165	0.1090	0.0633
-10	-0.00110	0.2091	0.0666
-5	-0.00055	0.2398	0.1594
0	0.0	0.6027	0.1594
5	0.00055	0.2398	0.0666
10	0.00110	0.2091	0.0633
15	0.00165	0.1090	0.0247
20	0.00220	0.0919	0.0301
25	0.00276	0.0605	0.0161
30	0.00331	0.0424	0.0142
35	0.00386	0.0336	0.0098
40	0.00441	0.0256	0.0099
45	0.00496	0.0288	0.0091
50	0.00551	0.0240	0.0084
55	0.00606	0.0209	0.0067
60	0.00661	0.0215	0.0082
65	0.00716	0.0193	0.0052
70	0.00772	0.0144	0.0050
75	0.00827	0.0122	0.0050
80	0.00882	0.0167	0.0050
85	0.00937	0.0120	0.0052
90	0.00992	0.0159	0.0046
95	0.01047	0.0133	0.0060
100	0.01102	0.0163	0.0046

FIRST MOMENT OF ENERGY -0.0002 ENERGY SUM 0.9399

SYSTEM A RADIAL SCAN

MBER ORIGINAL RAUL 11:24:03 06/14/74
CYCLE 0

INE SPREAD FUNCTION

AVELENGTH 0.0005875 E.F.L. 762.00 FIELD 1.70

IM. FREQ. 1133.20 CYCLES/MM NORMALIZING FACTOR 3.532

ADIAL SCAN

NO.	Y	I	DE
-100	-0.01103	0.0139	0.0036
-95	-0.01046	0.0069	0.0044
-90	-0.00993	0.0173	0.0055
-85	-0.00938	0.0138	0.0053
-80	-0.00882	0.0172	0.0092
-75	-0.00827	0.0334	0.0111
-70	-0.00772	0.0224	0.0084
-65	-0.00717	0.0299	0.0103
-60	-0.00662	0.0245	0.0084
-55	-0.00607	0.0245	0.0094
-50	-0.00552	0.0310	0.0122
-45	-0.00496	0.0340	0.0117
-40	-0.00441	0.0351	0.0141
-35	-0.00386	0.0433	0.0144
-30	-0.00331	0.0553	0.0202
-25	-0.00276	0.0665	0.0344
-20	-0.00221	0.1121	0.0344
-15	-0.00165	0.1090	0.0626
-10	-0.00110	0.2139	0.0634
-5	-0.00055	0.1912	0.1266
0	0.0	0.5026	0.1464
5	0.00055	0.2556	0.0670
10	0.00110	0.1843	0.0593
15	0.00165	0.1211	0.0321
20	0.00221	0.0842	0.0297
25	0.00276	0.0743	0.0209
30	0.00331	0.0471	0.0159
35	0.00386	0.0465	0.0155
40	0.00441	0.0363	0.0113
45	0.00496	0.0321	0.0109
50	0.00552	0.0262	0.0088
55	0.00607	0.0259	0.0077
60	0.00662	0.0154	0.0053
65	0.00717	0.0170	0.0050
70	0.00772	0.0095	0.0040
75	0.00827	0.0150	0.0063
80	0.00882	0.0182	0.0070
85	0.00938	0.0208	0.0070
90	0.00993	0.0195	0.0070
95	0.01046	0.0175	0.0056
100	0.01103	0.0171	0.0051

FIRST MOMENT OF ENERGY -0.0002 ENERGY SUM 0.9522

SYSTEM A RADIAL SCAN

MBER ORIGINAL RAUL 11:24:03 06/14/74
YCLE 0

INE SPREAD FUNCTION

WAVELENGTH 0.0005876 E.F.L. 762.00 FIELD 2.50

IM. FREQ. 1131.47 CYCLES/MM NORMALIZING FACTOR 3.532

ADIAL SCAN

NO.	Y	I	DE
-100	-0.01105	0.0128	0.0035
-95	-0.01050	0.0118	0.0065
-90	-0.00994	0.0194	0.0057
-85	-0.00939	0.0165	0.0069
-80	-0.00884	0.0212	0.0094
-75	-0.00829	0.0324	0.0095
-70	-0.00773	0.0165	0.0075
-65	-0.00718	0.0271	0.0091
-60	-0.00663	0.0223	0.0082
-55	-0.00608	0.0247	0.0099
-50	-0.00552	0.0337	0.0127
-45	-0.00497	0.0335	0.0120
-40	-0.00442	0.0390	0.0154
-35	-0.00387	0.0488	0.0211
-30	-0.00331	0.0559	0.0239
-25	-0.00276	0.0850	0.0412
-20	-0.00221	0.1227	0.0375
-15	-0.00166	0.1278	0.0692
-10	-0.00110	0.2160	0.0589
-5	-0.00055	0.1755	0.1178
0	0.0	0.4607	0.1353
5	0.00055	0.2530	0.0687
10	0.00110	0.1763	0.0561
15	0.00166	0.1232	0.0344
20	0.00221	0.0845	0.0297
25	0.00276	0.0810	0.0233
30	0.00331	0.0490	0.0167
35	0.00387	0.0513	0.0161
40	0.00442	0.0340	0.0107
45	0.00497	0.0309	0.0091
50	0.00552	0.0178	0.0066
55	0.00608	0.0220	0.0062
60	0.00663	0.0109	0.0044
65	0.00718	0.0163	0.0051
70	0.00773	0.0109	0.0046
75	0.00829	0.0173	0.0071
80	0.00884	0.0221	0.0077
85	0.00939	0.0200	0.0068
90	0.00994	0.0202	0.0063
95	0.01050	0.0129	0.0049
100	0.01105	0.0178	0.0058

FIRST MOMENT OF ENERGY -0.0003 ENERGY SUM 0.9514

SVSA

MBER ORIGINAL RAUL TANGENTIAL SCAN 11:24:03 06/14/74
.YCLE 0

INE SPREAD FUNCTION

WAVELENGTH 0.0005876 E.F.L. 762.00 FIELD 2.50

IM. FREQ. 1133.56 CYCLES/MM NORMALIZING FACTOR 3.532

ANGENTIAL SCAN

NO.	Z	I	DE
-100	-0.01103	0.0162	0.0062
-95	-0.01048	0.0151	0.0052
-90	-0.00992	0.0150	0.0050
-85	-0.00937	0.0120	0.0054
-80	-0.00882	0.0156	0.0040
-75	-0.00827	0.0082	0.0041
-70	-0.00772	0.0130	0.0051
-65	-0.00717	0.0204	0.0088
-60	-0.00662	0.0223	0.0068
-55	-0.00606	0.0223	0.0092
-50	-0.00551	0.0253	0.0087
-45	-0.00496	0.0256	0.0092
-40	-0.00441	0.0235	0.0089
-35	-0.00386	0.0307	0.0132
-30	-0.00331	0.0392	0.0149
-25	-0.00276	0.0575	0.0295
-20	-0.00221	0.0911	0.0293
-15	-0.00165	0.1079	0.0639
-10	-0.00110	0.2128	0.0676
-5	-0.00055	0.2433	0.1031
0	0.0	0.5192	0.1031
5	0.00055	0.2433	0.0676
10	0.00110	0.2128	0.0539
15	0.00165	0.1079	0.0293
20	0.00221	0.0911	0.0295
25	0.00276	0.0575	0.0149
30	0.00331	0.0392	0.0132
35	0.00386	0.0307	0.0089
40	0.00441	0.0235	0.0092
45	0.00496	0.0256	0.0087
50	0.00551	0.0253	0.0092
55	0.00606	0.0223	0.0068
60	0.00662	0.0223	0.0088
65	0.00717	0.0204	0.0051
70	0.00772	0.0130	0.0041
75	0.00827	0.0082	0.0040
80	0.00882	0.0156	0.0054
85	0.00937	0.0120	0.0050
90	0.00992	0.0150	0.0052
95	0.01048	0.0151	0.0062
100	0.01103	0.0162	0.0048

FIRST MOMENT OF ENERGY -0.0002 ENERGY SUM 0.9405

AUL *All SPHERICAL* SYS D 10:48:50 07/09/74
CYCLE 46

INE SPREAD FUNCTION.

AVELENGTH 0.0005876 E.F.L. 1143.0 FIELD 0.0

LIM. FREQ. 1134.50 CYCLES/MM NORMALIZING FACTOR 3.532

ANGENTIAL SCAN

NO.	Z	I	DE
-100	-0.01102	0.0065	0.0020
-95	-0.01047	0.0056	0.0030
-90	-0.00992	0.0056	0.0027
-85	-0.00937	0.0073	0.0031
-80	-0.00881	0.0093	0.0032
-75	-0.00826	0.0084	0.0028
-70	-0.00771	0.0093	0.0039
-65	-0.00716	0.0100	0.0042
-60	-0.00661	0.0161	0.0070
-55	-0.00606	0.0170	0.0075
-50	-0.00551	0.0300	0.0104
-45	-0.00496	0.0261	0.0131
-40	-0.00441	0.0507	0.0158
-35	-0.00386	0.0352	0.0179
-30	-0.00331	0.0720	0.0247
-25	-0.00275	0.0652	0.0326
-20	-0.00220	0.1173	0.0378
-15	-0.00165	0.1131	0.0657
-10	-0.00110	0.2328	0.0725
-5	-0.00055	0.2381	0.1599
0	0.0	0.5125	0.1599
5	0.00055	0.2381	0.0725
10	0.00110	0.2328	0.0657
15	0.00165	0.1131	0.0378
20	0.00220	0.1173	0.0326
25	0.00275	0.0652	0.0247
30	0.00331	0.0720	0.0179
35	0.00386	0.0352	0.0158
40	0.00441	0.0507	0.0131
45	0.00496	0.0261	0.0104
50	0.00551	0.0300	0.0075
55	0.00606	0.0170	0.0070
60	0.00661	0.0161	0.0042
65	0.00716	0.0100	0.0039
70	0.00771	0.0093	0.0028
75	0.00826	0.0084	0.0032
80	0.00881	0.0093	0.0031
85	0.00937	0.0073	0.0027
90	0.00992	0.0056	0.0030
95	0.01047	0.0056	0.0020
100	0.01102	0.0065	0.0017

FIRST MOMENT OF ENERGY -0.0002 ENERGY SUM 0.9819

OY51J

RAUL ALL SPHERICAL TANGENTIAL SCAN 10:48:50 07/09/74
CYCLE 46

LINE SPREAD FUNCTION

WAVELENGTH 0.0005876 E.F.L. 1143.0 FIELD 1.70

LIM. FREQ. 1133.43 CYCLES/MM NORMALIZING FACTOR 3.532

TANGENTIAL SCAN

NO.	Z	I	DE
-100	-0.01103	0.0174	0.0060
-95	-0.01048	0.0168	0.0066
-90	-0.00993	0.0197	0.0065
-85	-0.00937	0.0181	0.0065
-80	-0.00882	0.0194	0.0073
-75	-0.00827	0.0214	0.0074
-70	-0.00772	0.0203	0.0070
-65	-0.00717	0.0198	0.0085
-60	-0.00662	0.0296	0.0095
-55	-0.00607	0.0225	0.0108
-50	-0.00551	0.0408	0.0122
-45	-0.00496	0.0255	0.0135
-40	-0.00441	0.0542	0.0168
-35	-0.00386	0.0377	0.0192
-30	-0.00331	0.0737	0.0238
-25	-0.00275	0.0624	0.0328
-20	-0.00221	0.1190	0.0372
-15	-0.00165	0.1039	0.0573
-10	-0.00110	0.2030	0.0630
-5	-0.00055	0.1876	0.1136
0	0.0	0.4233	0.1136
5	0.00055	0.1876	0.0630
10	0.00110	0.2030	0.0573
15	0.00165	0.1039	0.0372
20	0.00221	0.1190	0.0328
25	0.00275	0.0624	0.0238
30	0.00331	0.0737	0.0192
35	0.00386	0.0377	0.0168
40	0.00441	0.0542	0.0135
45	0.00496	0.0255	0.0122
50	0.00551	0.0408	0.0108
55	0.00607	0.0225	0.0095
60	0.00662	0.0296	0.0085
65	0.00717	0.0198	0.0070
70	0.00772	0.0203	0.0074
75	0.00827	0.0214	0.0073
80	0.00882	0.0194	0.0066
85	0.00937	0.0181	0.0066
90	0.00993	0.0197	0.0065
95	0.01048	0.0168	0.0060
100	0.01103	0.0174	0.0059

FIRST MOMENT OF ENERGY -0.0002 ENERGY SUM 0.9374

SYSID

AUL ALL SPHERICAL RADIAL SCAN 10:48:50 07/09/74
CYCLE 46

INE SPREAD FUNCTION

AVELENGTH 0.0005876 E.F.L. 1143.0 FIELD 1.70

LIM. FREQ. 1131.43 CYCLES/MM NORMALIZING FACTOR 3.532

ADIAL SCAN

NO.	Y	I	DE
-100	-0.01105	0.0148	0.0050
-95	-0.01050	0.0121	0.0044
-90	-0.00994	0.0159	0.0056
-85	-0.00939	0.0141	0.0050
-80	-0.00884	0.0160	0.0060
-75	-0.00829	0.0159	0.0051
-70	-0.00773	0.0139	0.0049
-65	-0.00718	0.0139	0.0058
-60	-0.00663	0.0204	0.0076
-55	-0.00608	0.0194	0.0067
-50	-0.00552	0.0221	0.0084
-45	-0.00497	0.0228	0.0097
-40	-0.00442	0.0367	0.0141
-35	-0.00387	0.0375	0.0146
-30	-0.00331	0.0519	0.020
-25	-0.00276	0.0598	0.0252
-20	-0.00221	0.0940	0.0339
-15	-0.00166	0.0960	0.0571
-10	-0.00110	0.2569	0.1061
-5	-0.00055	0.2801	0.0869
0	0.0	0.2533	0.0956
5	0.00055	0.2442	0.0700
10	0.00110	0.1902	0.0743
15	0.00166	0.1936	0.0492
20	0.00221	0.1111	0.0432
25	0.00276	0.1148	0.0277
30	0.00331	0.0566	0.0221
35	0.00387	0.0605	0.0158
40	0.00442	0.0365	0.0133
45	0.00497	0.0337	0.0101
50	0.00552	0.0278	0.0098
55	0.00608	0.0258	0.0098
60	0.00663	0.0292	0.0090
65	0.00718	0.0232	0.0096
70	0.00773	0.0276	0.0073
75	0.00829	0.0172	0.0077
80	0.00884	0.0247	0.0078
85	0.00939	0.0193	0.0065
90	0.00994	0.0185	0.0077
95	0.01050	0.0234	0.0064
100	0.01105	0.0137	0.0064

FIRST MOMENT OF ENERGY 0.0002 ENERGY SUM 0.9432

.SNS1)

UL ALL SPHERICAL RADIAL SCAN 10:48:50 07/09/74
CYCLE 40

NE SPREAD FUNCTION

AVELENGTH 0.0005876 E.F.L. 1143.0 FIELD 2.50

L M. FREQ. 1127.78 CYCLES/MM NORMALIZING FACTOR 3.532

DIAL SCAN

NO.	Y	I	OE
100	-0.01106	0.0141	0.0064
-95	-0.01053	0.0220	0.0071
-90	-0.00998	0.0172	0.0058
-85	-0.00942	0.0214	0.0070
-80	-0.00887	0.0193	0.0078
-75	-0.00831	0.0224	0.0070
-70	-0.00775	0.0208	0.0099
-65	-0.00720	0.0317	0.0095
-60	-0.00665	0.0249	0.0112
-55	-0.00610	0.0365	0.0125
-50	-0.00554	0.0383	0.0176
-45	-0.00499	0.0560	0.0160
-40	-0.00443	0.0525	0.0242
-35	-0.00388	0.0762	0.0249
-30	-0.00333	0.0780	0.0398
-25	-0.00277	0.1303	0.0383
-20	-0.00222	0.0910	0.0579
-15	-0.00166	0.2426	0.0835
-10	-0.00111	0.1490	0.0738
-5	-0.00055	0.2460	0.0854
0	0.0	0.2009	0.0526
5	0.00055	0.1642	0.0655
10	0.00111	0.1557	0.0412
15	0.00166	0.0956	0.0340
20	0.00222	0.0562	0.0231
25	0.00277	0.0514	0.0158
30	0.00333	0.0547	0.0171
35	0.00388	0.0393	0.0120
40	0.00443	0.0333	0.0125
45	0.00499	0.0336	0.0103
50	0.00554	0.0287	0.0110
55	0.00610	0.0290	0.0082
60	0.00665	0.0217	0.0097
65	0.00720	0.0301	0.0091
70	0.00775	0.0215	0.0080
75	0.00831	0.0244	0.0088
80	0.00887	0.0250	0.0083
85	0.00942	0.0215	0.0077
90	0.00998	0.0238	0.0082
95	0.01053	0.0203	0.0069
100	0.01106	0.0210	0.0075

FIRST MOMENT OF ENERGY -0.0005 ENERGY SUM 0.9308

SVSD

RAUL ALL SPHERICAL TANGENTIAL SCAN 10:48:50 07/09/74
YCLE 46

INE SPREAD FUNCTION

AVELENGTH 0.0005876 E.F.L. 1143.0 FIELD 2.50

IM. FREQ. 1132.17 CYCLES/MM NORMALIZING FACTOR 3.532

TANGENTIAL SCAN

NO.	Z	I	DE
-100	-0.01104	0.0198	0.0072
-95	-0.01049	0.0210	0.0078
-90	-0.00994	0.0224	0.0075
-85	-0.00938	0.0209	0.0083
-80	-0.00883	0.0250	0.0065
-75	-0.00828	0.0234	0.0091
-70	-0.00773	0.0273	0.0090
-65	-0.00718	0.0239	0.0102
-60	-0.00662	0.0336	0.0107
-55	-0.00607	0.0270	0.0131
-50	-0.00552	0.0471	0.0138
-45	-0.00497	0.0315	0.0169
-40	-0.00442	0.0540	0.0186
-35	-0.00386	0.0404	0.0203
-30	-0.00331	0.0747	0.0227
-25	-0.00276	0.0562	0.0276
-20	-0.00221	0.0945	0.0294
-15	-0.00166	0.0657	0.0446
-10	-0.00110	0.1489	0.0521
-5	-0.00055	0.1954	0.1230
0	0.0	0.4561	0.1230
5	0.00055	0.1954	0.0521
10	0.00110	0.1489	0.0446
15	0.00166	0.0657	0.0294
20	0.00221	0.0945	0.0276
25	0.00276	0.0562	0.0227
30	0.00331	0.0747	0.0203
35	0.00386	0.0404	0.0186
40	0.00442	0.0540	0.0169
45	0.00497	0.0315	0.0138
50	0.00552	0.0471	0.0131
55	0.00607	0.0270	0.0107
60	0.00662	0.0336	0.0102
65	0.00718	0.0239	0.0090
70	0.00773	0.0273	0.0091
75	0.00828	0.0234	0.0085
80	0.00883	0.0250	0.0063
85	0.00938	0.0209	0.0075
90	0.00994	0.0224	0.0078
95	0.01049	0.0210	0.0072
100	0.01104	0.0198	0.0069

FIRST MOMENT OF ENERGY -0.0001 ENERGY SUM 0.9278

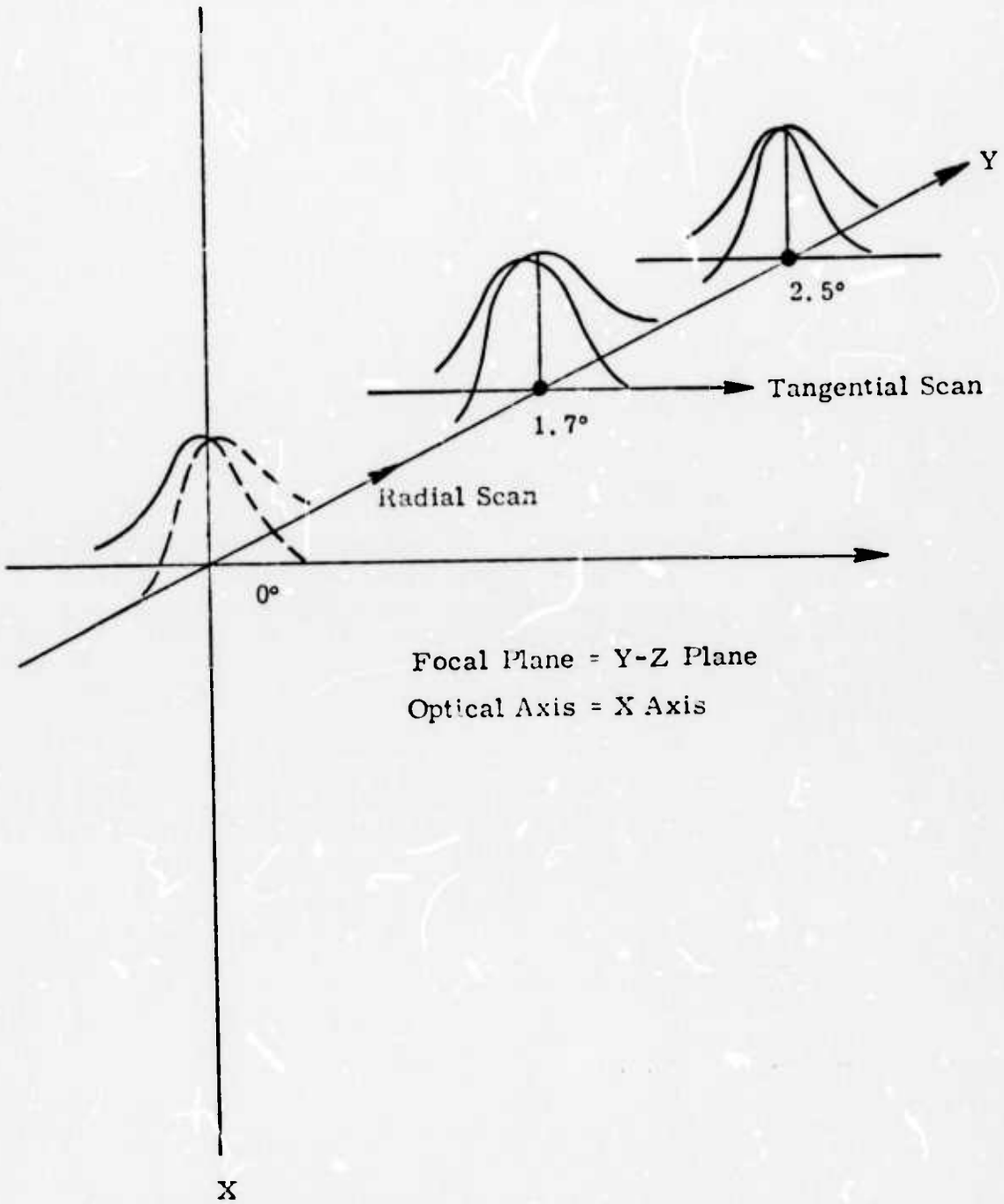

Figure 23. Definition of Line Spread Function Axes

4.3.4 Conclusions

Both forms discussed above have the potential of meeting the requirements of the TEAL-AMBER I study. None of the designs have been fine-tuned nor have tolerance studies been undertaken. Therefore, the MTF responses are probably quite close to the hardware values.

A figure of merit for performance is MTF times optical efficiency times one minus the area obscuration. As shown in Table 6 all the figures of merit are very close. Therfore, ease of manufacture can become a larger decision making factor. The all spherical system will be easier to fabricate and obtain the necessary blanks since unusual glasses are not used.

The sensitivities of the aspheric system to melt variation in the corrector glasses is higher than the all-spherical one. These variations in the optical properties can be compensated for by making final adjustments at the assembly phase of the telescope. Such changes include changing the spacing of the optical elements relative to each other and also retouching the aspheric surfaces on one of the corrector elements in order to minimize the residual chromatic variation. Obviously, this adds to the complexity of fabrication. Based on these results, the systems represented by C&D are the recommended systems, strictly because all surfaces are spherical, the refractors are common glass and the system will be easier to manufacture.

However, there are additional options to be exercised in both subforms with a possible increase in total system performance. The position of the focal plane keeps the total response of systems A & B away from the optimum. If the total camera could be inserted into the whole of the primary a fair distance, the MTF response would improve. Basically, the primary will become less powerful, thus, easing the aberration problem. Or the total system could be increased in aperture size, (keeping fast f/#) thus increasing the photon collection efficiency of the system. There is a positive trade that should be carried out of f/#, focal plane position, and photon flux density at the photocathode surface for systems A & B. One will note that in system D. the focal surface is very near the vertex of the reflecting surface of the

TABLE 6. TELESCOPE TRADEOFFS

Monochromatic MTF at 10 cycles/mm Field Angle MTF	System A	B	C	D
0° Radial or Tangential	0.77	0.87	0.91	0.95
1.7° Radial	0.77	0.85	0.92	0.90
1.7° Tangential	0.77	0.80	0.91	0.83
2.5° Radial	0.77	0.82	0.89	0.83
2.5° Tangential	0.77	0.56	0.80	0.75
Optical Efficiency at 0.5μ	0.9	0.9	0.8	0.8
Area Obscuration	0.30		0.36	
Chromatic Aberration	Needs three Correctors		Done by Spherical Elements	
Simplicity	Aspherics		All Spheres	
FM: 0°	0.49	0.55	0.47	0.49
1.7° R/T	0.49/0.49	0.54/0.51	0.47/0.47	0.46/0.43
2.5° R/T	0.49/0.49	0.52/0.35	0.45/0.41	0.43/0.38

primary mangin mirror. Systems C&D could possibily be improved by not using the Mangin Mirror, but a first surface mirror with the requirement for a high field curvature correction transferred to the field group.

Based on the above study, the recommended specifications for the TEAL-AMBER I telescope have been established. (Refer to table 7.)

TABLE 7. TEAL-AMBER TELESCOPE, RECOMMENDED SPECIFICATIONS

Form	Cassegrain
Clear Aperture	30" diam.*
f/#	f/1.5
Total Optical Efficiency	> 0.5
MTF at 10 cycles/mm Over Total Field in Both. Radial and Tangential Directions	> 0.75
Blur Circle 80% of energy	< 6 sec or 33μ
Spectral Region	0.4 to 0.6μ weighted for the solar and S-20 responses
FOV	5° x 1°*
Focal Surface	Flat 6" behind the last optical element* and near vertex of primary mirror.
Distortion	Cause less than 8 sec due to mapping of a spherical heaven onto a flat focal surface. (See Section 4.4.)
Off-Axis Rejection	Reduce the moon at 10° off the FOV to 0.1 of the in-field scattered energy - BRDF (at 10° or greater) of < 2×10^{-3} (See Section 4.5.)

*Required by camera

4.4 MAPPING PROBLEM OF THE TEAL AMBER-I CAMERA

In the TEAL-AMBER I camera, it is desirable to transform the angle space of the heavens onto a flat surface at the photocathode of the imaging tube. This is necessary because of the resolution requirements on the electron optics, which transforms photon image at the photocathode into an electron image at the storage device. Ordinarily, this would not cause a severe problem but would

create a mapping function of $f(\theta) = A(\theta + k\theta 3)$ with the associated distortion. However, for the TEAL-AMBER I camera, the star's image will move across the telescope focal surface during any one exposure or as the telescope is scanned across the heavens. Thus, the star will move along a nonlinear path on the flat surface. The concept is to track this star with the image-storing device, a tape that will store electrons with spatial distribution. However, the tape has only one degree of freedom and it must be used to correct for the major scan motion. Also, the motion can only be a constant linear movement. The result of the nonlinear star's image motion and the linear one-directional tape motion is an effective motion of the star on the tape. This motion could be detrimental in the form of creating false alarms by making star tracks that could be interpreted as satellites and by reducing the photon density of the satellite image on the tape. Therefore, it is highly desirable to minimize or eliminate this motion. This section discusses the magnitude of the problem.

4.4.1 Conclusions

The conclusion reached in this study is that stars will create tracks on the storage tape on the order of 10 to 12 arc-sec. This is for an isotropic imaging telescope in which the available parameters have been optimized and the instantaneous FOV is 5° x 10°. Also, the scanned angular space is not mapped onto the tape in a linear fashion and the transform is not achieved by multiplying the angle by the telescope focal length.

4.4.2 Small Angle Approximation of a Spherical Image Surface

Figure 24 shows two stars in angle space, one at $\emptyset = \emptyset_o$, $\theta = 0$ and one at $\emptyset = \emptyset_o$, $\theta = \theta_o$, where θ is a line of latitude and $\emptyset$ is a line of longitude within the telescope's FOV. The references for the angles are the telescope optical axis (y) and scan axis (x). The telescope will scan at a rate of $\emptyset$ about the x-axis; thus, the star will move, referenced to telescope optical axis, at the $\emptyset$ rate as shown by the arrows. If angle space is imaged onto a concave spherical surface, this diagram also suffices for the image surface. Now, if one would rotate the image sphere at $\emptyset$ also, the star's image would not move on the image surface. This is the

MAPPING OF SPHERICAL SURFACE ON TO A FLAT SURFACE

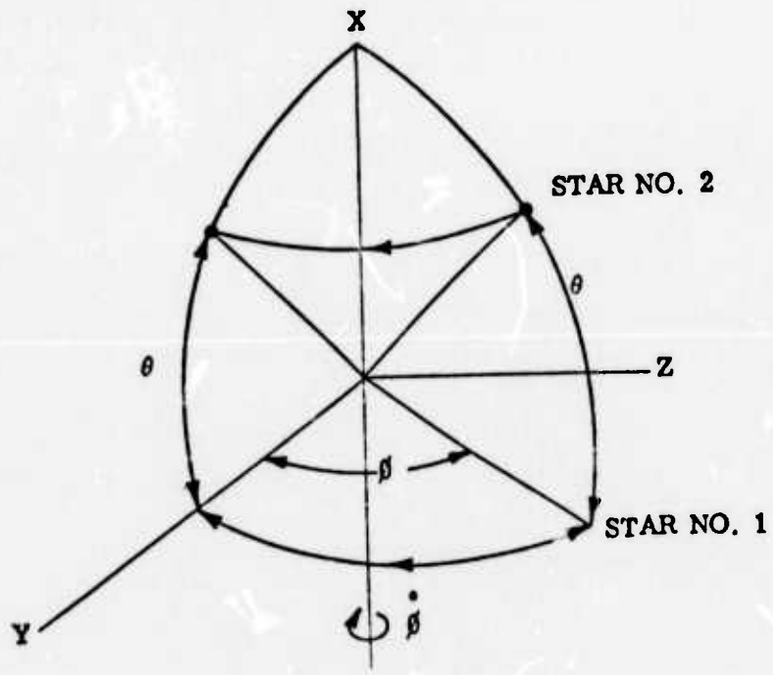

- SMALL ANGLE APPROXIMATION

$$X = f\theta, \quad Z = f\phi, \quad \dot{Z} = f\dot{\phi}$$

- IF $\vec{V}_{TAPE} = \dot{Z}$, STAR'S IMAGE WILL NOT MOVE ON TAPE

Figure 24. Coordinate Definitions

basic scanning philosophy of the TEAL-AMBER I camera. The same result would also be approximately true if the initial angles (ϕ_o, θ_o) were small and the image surface were flat. However, for the TEAL-AMBER I camera, ϕ_o and θ_o are in the 2° to 5° range and residual motions on the order of 8 arc-sec are of concern. Under these conditions, the small angle approximation is not valid.

4.4.3 Mapping of a Spherical Surface onto a Flat Surface in a Real Optical System

Figure 25 shows the two stars from angle space mapped onto a flat surface with the third order distortion coefficient K added to the linear or small angle approximation. In this figure, K is symmetrical about the optical axis (y), and X_1 is not equal to X_2, nor is Z_1 equal to Z_2. Again as the telescope is rotated, star #2 moves towards (X_1,0) and star #1 moves towards (0,0), both at a nonlinear rate in the Z direction since $Z = f\ (1 + 3K\ \theta^2)\ \dot{\phi}$ (f is the focal length). The actual motions are calculable. This is shown in Figure 26. It should be noted that there exist higher order distortion coefficients, but they modify angles raised to the 5th power and thus can be neglected for this problem of 2° to 5°: ($5° \Longrightarrow 0.436$ RAD, $(0.436)^3 = 0.08$ and $(0.436)^5 = 0.016$).

For the case of a distortionless system ($K = 1/3\ \theta \rightarrow f\tan\theta$ and $\dot{Z} = f\dot{\phi}$), there are motions on the order of 36 arc-sec. This is shown in Figure 27 where the ideal positions of the star on the tape as shown as "o" and the actual as "X". Each vertical line is the same line on the tape just displaced in time. The bottom section of the figure shows the total motion of the star's image on the tape for $\phi_o = 5°$, $\theta_o = 2.5°$ or a 5° x 10° telescope FOV.

Looking at the equations in Figure 26, there are two parameters that can be varied: K&L. In the optical design, K can be varied by changing the classical distortion requirements of the primary optics or by introducting some other mechanism such as fiber optics. L is just a gain value in the tape servo control. Therefore, the question is: if one had complete freedom to select K and L, what would be an optimum selection? It should be noted at

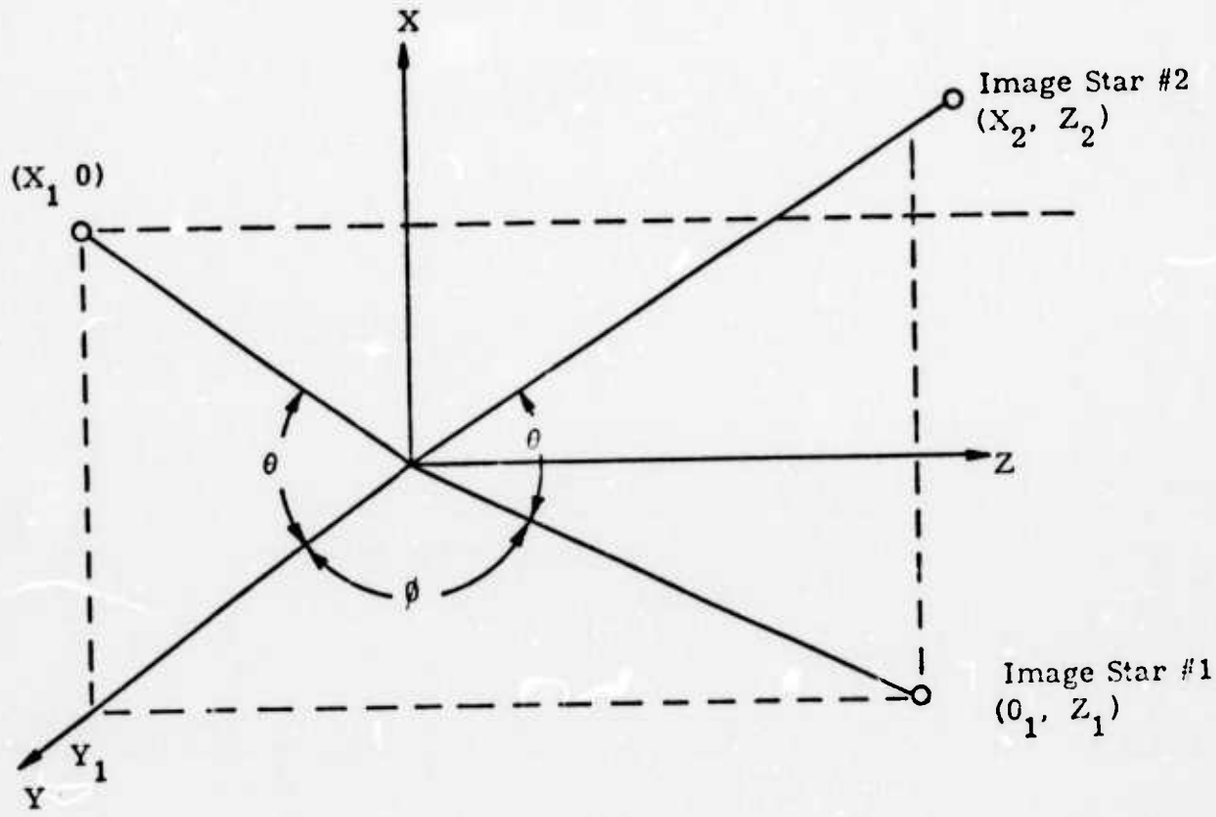

Focal Plane at Y = f (Focal Length)

$$X = f(\theta + K\theta^3)$$

$$Z = f(\phi + K\phi^3)$$

Figure 25. Mapping of Spherical Surface Onto a Flat Surface

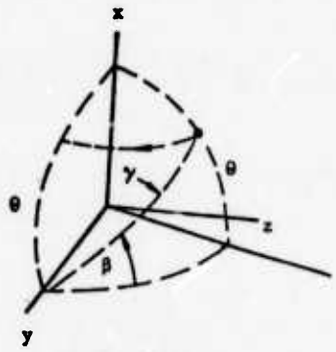

Angle Space

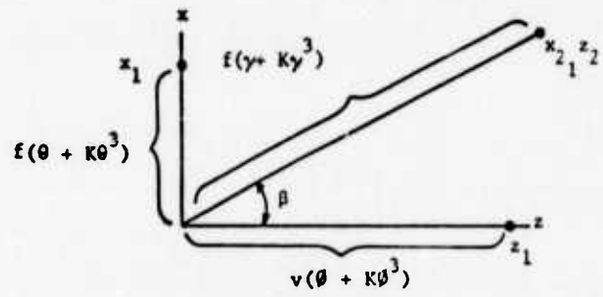

Image Space

(1) From spherical trigonometry of a right spherical triangle:

$$\cos\gamma = \cos\theta\cos\phi$$
$$\cos\beta = \tan\phi/\tan\gamma$$
$$\sin\beta = \sin\theta/\sin\gamma$$

(2) In image space:

$$X_2 = f(\gamma + K\gamma^3)\sin\beta$$
$$Z_2 = f(\gamma + K\gamma^3)\cos\beta$$
$$X_1 = f(\theta + K\theta^3)$$
$$Z_1 = f(\phi + k\phi^3)$$

(3) The total peak excursion in the X direction is

$$X_2 - X_1 = f(\gamma + K\gamma^3)\sin\beta - f(\theta + K\theta^3)$$

(4) The instantaneous variation of the actual Z value from the desired value (Z tape) is

$$Z_{actual} - Z_{tape} = (\gamma + K\gamma^3)\cos\beta - L\phi f$$

where L relates $\dot{\phi}$ to $\dot{Z}$, $\dot{Z} = L\phi f$

(5) Using the first two terms of the power series expansions for the trigonometric functions

$$\sin\beta = (\theta - \theta^3/6)/\gamma - \gamma^3/6)$$
$$\cos\beta = (\phi + \theta^3/3)/\gamma + \gamma^3/3)$$
$$\gamma^2 = \phi^2 + \theta^2$$

(6) Substituting the approximations and neglecting high order terms

$$X_2 - X_1 \approx (K + 1/6)\,\phi^2\,\theta$$
$$Z_{act} - Z_{tape} \approx f((1-L) + (K - 1/3)\,\theta^2 + K\phi^2)\,\phi = \Delta Z$$

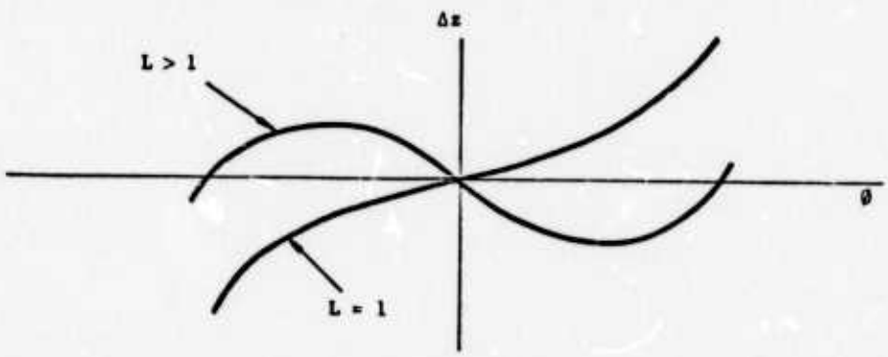

Typical Δz for K = 1/3, θ = 0

Figure 26. Derivation of Star's Motion (Cont.)

this point that K could be theoretically made direction sensitive where $K_x \neq K_z$. The following optimization keeps K constant and independent of direction. The basic question is: what is an optimum system? The simplest assumption is to select that operating point where the maximum star motion at any point in the FOV is minimized. This may result in motions at some points within the FOV that are larger than the minimum motion that could be achieved by optimizing K&L for that specific point. Figures 28 through 34 show the maximum peak to peak excursions of ΔX and ΔZ as a function of K for various L values. For example, based on the above rule, the optimum K value for L = 1.001 would be 0.15. Under these conditions, a star will have total motions in accordance with the table below:

θ	ΔZ	ΔX
0	13 arc-sec	0 arc-sec
2.0°	17 arc-sec	16 arc-sec
2.5°	20 arc-sec	20 arc-sec

Table 8 is a summary chart of the maximum excursions of the star's image on the tape. Based on this chart, the optimum is within L = 0.9995, K = 0.018 to L = 0.9997, K = 0.005 with worst case excursions of 10 to 12 arc-sec.

An interesting point is that L is not equal to 1 for the optimum, implying that the tape is moving at a slower velocity than the scan. However, this is true only at $\theta = 0$. Effectively, the tape rate has been matched to the average velocity at another point within the FOV (θ_1) where Z (actual)=Z (tape) at the ends of the FOV or $\emptyset = \emptyset_o$ (see Figure 35).

4.4.4 Mapping of a Total Scan

The fact that L is not equal to one implies a distoriton in the overall scanned FOV. This is effectively a gain function in the scanned direction (Z). The basic question is: what will a typical mapping of ϕ, α

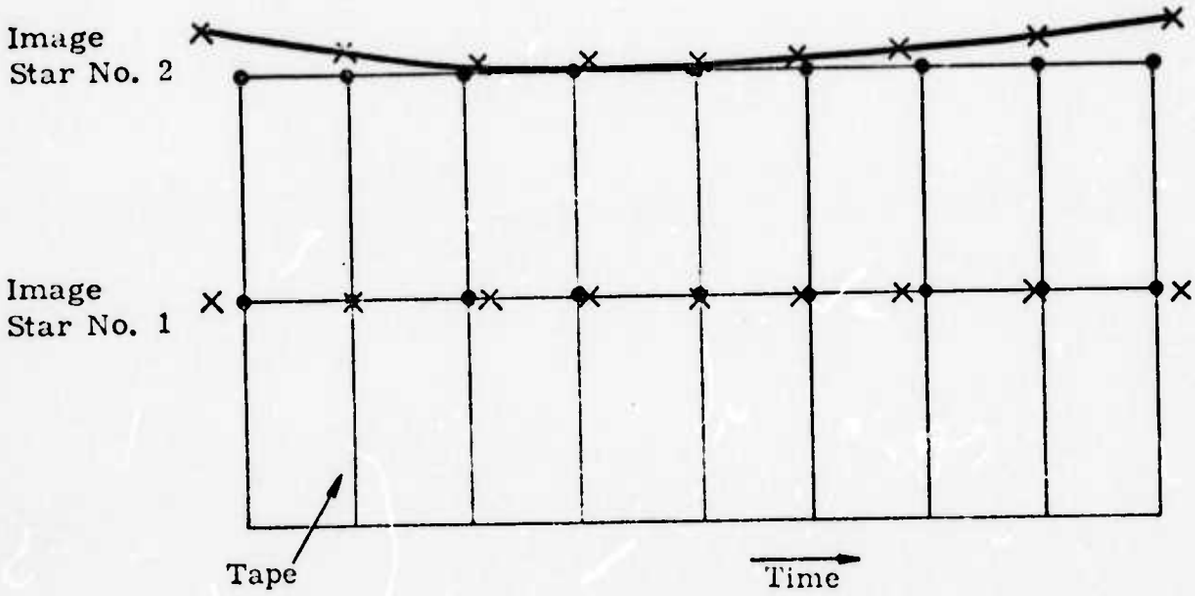

	Star Motions on Tape For L = 1, $\dot{Z} = f\dot{\phi}$
Star No. 2	≈ 34 Arc-Seconds ≈ 36 Arc-Seconds
Star No. 1	0 Arc-Seconds ≈ 36 Arc-Seconds

Figure 27. Motion of Star for "Distortionless System"

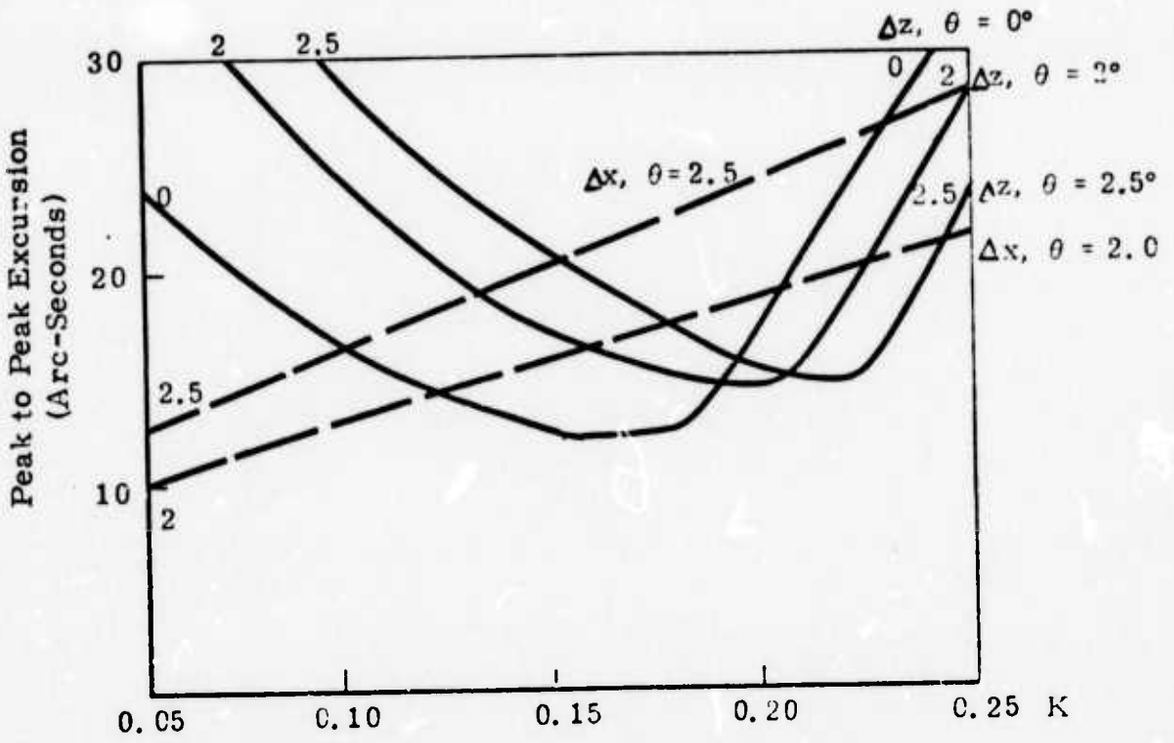

Figure 28. Δz, Δx vs. K for L = 1.001

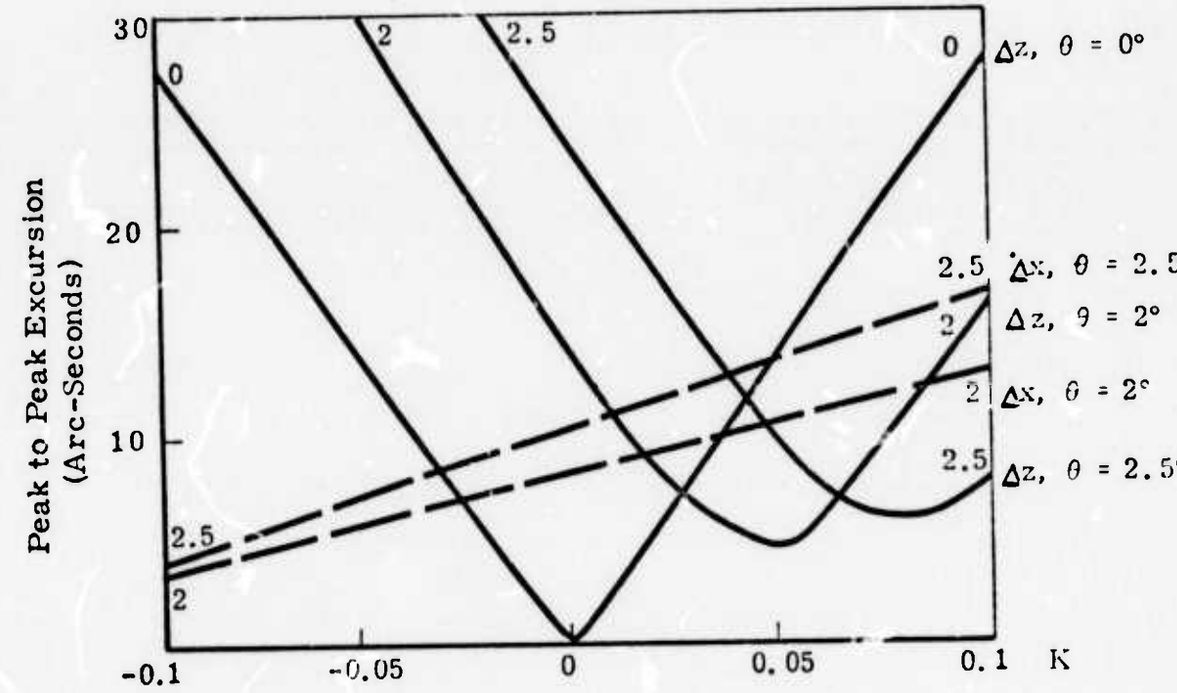

Figure 29. Δz, Δx vs. K for L = 1.000

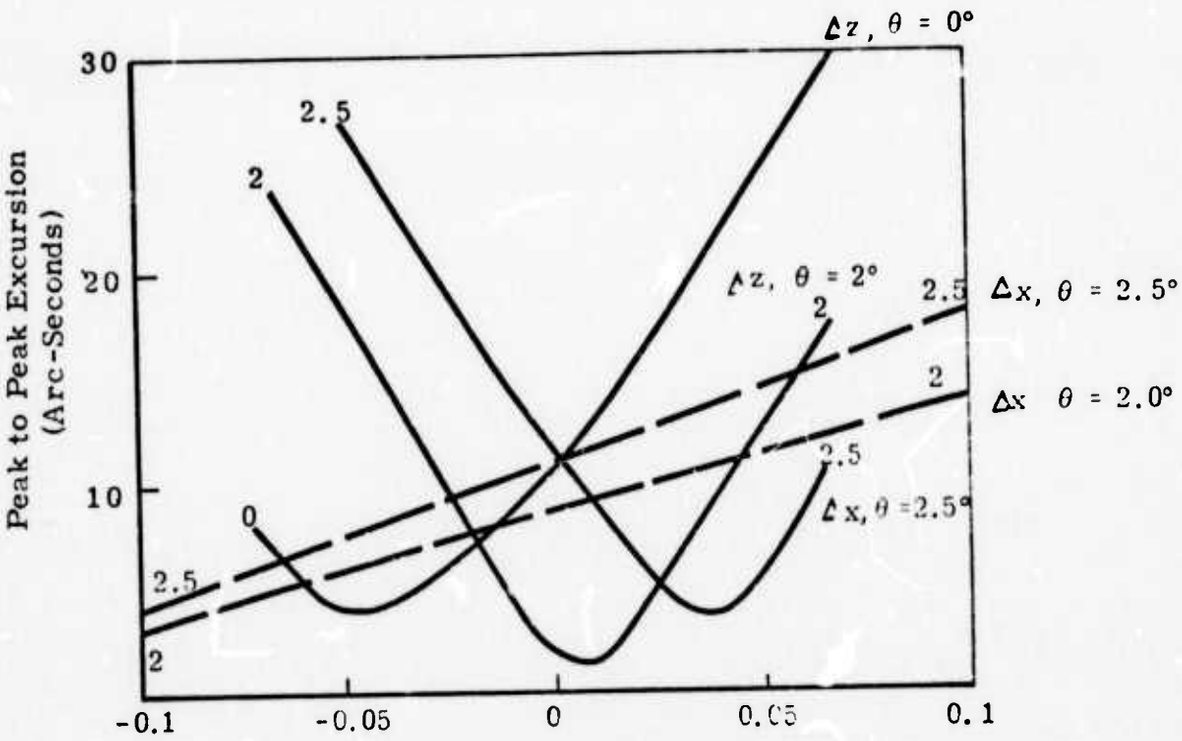

Figure 30. Δz, Δx vs. K for L = 0.9997

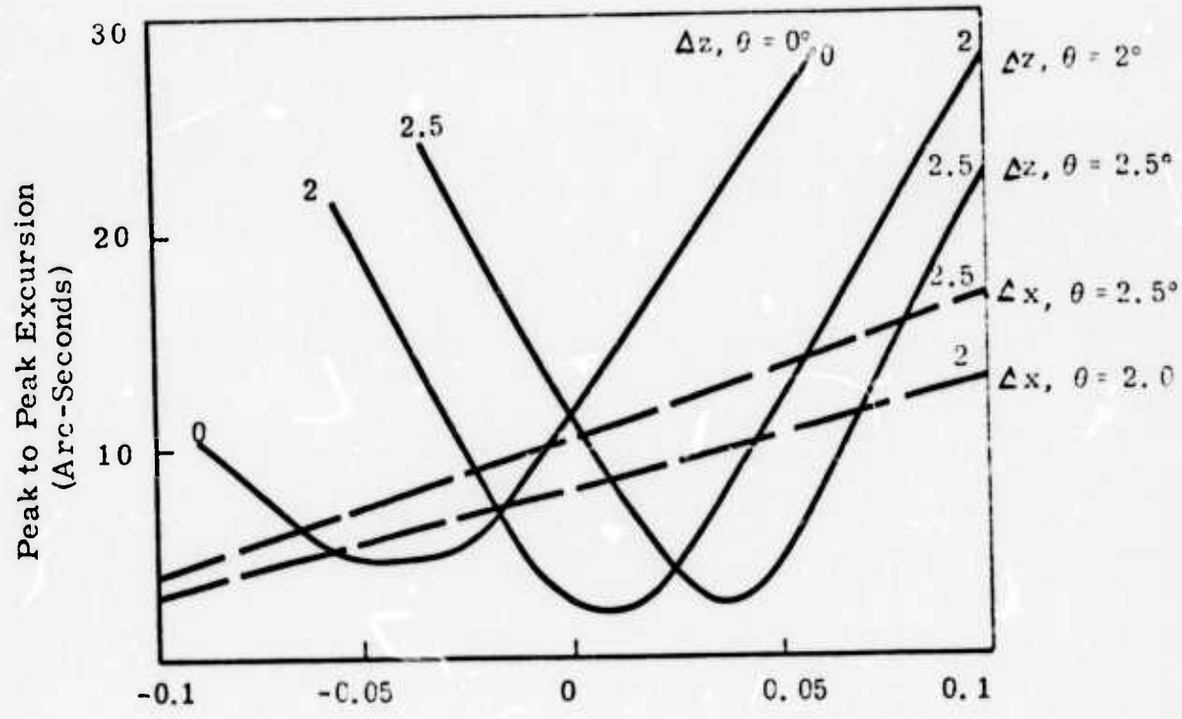

Figure 31. Δz, Δx vs. K for L = 0.9968

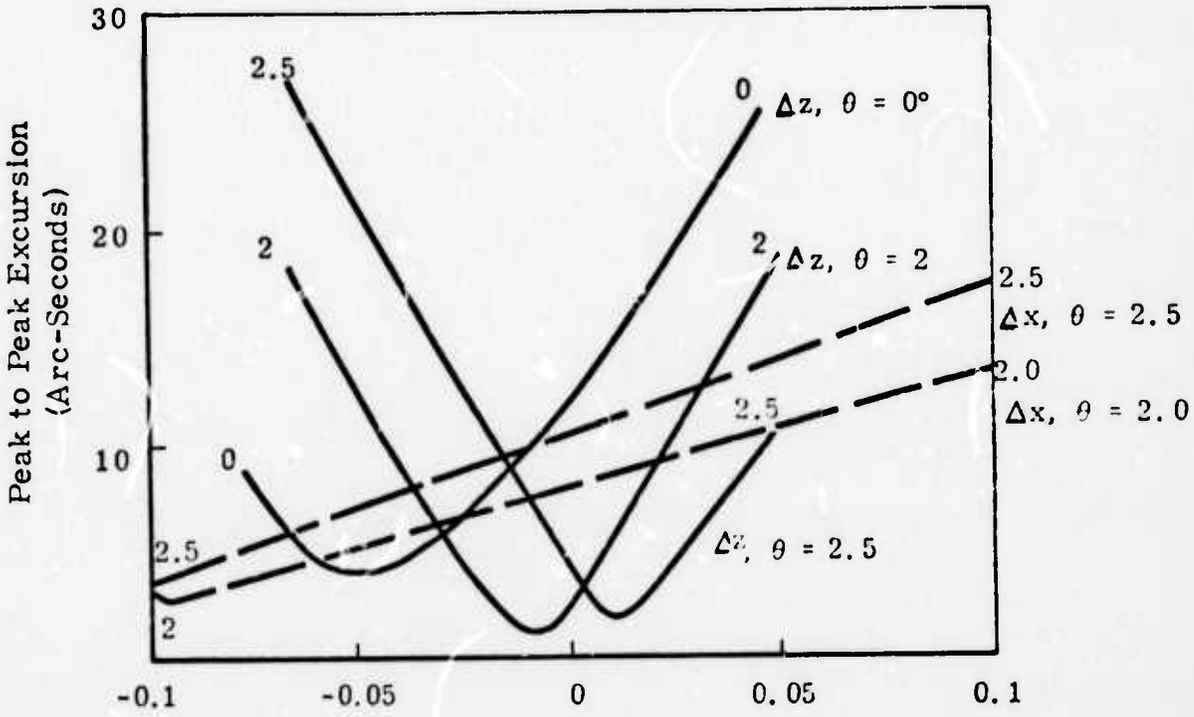

Figure 32. Δz, Δx vs. K for L = 0.9995

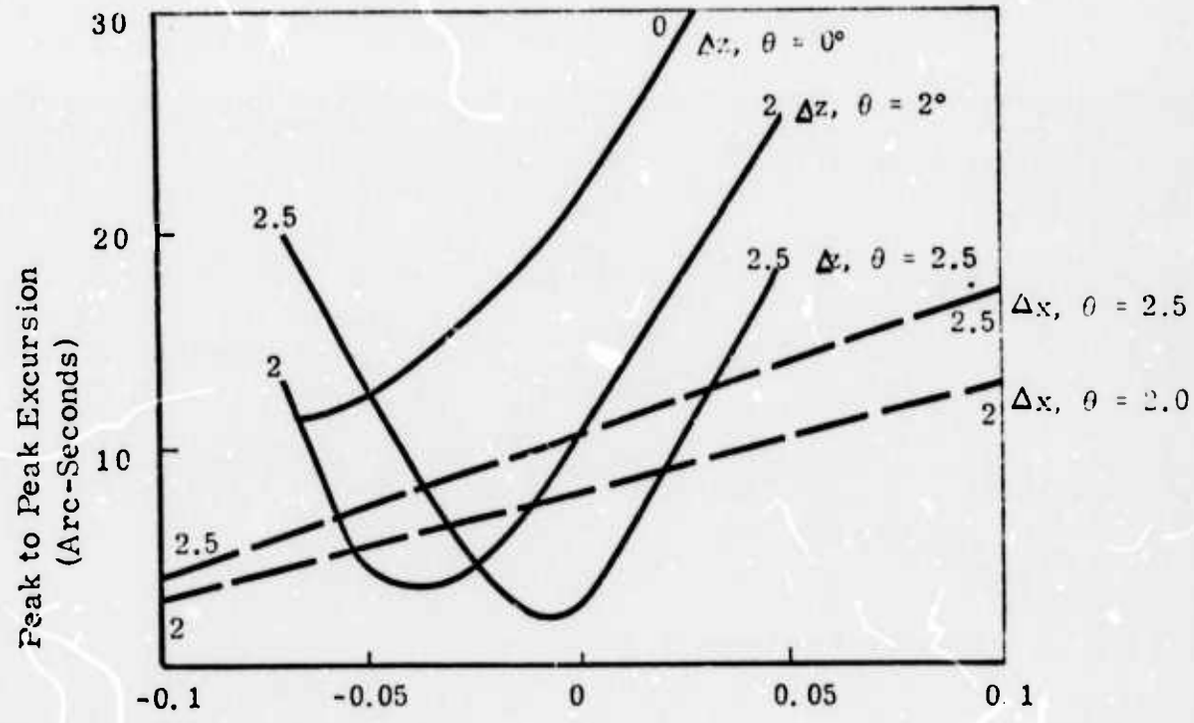

Figure 33. Δz, Δx vs. K for L = 0.9993

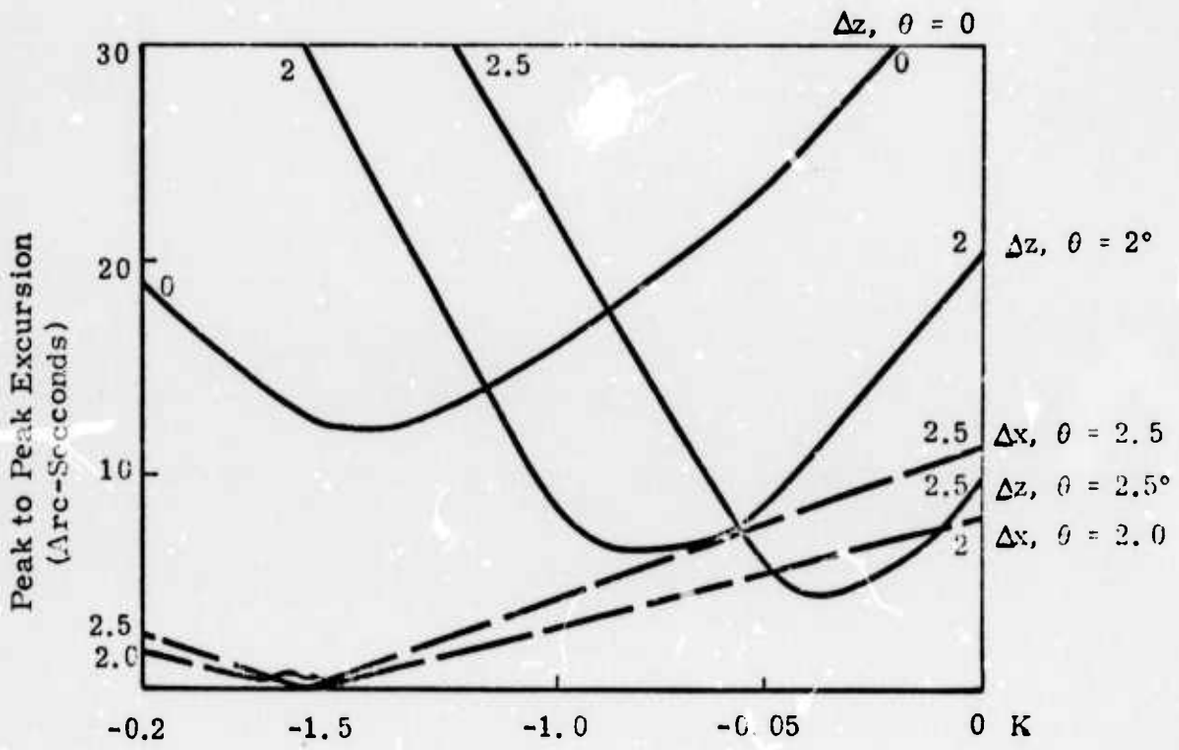

Figure 34. Δz, Δx vs. K for L = 0.9990

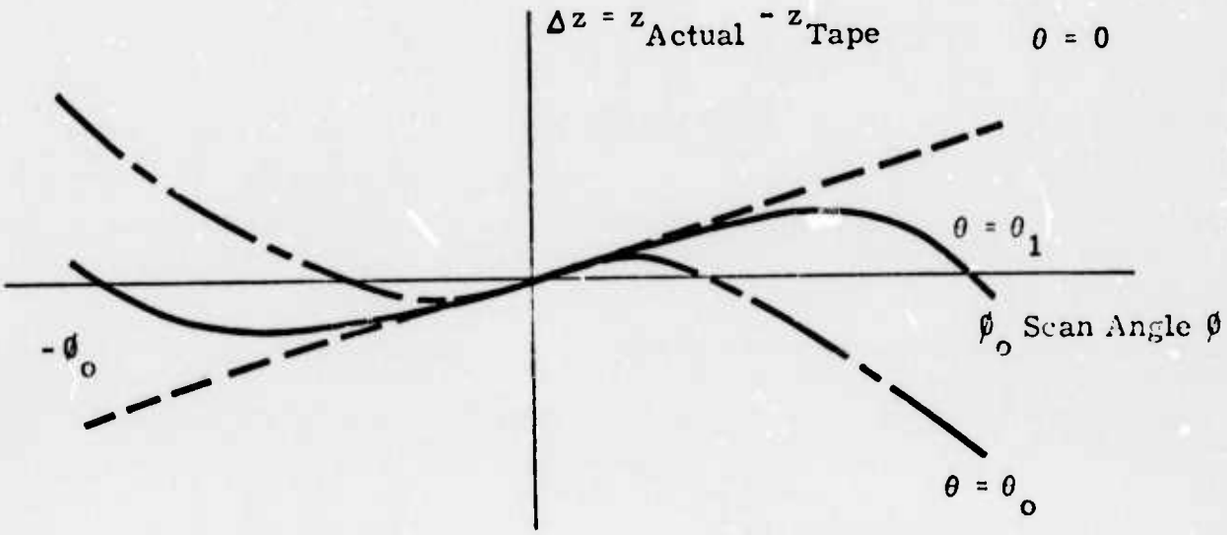

It can be shown that

$$\theta_1^2 = \left[1 - L + K\phi_o^2\right] / (K - 1/3)$$

Figure 35. Typical Δz for Various θ (Latitude Lines)

TABLE 8. MAXIMUM MOTION OF STAR'S IMAGE VERSUS L&K&θ FOR $\phi_{MAX} = 5°$

		θ = 0°		2.0°		2.5°	
L	K	ΔX	ΔZ	ΔX	ΔZ	ΔX	ΔZ
1.001	0.15	0	13	16	17	20	20
1.000	0.03	0	8	10	64	13	13
0.9997	0.005	0	8	9	2	11	13
0.99968	0.0	0	12	9	2	11	11
0.9995	-0.018	0	13	8	2	10	11
0.0003	-0.045	0	14	6	4	8	13
0.999	-0.08	0	17	4	7	6	17

ΔX, ΔZ are in arc-sec

onto Z, X look like on the tape? ψ and α are the angular coordinates of the total scan (see figure below).

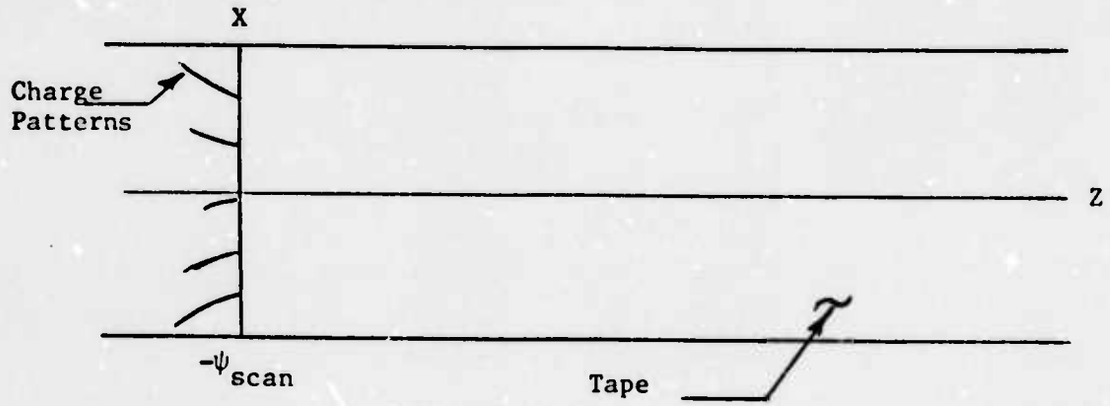

To answer the above question, one must define the star's point position within an exposure. The stars create tracks, not point images, during an exposure. Also, the beginning of the scan on the tape must be identified and defined. The most obvious point on the tape for the star's position is when the star has been within the telescope's FOV for one half an exposure. As shown in Figures 26 and 35, the motion of the star's image is symmetrical about this time point. For the beginning of scan, a practical reference is when the optical axis (center of the telescope FOV) is coincident with the starting scan angle of the total scan pattern ($-\psi$ scan) (See Figure 36.)

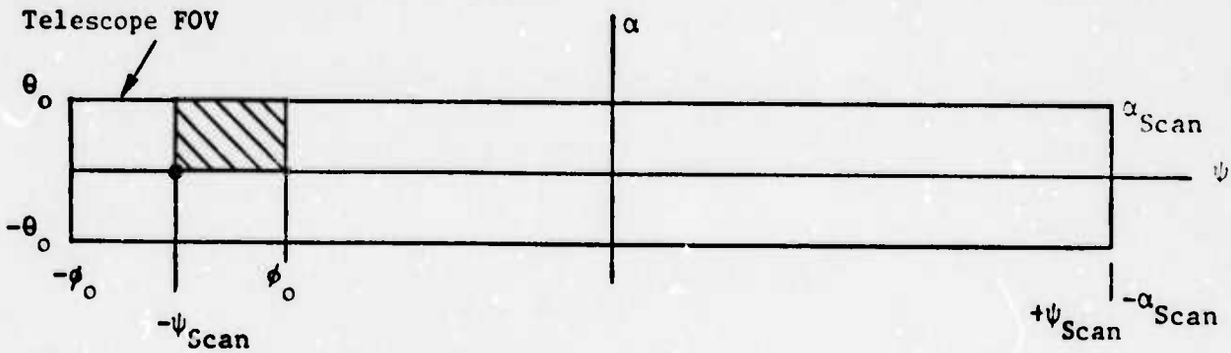

where ψ is scan angle referenced to celestial sphere
α is a latitude line of the scanned FOV.

Figure 36. Telescope FOV as Related to the Total Scanned FOV

At the beginning of the scan $(t = 0)_1$, a linear array of stars in α at $\psi = -\psi$ scan would have been within the telescope's FOV for one-half

of the total exposure. Thus, the actual scanning process would have started at $t = t_{exposure/2}$, and a charge pattern would have already been deposited on the tape (See figure above).

At this point $\alpha = \theta$ and $X = \alpha + K\alpha^3$; thus, α is not mapped linearly into X. Similarly, and α-array of stars at $\psi = \psi_o$ would have the same charge pattern on the tape at $t = t_o = \frac{-\psi_o + \psi \text{ scan}}{\dot{\phi}}$

The pattern will be displaced on the tape by the dimension Z_o, where

$$Z_o = L\dot{\phi}\, t_o = Lf\,(-\psi_o + \psi_{scan})$$

Therefore, the mapping of angle space onto the tape is defined by:

$$X = f(\alpha + K\alpha^3)$$

$$Z = Lf(-\psi + \psi_{scan})$$

4.5 OFF-AXIS REJECTION (BAFFLING)

In order to size the telescope, the gimbal, and the dome in which it will be housed, it is necessary to establish the length of fore-baffle required to obtain the performance of the system in the presence of off-axis sources of photons. It is the purpose of this section to make certain assumptions about the problem, using this input size for the fore-baffle. Basically, the results of this brief study are stated below:

a. The major source of off-axis energy is the moon.

b. The moon creates a large in-field source of diffuse energy, thus reducing the effect of out-of-field sources.

c. A fore-baffle equal in length to one-quarter the aperture diameter will reduce the moon's off-axis energy to less than 10% of the in-field energy. Thus, a long baffle is not required.

4.5.1 Off-Axis Rejection Requirements

The major consideration for determing the off-axis rejection criteria for the telescope is the increase in noise created by this source of photons. The general effect of energy sources outside the FOV is to increase the photon flux at the image plane somewhat uniformly over the total photocathode area. Thus, this increases the number of photons per sample and the inherent photon noise level. The distribution of this added energy will not be completely uniform but will have very low spatial frequencies (fractions of a cycle/mm). The major source of extra energy is the moon. Its energy can be scattered off the optical surfaces onto the photocathode. However, the moon's energy is also scattered by the atmosphere and creates a background level within the FOV of the telescope. Therefore, the off-axis energy is added to the on-axis atmospheric scatter energy making the off-axis rejection requirements less severe since the former cannot be avoided. The criterion selected for the off-axis rejection requirement is to reduce the off-axis photons to less than 10% of the in-field atmopsheric scattered photons.

4.5.2 Basic Definitions

Before proceeding with how the above requirement reflects itself in the telescope design, it is appropriate to establish some basic definitions. There are three basic parameters: BRDF, PSRR, ESRR. Also, the effect of a fore-baffle on a system should be established.

4.5.2.1 Bidirectional Reflectance Distribution Function (BRDF)

a. Mirror Surfaces

The scatter characteristics of mirror surfaces can be described by a bi-directional reflectance distribution function (BRDF), which describes the fraction of energy scattered in a given direction as a function of two angles: the angle of incidence on the surface (θ) and the angle (ϕ) between the direction in which the scattered light is measured and the direction in which the specularly reflected energy propagates.

The BRDF, as shown in Eq. 1 below, has the units of (fraction/steradian) and can be physically interpreted as the amount of energy $P(\theta, \phi)$ detected by a detector located at some angle ϕ with respect to the specularly

reflected component divided by the total incident radiation $P(\theta, o)$ and the solid angle subtended by the detector. Thus,

$$BRDF(\theta, \phi) = \frac{P(\theta, \phi)}{P(\theta, o)} \quad \frac{1}{\Omega_{DET}} \qquad \text{Fraction/Steradian} \qquad (1)$$

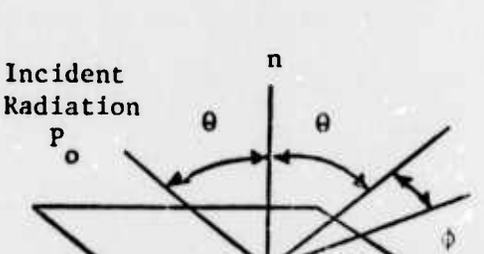

Specularly Reflected Radiation

Scattered Radiation P_ϕ
(Measured by Ω_{DET})

For the analysis contained in this report, the BRDF has been assumed to be a function of the angle ϕ only, which is effectively the angular distance between the detector and the source.

$$BRDF(\phi) = \frac{P(\phi)}{P(o)} \quad \frac{1}{\Omega_{DET}} \qquad [\text{Fraction/Steradian}] \qquad (2)$$

b. Refractor Surfaces

For a refractor, a similar set of equations can be derived.

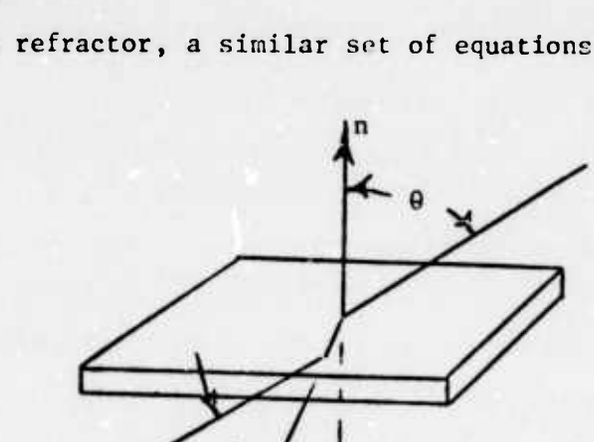

$$BRDF(\theta, \phi) \approx BRDF(\phi) = \frac{P(\phi)}{P(o)} \cdot \frac{1}{\Omega_{DET}} \qquad (3)$$

c. Optical System

Just as the scatter characteristics of a surface can be described by a BRDF, the scatter characteristics of an optical system can also be described by a BRDF whose meaning is analogous to that of a surface; i.e., the BRDF of a system describes the fraction/steradian of the incident energy being scattered onto a detector in the focal plane whose position in the focal plane is such that its angular displacement from the source of the collimated energy is the angle ϕ.

$$BRDF = \frac{P(\phi)}{P(o)} \cdot \frac{1}{\Omega_{DET}} = S(\phi) \tag{4}$$

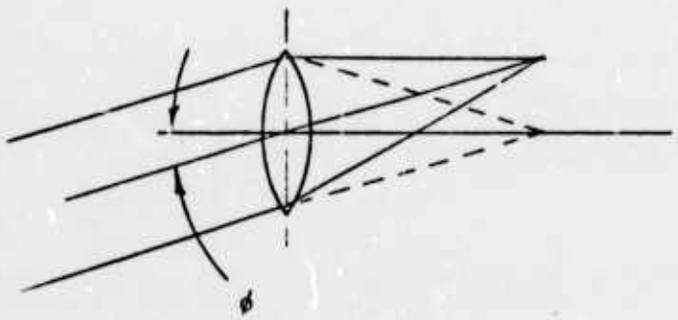

4.5.2.2 Point Source Rejection Ratio (PSRR)

For optical systems having the operational requirement that they be able to search a field of view close to a single bright point source, the system performance parameter of interest is the point source rejection ratio (PSRR), which describes the amount of energy from the unwanted point source detected when the system's line of sight is displaced an angle ϕ from the point source with respect to the amount of energy that would be detected if the source were being imaged directly onto the detector.

$$PSRR = \frac{P(\phi)}{P(o)} = BRDF(\phi) \cdot \Omega_{DET} \tag{5}$$

Thus, the point source rejection ratio is simply the BRDF of the system multiplied by the angular subtense of the detector being used.

4.5.2.3 Extended Source Rejection Ratio (ESRR)

For optical systems having the operational requirement that they be able to search a field of view close to a bright extended source of unwanted

energy (such as the earth), the system performance parameter of interest is the extended source rejection ratio (ESRR), which describes the ratio of amount of energy from the unwanted extended source that is detected when the system line of sight is displaced at some angle from the edge of the source divided by the amount of energy that would be detected were the source being imaged directly onto the detector. Thus, the ESRR will have the form

$$ESRR(\phi) = \frac{H(\phi)}{H(o)} \qquad (6)$$

where $H(\phi)$ = focal plane irradiance due to extended source having edge angle ϕ from detector, and $H(o)$ = focal plane irradiance due to the extended source imaged directly on detector.

The ESRR given in Eq. 7 below can be shown to be equal to the integral of the system BRDF over the offending extended source. Note that the ESRR is independent of the angular subtense of the detector size being used, unlike the PSRR.

$$ESSR = \iint_{Source} S(\phi) \, d\Omega \qquad (7)$$

4.5.2.4 Effects of a Fore-Baffle

In an effort to reduce the total irradiation of the mirrors of any system requiring high off-axis rejection, it is standard practice to place a fore-baffle in the front of the leading optical element to reduce the subtense of the source as seen by the element. The effect of a fore-baffle is to impose a weighting function $T(\phi)$ on the total irradiance of the front element. When the effect of the reduced irradiance on the optical element due to the fore-baffle is considered, the ESRR of Eq. 7 becomes

$$ESRR = \iint_{Source} S(\phi)T(o) \, d\Omega \qquad (8)$$

In Eq. 8, two basic parameters of interest are implied, α_o and ϕ_o. The first describes the angular separation between the detector of interest and the edge of the offending source, while the second is the angle at which the irradiance of the mirror goes to zero due to the existence of the fore-baffle. Thus, Eq. 8 can be written.

$$ESRR(\alpha_o, L/D) = 2 \int_{\phi_o}^{\alpha_o \sqrt{\phi_o^2 - \alpha^2}} \int_{o} T(\alpha,\beta) S(\alpha,\beta) d\alpha d\beta \qquad (9)$$

4.5.3 Relating BRDF Of The Optical Elements To System Requirements

In the telescope designs under consideration, there are two effective sources of scattered light: (1) the front refractors and (2) the primary reflector (see Figure 37). Making the assumption that the atmospheric scattered light is directly proportional to the moonlight directly illuminating the telescope, one can derive the BRDF requirement for the above elements.

Again using Eq. 6, the required system ESRR may be directly written as

$$ESRR_{req'd} = \psi_b / \psi_{moon} \qquad (10)$$

ψ_b = allowed background brightness

ψ_{moon} = brightness

In addition, the required system BRDF may also be derived directly from Eq. 10. The moon's angular subtense is considered sufficiently small as to allow Eq. 7 to be approximated as

$$ESRR = \int BRDF(\phi) \cdot d\Omega \cong BRDF(\phi) \cdot \Delta\Omega \qquad (11)$$

where $\Delta\Omega$ = angular subtense of the moon = 5.9×10^{-5} steradian

Thus, the required BRDF may be written

$$BRDF_{req'd} = \psi_b / \psi_{moon} \quad \Delta\Omega \qquad (12)$$

4.5.3.1 Simple Calculation

It is perhaps convenient at this point to use a simple calculation to gain insight to the magnitude of the BRDF required.

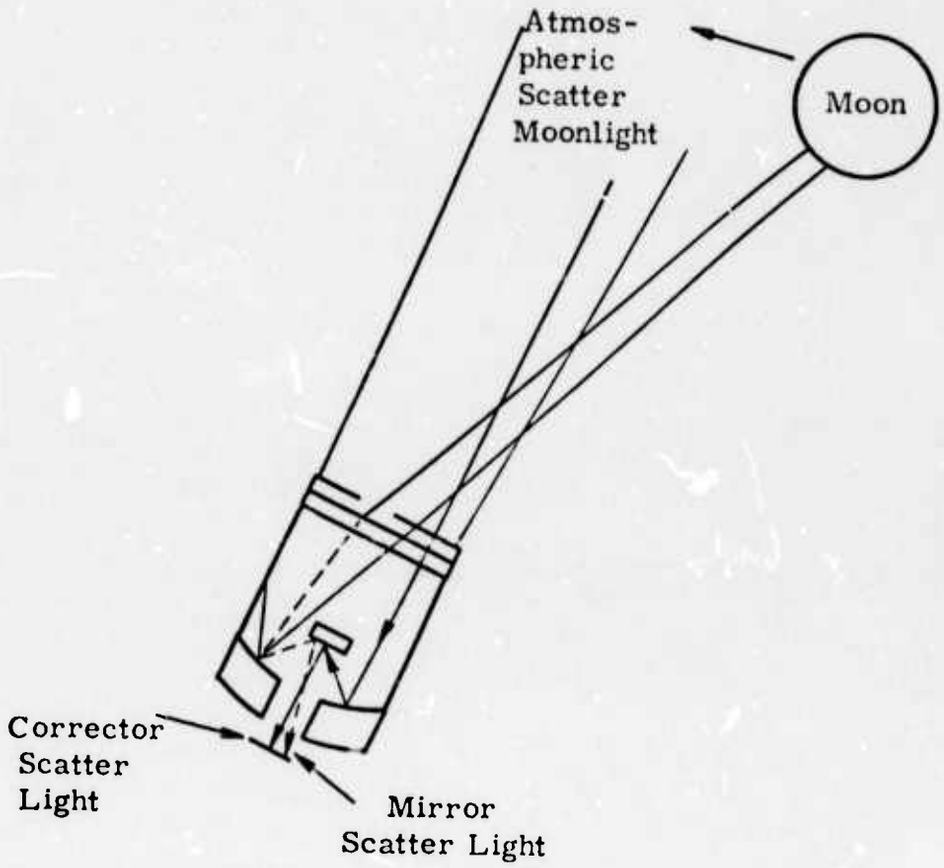

Figure 37. Sources of Scattered Light

$$K \times \eta_{opt} \times A_p \times L_{moon}(\phi) \times \frac{A_{DET}}{f^2} = \eta_{opt} \times M \cos\phi \times BRDF(\phi) \times A_{DET} \times \frac{A_p}{f^2} \quad (13)$$

where

K = 0.1 or desired attenuation of out-of-field sources

η_{opt} = optical efficiency of the system

A_p = aperture area

$L_{moon(\phi)}$ = radiance of the background - (photons/sec)/m^2-ster or other appropriate units

$\frac{A_{DET}}{f^2}$ = effective FOV of the sample area (ster)

M = irradiance of the moon on the telescope (photons/sec)/m^2

$\cos\phi$ = classical reduction in area when the area is not normal to LOS.

$BRDF(\phi)$ = fraction scatter/ster

Note $\frac{A_p}{f^2}$ = solid angle through which the detector sees the scattered light

Eliminating common terms,

$$K\, L_{moon}(\phi) = M\cos(\phi)\, BRDF(\phi) \quad (14)$$

Figure 38 shows $L_{moon}(\phi)$ as a function of angle from the moon and the phase of the moon. It was scaled from sun scattered data. Also it was assumed that either the moon is at zenith or only one air mass does the scattering. (The curve was supplied by Avco Systems Division.) The table below is extracted from the RCA E-O Handbook showing the illuminance of the moon on the earth at zenith for various phases of the moon.

θ = 100° full moon	3×10^{-1} lumens/m^2
θ = 120°	8×10^{-2}
θ = 90°	$3 \times 10^{-?}$

For a rough estimate of the BRDF, let us consider the condition of full moon at zenith and 10° from the optical axis with a small FOV on

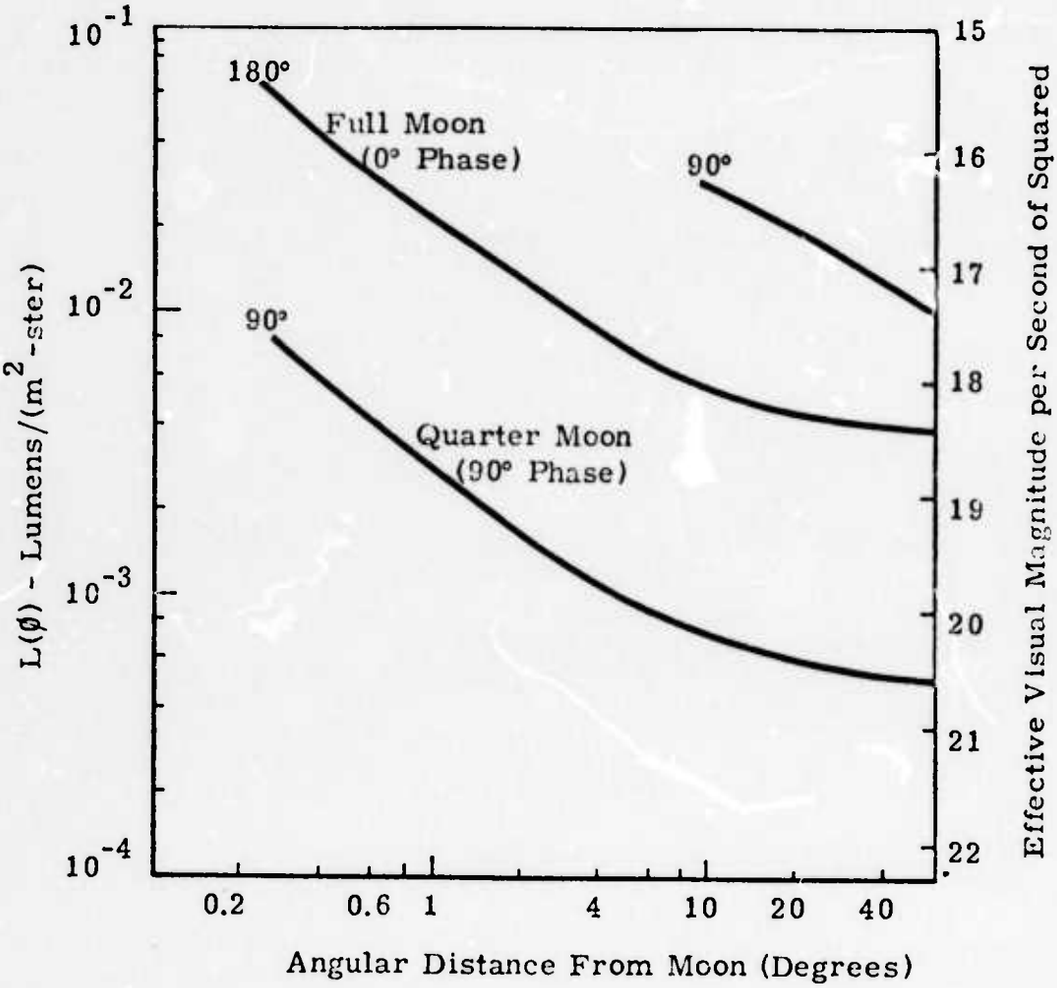

Figure 38. Atmospheric Scatter Moonlight

axis. From the table above $M = 3 \times 10^{-1}$ lumens/m^2 and form Figure 38, L_{moon} (10°) = 6×10^{-3} lumens/ster-m^2

From Eq. 14,

$$\text{BRDF } (10°) = \frac{(0.1)\ (6 \times 10^{-3})}{3 \times 10^{-1} \cos (10°)} = 2 \times 10^{-3}$$

4.5.3.2 Detailed Calculations

The results of a more rigorous calculation has been performed using the actual moon brightness and the angle dependence of both in-or out-of-field moonlight, coupled with the effect of a fore-baffle. The results are shown in Figures 39 and 40. Figure 39 shows:

a. The BRDF required for the front refractive elements in order to reduce the out-of-field energy to 0.1 of the in-field energy for various L/D ratios

b. The expected BRDF's for the same refractive elements

Note that for a typical lens, an L/D of 0.25 with a typical lens will meet the 0.1 requirement for all angles greater than 6° for the moon off the field.

Figure 40 is similar to the refractive one, except this one is for the primary mirror. The mirror inherently has an L/D = 2 because of the optical barrel.

4.5.3.3 Other Scatters

It should be noted that diffraction effects and scatter off blackened surfaces are generally well below the optical element scatter and therefore were not considered important to this first estimate.

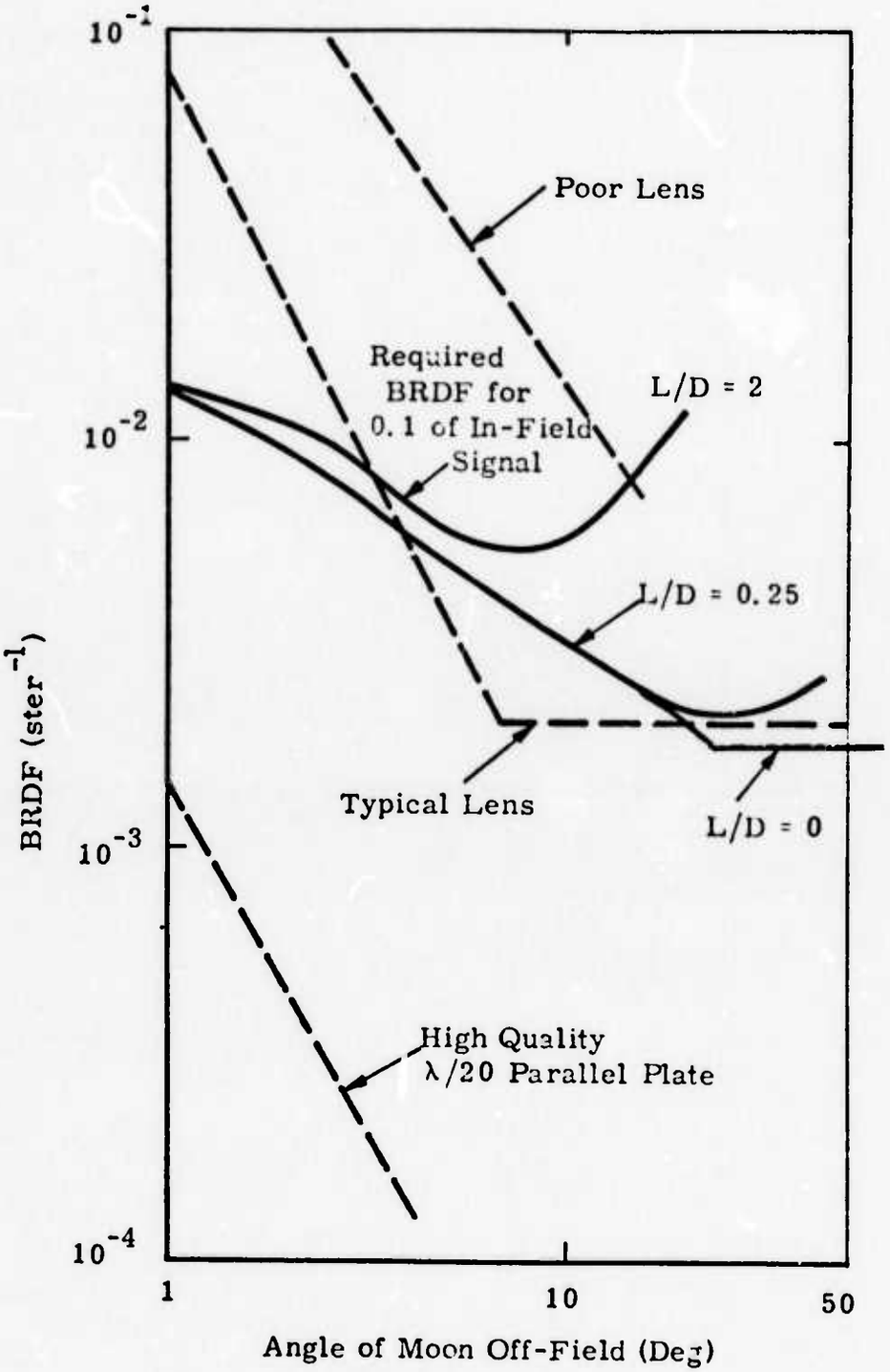

Figure 39. Refractive Optics Scatter

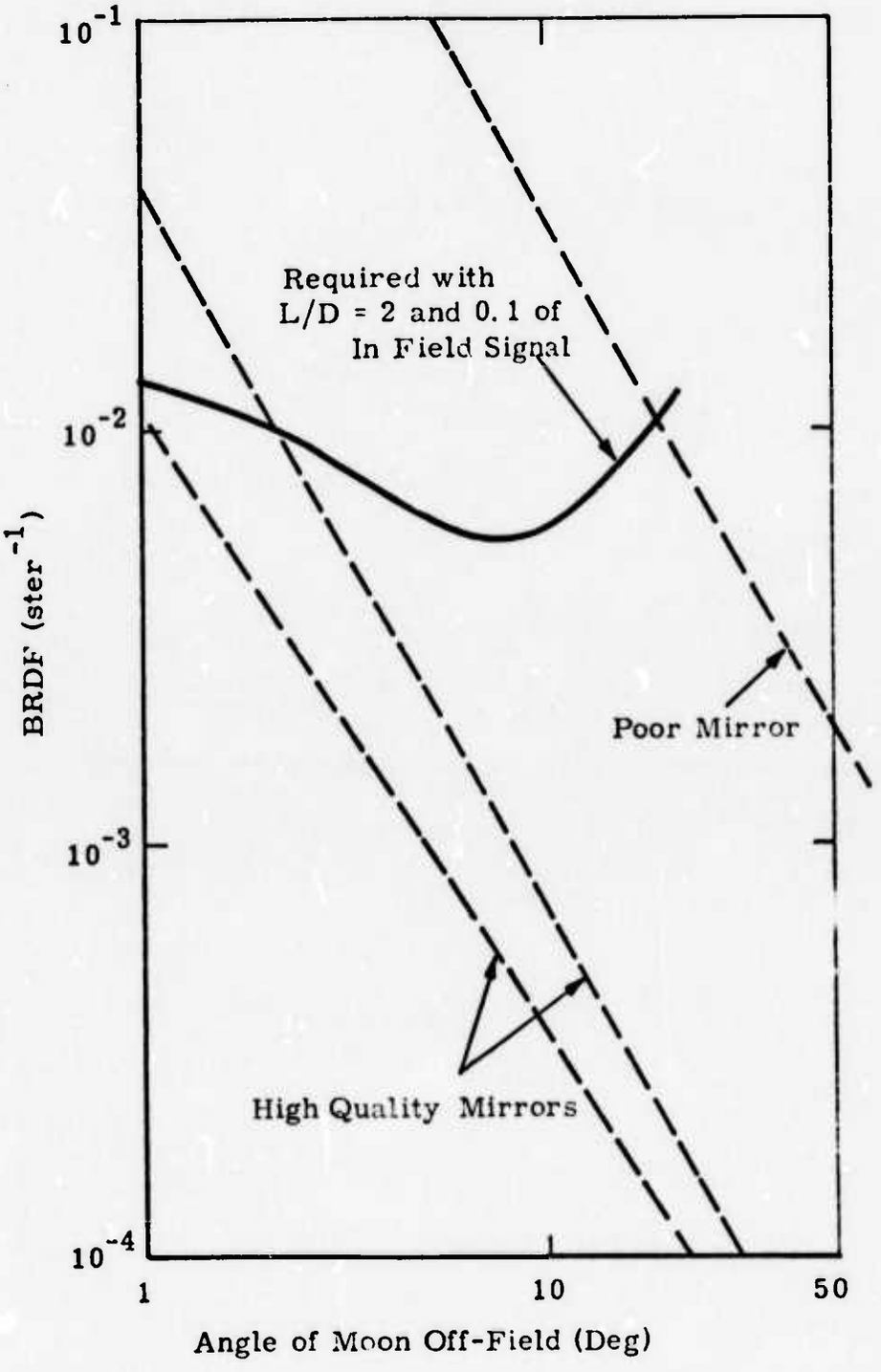

Figure 40. Primary Mirror Scatter

APPENDIX A

EQUATIONS OF MOTION OF MIRROR AND TELESCOPE

The following equations may be used to compute the motions of a mirror and telescope required to cause the reflected telescope axis to scan a great circle while keeping the focal plane rollers positioned as required to compensate image rotation. The telescope is assumed to be fixed at a site on the earth's surface with freedom to rotate about its optical axis. The mirror is assumed to be free to rotate about vertical (azimuth) horizontal (elevation) axes. The various vectors are projected onto the celestial sphere in the figure. Using the typical general case shown, we can make the following statements:

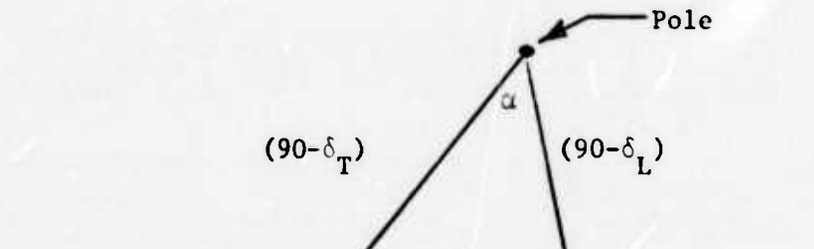

given

α_L = right ascension of location

δ_L = declination of location (latitude of site)

ψ = elevation of telescope* above local horizontal

σ = azimuth of telescope* clockwise from north

we may find

α_T = right ascension of telescope axis*

δ_T = declination of telescope axis*

---

*The telescope vector is colinear with the optical axis and points in the direction of incoming light energy.

as follows:

$$\cos (90-\delta_T) = \sin \delta_T = \sin \delta_L \sin \psi + \cos \delta_L \cos \psi \cos (-\sigma)$$

$$\sin \delta_T = \sin \delta_T \sin \psi + \cos \delta_L \cos \psi \cos \sigma$$

$$\delta_T = \square$$

and

$$\frac{\sin a}{\cos \psi} = \frac{\sin (-\sigma)}{\cos \delta_T}$$

$$\sin a = \frac{-\sin \sigma \cos \psi}{\cos \delta_T}$$

$$a = \square$$

$$\alpha_T = \alpha_L - a$$

$$\alpha_T = \square$$

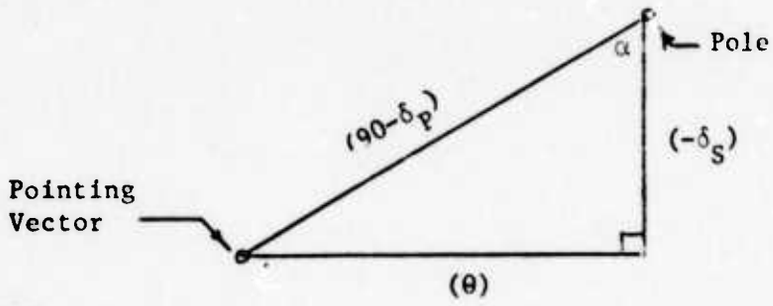

Given

α_S = right ascention of scan velocity vector

δ_S = declination of scan velocity vector

θ = scan angle = ω_{st}

we may find

α_P = right ascention of pointing vector

δ_P = declination of pointing vector

as follows:

$$\cos (90-\delta_P) = \sin \delta_P = \cos \theta \cos (-\delta_S)$$

$$\sin \delta_P = \cos \theta \cos \delta_S$$

$$\delta_P = \square$$

and

$$\frac{\sin a}{\sin \theta} = \frac{\sin (90)}{\cos (\delta_P)}, \qquad \sin a = \frac{\sin \theta}{\cos \delta_P}, \quad a = \square$$

$$\alpha_P = \alpha_S - a = \square$$

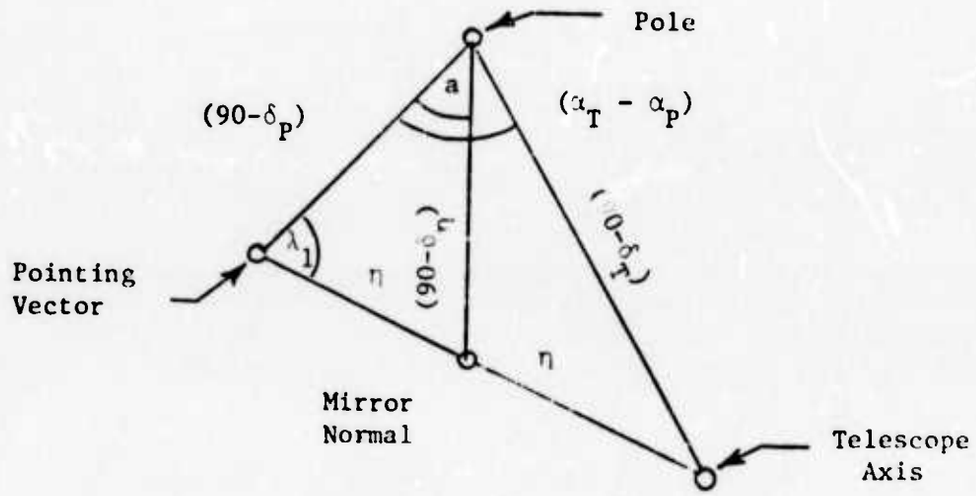

We may now compute η as follows:

$$\cos 2\eta = \sin \delta_P \sin \delta_T + \cos \delta_P \cos \delta_T \cos (\alpha_T - \alpha_P)$$

$$2\eta = \square$$

$$\eta \quad \square$$

and

α_η = right ascension of mirror normal

δ_η = declination of mirror normal

as follows:

$$\frac{\sin \lambda_1}{\cos \delta_T} = \frac{\sin (\alpha_T - \alpha_P)}{\sin 2_\eta}$$

$$\sin \lambda_1 = \frac{\cos \delta_T \sin (\alpha_T - \alpha_P)}{\sin 2_\eta}$$

$$\lambda_1 = \square$$

$$\cos (90-\delta_\eta) = \sin \delta_\eta = \sin \delta_P \cos \eta + \cos \delta_P \sin \eta \cos \lambda_1$$

$$\delta_\eta = \square$$

and

$$\frac{\sin a}{\sin \eta} = \frac{\sin \lambda_1}{\cos \delta_\eta}, \quad \sin a = \frac{\sin \eta \sin \lambda_1}{\cos \delta_\eta}$$

$$a = \square$$

$$\delta_\eta = \alpha_P + a = \square$$

Now we can find

α_M = elevation of mirror normal above loca horizontal

β_M = azimuth of mirror normal clockwise from north

as follows:

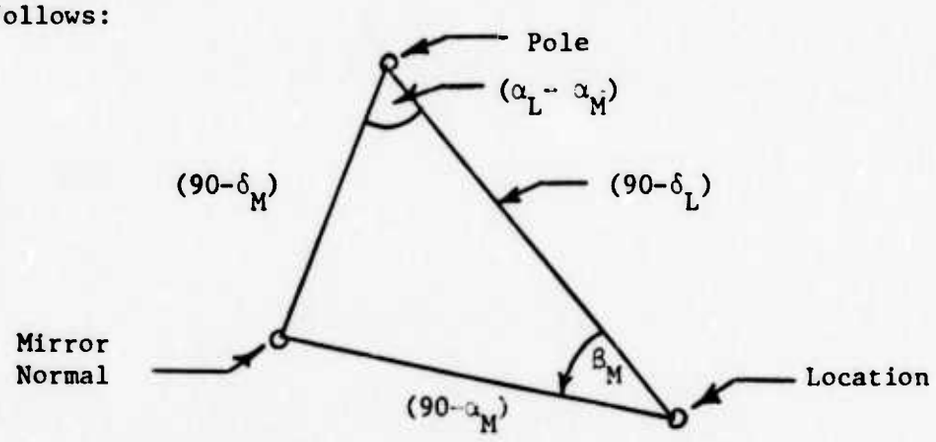

$$\cos (90-\delta_M) = \sin \alpha_M = \sin \delta_M \sin \delta_L + \cos \delta_\eta \cos \delta_L \cos (\alpha_L - \alpha_M)$$

$$\alpha_M = \square$$

$$\frac{\sin (-\beta_M)}{\cos \delta_\eta} = \frac{\sin (\alpha_L - \alpha_\eta)}{\cos \alpha_M}, \qquad \sin \beta_M = \frac{-\cos \delta_\eta \sin (\alpha_L - \alpha_M)}{\cos \alpha_M}$$

$$\beta_M = \square$$

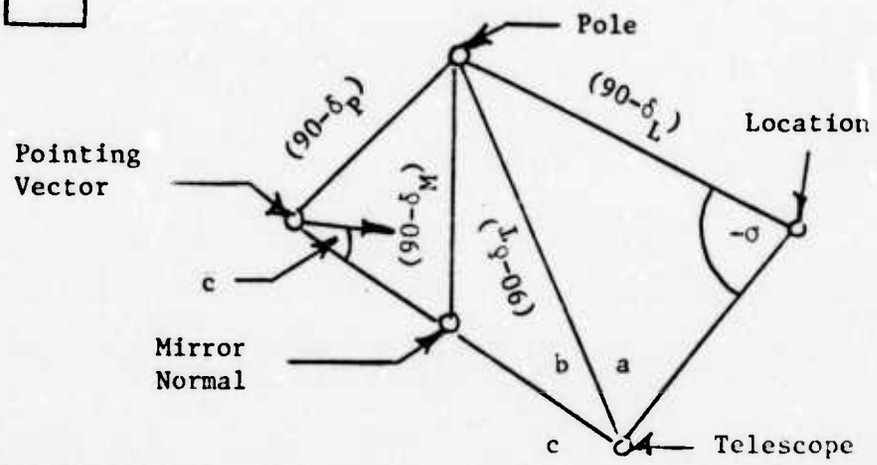

To find $\emptyset$ = rotation of telescope about optic axis from a vertical plane, we proceed as follows:

$$\emptyset = a + b + c, \quad c = \lambda_1 - 90°$$

$$\emptyset = a + b + \lambda_1 - 90°$$

$$\frac{\sin a}{\cos \delta_L} = \frac{\sin (-\sigma)}{\cos \delta_T}, \qquad \sin a = \frac{-\cos \delta_L \sin \sigma}{\cos \delta_T}$$

$$a = \square$$

$$\frac{\sin b}{\cos \delta_P} = \frac{\sin (\alpha_T - \alpha_P)}{\sin 2\eta}, \qquad \sin b = \frac{\cos \delta_P \sin (\alpha_T - \alpha_P)}{\sin 2\eta}$$

$$b = \square$$

$$\emptyset = a + b + \lambda_1 - 90° = \square$$

APPENDIX B

EQUATIONS OF MOTION OF IMAGE SPACE

Assume a telescope and mirror as shown in Figure 41 with the XYZ coordinates fixed in inertial space. The mirror has two degrees of rotational freedom: about the X axis (azimuth) and about the inersection of the mirror plane and the Y-Z plane (elevation). The optic axis is colinear with the Y axis. The mirror creates a virtual image of object-space that appears to move as the mirror is moved.

Equations are derived below that describe the apparent motion of image space as a function of mirror motion. The motion of corresponding images in the focal plane of the telescope also described.

Figure 42 shows the mirror in a typical position. If wer assume, temporarily, that α (elevation) is constant and let BAC be a disk fixed in object space, B'A'C' is the image of BAC. If we can determine the apparent motion of B'A'C' due to rotation of the mirror about the X axis (azimuth), we will have described the motion of image space.

The rotation of B'A'C' is composed of two components; rotation around the OP' axis and the motion of the OP' axis around the X axis. The magnitude of the latter is simply β, the angular velocity of the mirror.

The magnitude of the first component is determined by noting that 90° of the rotation of the mirror about X will cause A' to mate with A, which means that B'A'C' has rotated 90° on the OP' axis. The magnitude of the angular velocity about OP' is therefore also equal to $\dot{\beta}$.

Adding the two components vectorally, we find that the total is

$$\omega_{i\beta} = 2\dot{\beta} \cos \alpha \qquad (1)$$

and is located at the intersection of the mirror plane with the XON plane.

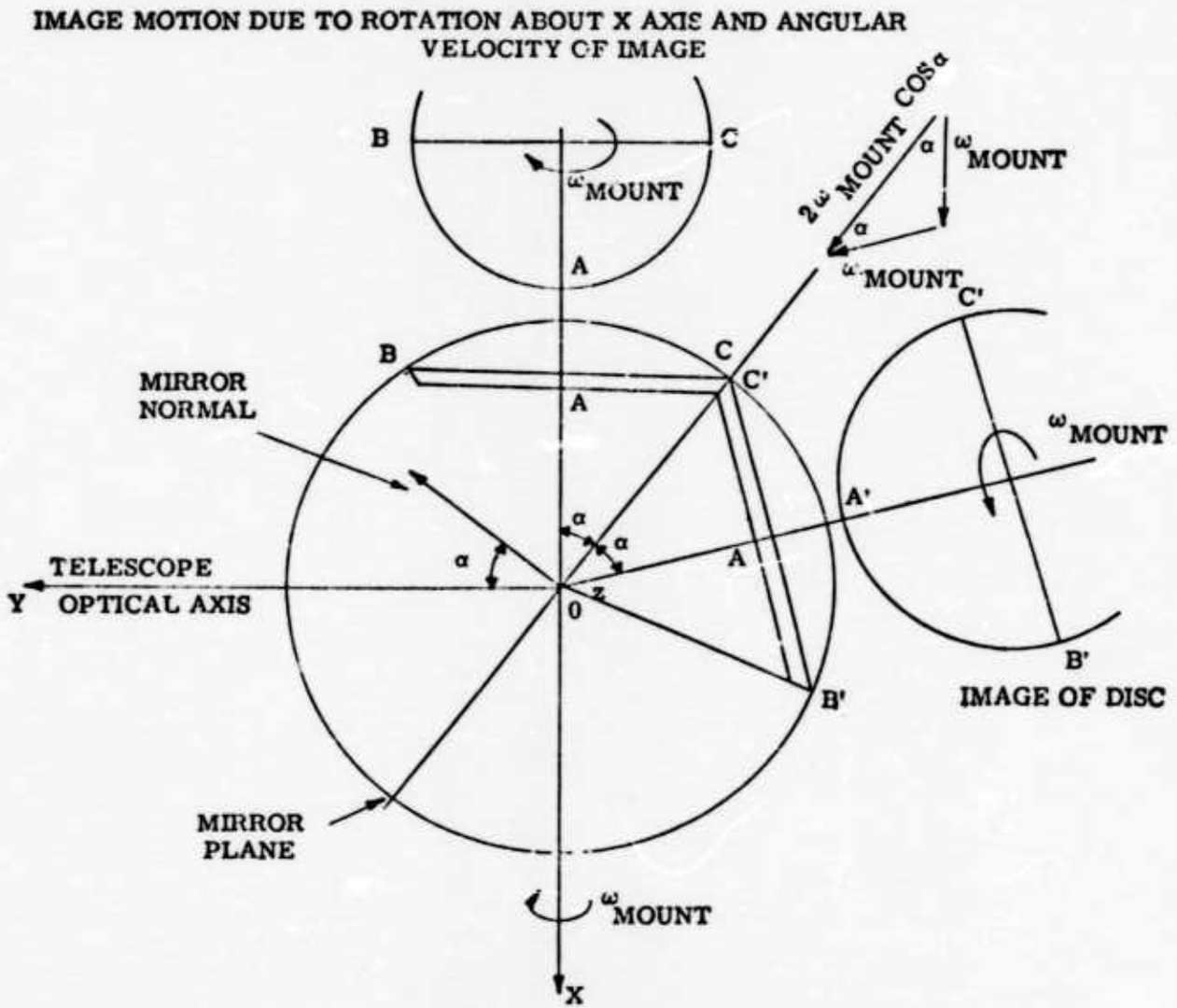

Figure 41. Image Motion Due to Rotation About X Axis and Angular Velocity of Image

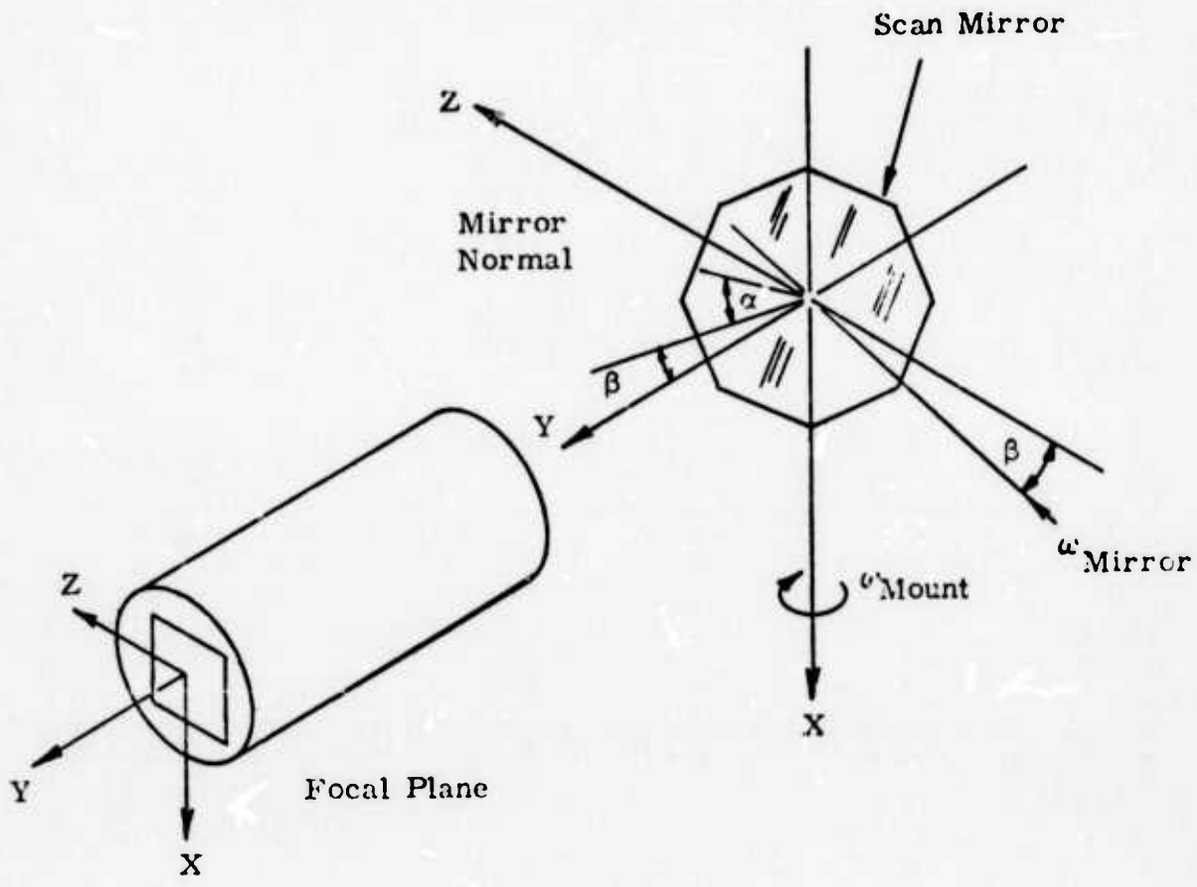

Figure 42. Definition of Variables for the Scan Mirror and Telescope

In other words, the motion of B'A'C' and, therefore, image space may be visualized by picturing the cone C'O'B' as rolling against the fixed cone COB with the line of tangency on the same plane as the X axis and the mirror normal. The angular velocity of the image cone, about the line of tangency is given by Eq. 1.

Figure 43 shows $\omega_{i\beta}$ broken into components along the Y axis and in the X-Z plane. (Note the XYZ axes have been rotated 180° around the Y axis in Figure 41 to clarify the picture.) The component along the Y, or optic, axis will cause unwanted image rotation in the focal plane. The remaining component in the X-Z plane causes image translation in the focal plane. The components are determined from Figure 43 as follows:

$$\omega_{R\beta} = \omega_{i\beta} \sin \alpha \cos \beta \tag{2}$$

$$\omega_{T\beta} = \omega_{i\beta} \sqrt{1 - (\sin \alpha \cos \beta)^2} \tag{3}$$

If we now hold β (azimuth) constant (see Figure 41) and vary α (elevation), a different situation obtains. Now all points on the axis of rotation (i.e., the intersection of the mirror plane with the Y-Z plane) have zero velocity in image-space. This line is therefore the axis of rotation of image-space. The magnitude of the angular velocity of image-space is simply.

$$\omega_{i\alpha} = 2\dot{\alpha}$$

and the components corresponding to $\omega_{R\beta}$ and $\omega_{T\beta}$ are

$$\omega_{R\alpha} = \omega_{i\alpha} \sin \beta \tag{5}$$

and

$$\omega_{T\alpha} = \omega_{i\alpha} \cos \beta \tag{6}$$

Now, combining Eq. (2) and (5) to find the total image rotation velcoity,

$$\omega_R = \omega_{i\beta} \sin \alpha \cos \beta - \omega_{i\alpha} \sin \beta$$

$$\omega_R = 2\dot{\beta} \cos \alpha \sin \alpha \cos \beta - 2\dot{\alpha} \sin \beta$$

$$\omega_R = \dot{\beta} \sin 2\alpha \cos \beta - 2\alpha \sin \beta \tag{7}$$

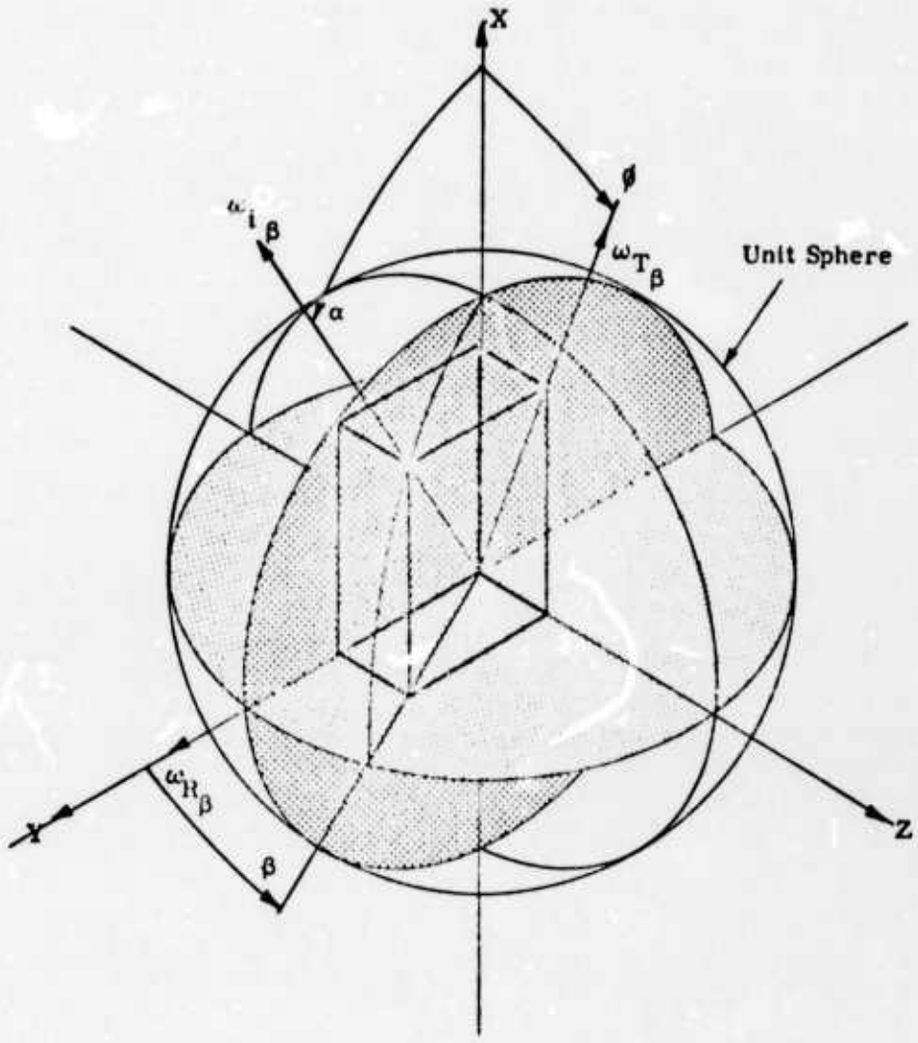

Figure 43. Image Space Motion

Similarly, finding the sum of all components along the X axis,

$$\omega_{TX} = \omega_{i\beta} \cos \alpha$$
$$\omega_{TX} = 2\dot{\beta} \cos^2 \alpha \qquad (8)$$

and along the Z axis,

$$\omega_{TZ} = \omega_{i\beta} \sin \alpha \sin \beta + \omega_{ik} \sin \beta$$
$$\omega_{TZ} = 2\dot{\beta} \cos \alpha \sin \alpha \sin \beta + 2\dot{\alpha} \cos \beta$$
$$\omega_{TZ} = \dot{\beta} \sin 2\alpha \sin \beta + 2\dot{\alpha} \cos \beta \qquad (9)$$

Equations (7), (8) and (9) can now be used to determine the velcoity components of images in the focal plane of the telescope. Assuming a focal length, f, and using the focal plane coordinates shown in Figure 41, we can say, image rotation is

$$\omega_R = \dot{\beta} \sin 2\alpha \cos \beta - 2\dot{\alpha} \sin \beta \qquad (10)$$

Image velocity in the X direction is

$$V_X = f(-\omega_{TZ}) = -f[\dot{\beta} \sin 2\alpha \sin \beta + 2\dot{\alpha} \cos \beta] \qquad (11)$$

Image velocity in the Z direction is

$$V_Z = f(\omega_{TX}) = f[2\dot{\beta} \cos^2 \alpha] \qquad (12)$$

Note that Eq. (10), (11), and (12) assume that the focal plane is spherical or that the field angle (θ) is small enough to make $\theta \rightarrow \tan \theta$. In other words, image velocity components due to mapping errors that arise when a sphere is mapped onto a plane have not been considered here.

PERKIN-ELMER
ELECTRO-OPTICAL DIVISION
NORWALK, CONNECTICUT

REPORT NO. 11984-A

ADDENDUM TO TEAL AMBER FINAL REPORT

PREPARED FOR

CBS LABORATORIES

DATE: 9 AUGUST 1974

REF: 40860-14000

1.0 INTRODUCTION

The effort in the optical design area for the Teal Amber telescope was extended to look at a variation in the all-spherical Cassegrain system which is the recommended optical form. This variation was effectively letting the focal surface be optimized for the optical system rather than being governed by the mechanical interface with the CBS camera. Also, the system would be made optically faster, F/1.2 from F/1.5. For the purpose of identification this is System E. In the data that follows, the aperture was increased and the focal length kept constant. The results of the investigation showed an increased in-system response, throughout, with image quality being superior over the other systems even though it is a faster system.

2.0 DATA PRESENTATION

Table #1 summarizes the parameters of the new System E and compares them to the recommended system in the final report (System D). Following the tables, one will find the appropriate data. All definitions are per the final report #11984. The width of LSF within which 80% of the energy is contained has been added to the table for comparison. This information is obtained from the column DE in the tabular data. (1 arc-sec $\simeq$ 5.5μ). An examination of the classical h-tan u curves show that color should not be a problem and can be controlled such that the data shown is representative of the systems polychromatic response. One should note that the second optical surface is an aspheric which is very mild, however, all the glass is still BK7.

3.0 SUMMARY

From the optical system viewpoint, System E is superior. It yields equal to or better than any of the previous systems. The fact that the system is optically faster implies high concentration of photons per unit area at the photocathode. One can make use of the increased aperture area (1.56 times larger) hence collect more photons, or scale the system down to 30" and have a higher concentration of photons in a smaller area. The main disadvantage is the location of the focal surface. It is well forward of the primary mirror vertex (0.37m or 14.6 inches) and close to the field elements (0.096m or 3.8 inches). One should also note that the volume available for the camera is not a cylinder of radius (0.4m or 15.7 inches) but a truncated cone. The cone is limited by the rays leaving the primary and approaching the secondary.

Note: All Dimensions in Meters

F/No. 1.2
Aperture 0.96 Meter
(Diameter)
Focal Length 1.14 Meters
Obscuration ≈ 30%
Thruput > 55%

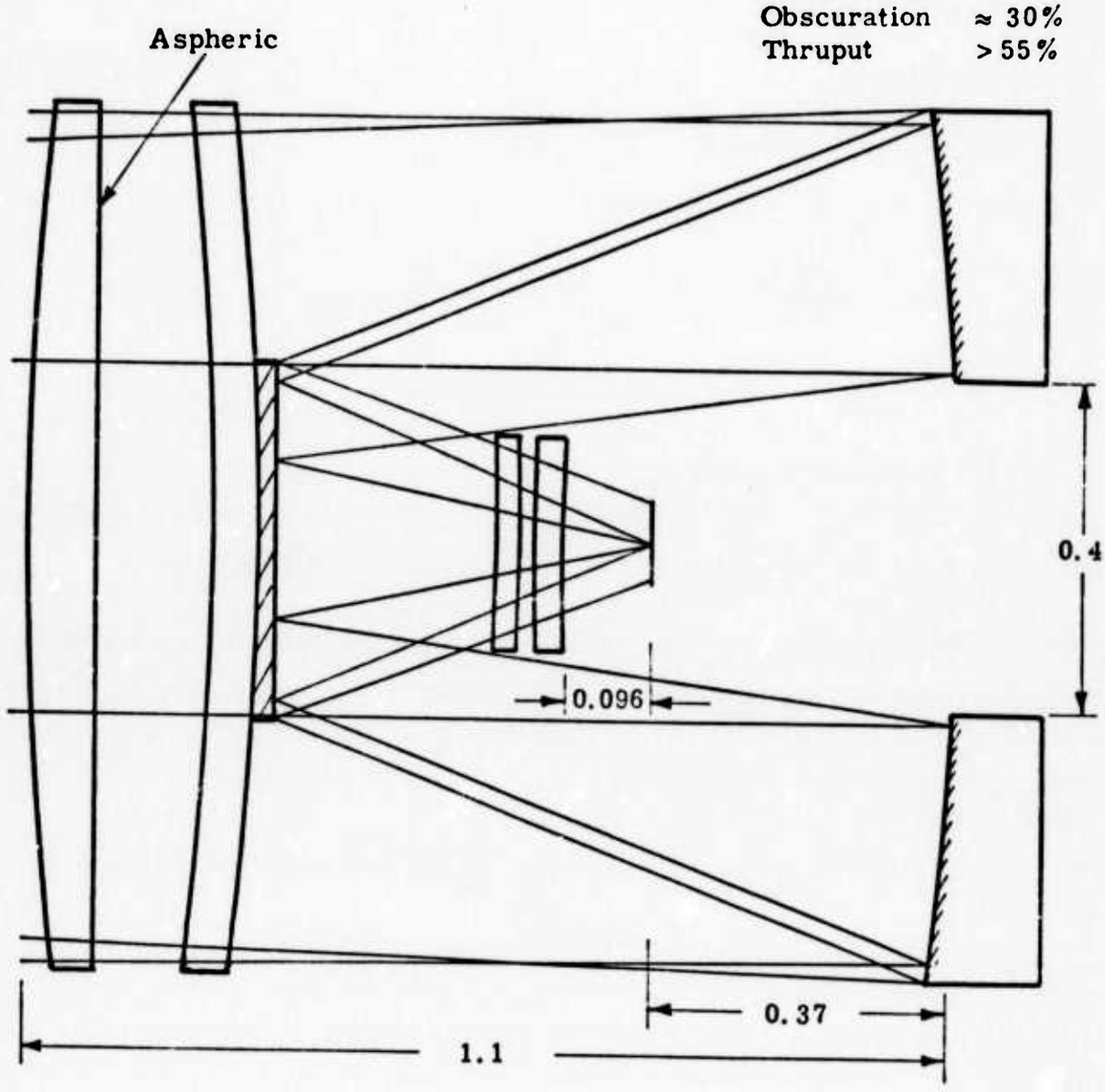

Figure 1. System E Optical Schematic

TABLE 1. COMPARISION OF SYSTEM D AND SYSTEM E

Parameter		System D	System E
F/#		F/1.5	F/1.2
Aper Diam		0.76m (30")	0.96m (38")
Focal Length		1.14m	1.14m
Optical EFF		51%	55%
MTF (10c/mm) at	0°	0.95	0.92
	2.5°Radial	0.83	0.96
	2.5°Tangential	0.75	0.88
FM	0°	0.49	0.51*
	2.5°Radial	0.45	0.53*
	2.5°Tangential	0.41	0.48*
80% Energy LSF	0°	1.3 arc-sec	2.1 arc-sec
	2.5°Radial	2.3 arc-sec	2.0 arc-sec
	2.5°Tangential	2.5 arc-sec	1.6 arc-sec
Simplicity		All Spheres	1 Aspheric

*This comparison does not include increase in aperture.

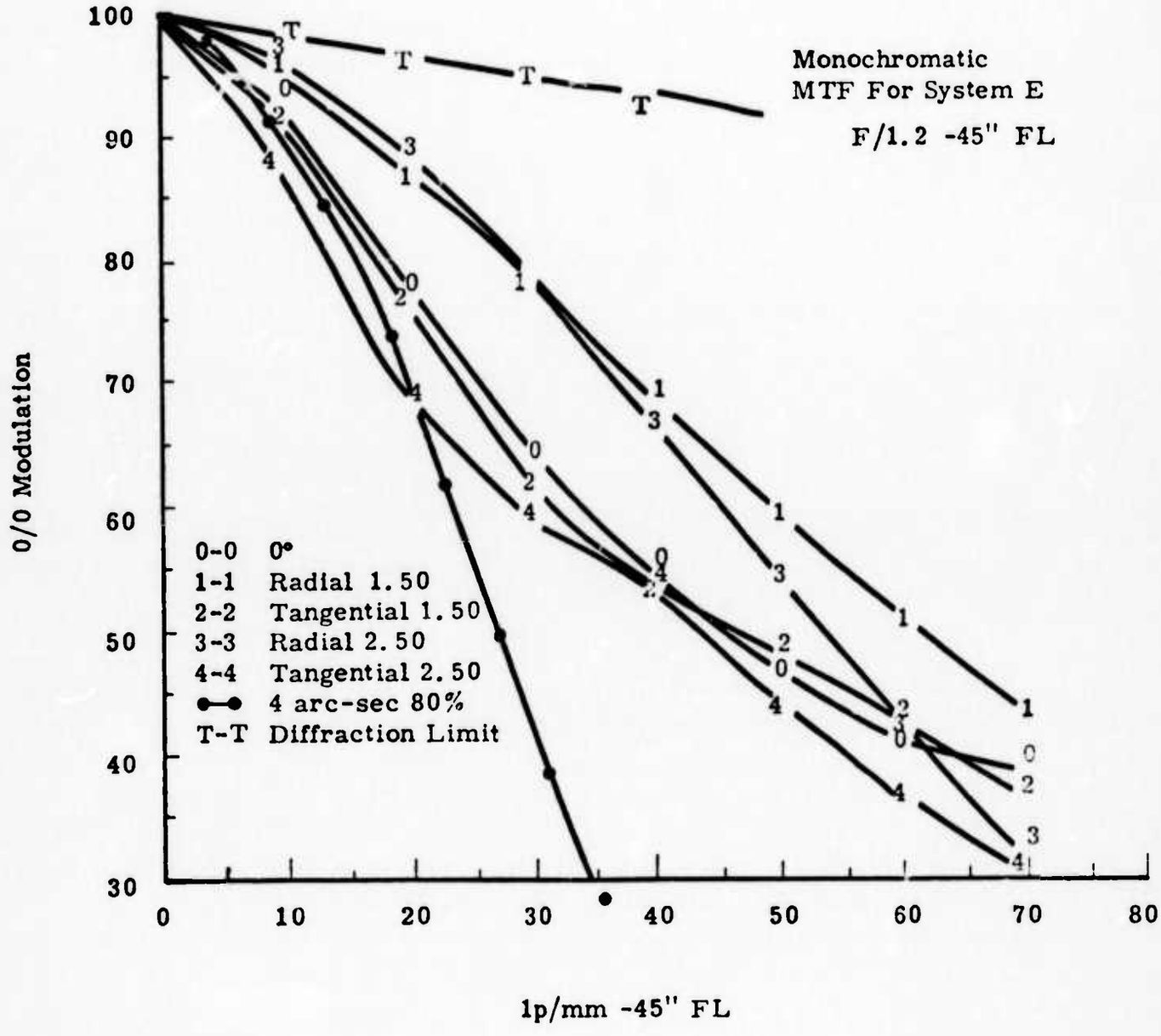
Monochromatic
MTF For System E
F/1.2 -45" FL
0/0 Modulation
1p/mm -45" FL
0-0 0°
1-1 Radial 1.50
2-2 Tangential 1.50
3-3 Radial 2.50
4-4 Tangential 2.50
4 arc-sec 80%
T-T Diffraction Limit
100
90
80
70
60
50
40
30
0
10
20
30
40
50
60
70
80

RAUL 11:24:04 07/29/74
CYCLE 12

MONOCHROMATIC O.T.F.

WAVELENGTH 0.0005876 FIELD 0.0 0.0

LINES PARALLEL TO RADIAL DIR.

FREQ	THEOR	MTF	REAL	IMAG	PHASE
10.	0.983	0.923	0.923	0.0	0.0
20.	0.967	0.779	0.779	0.0	0.0
30.	0.950	0.640	0.640	0.0	0.0
40.	0.933	0.536	0.536	0.0	0.0
50.	0.916	0.467	0.467	0.0	0.0
60.	0.900	0.420	0.420	0.0	0.0
70.	0.883	0.385	0.385	0.0	0.0

RAUL 11:24:04 07/29/74
CYCLE 12

MONOCHROMATIC O.T.F.

WAVELENGTH 0.0005876 FIELD 1.50 0.0

	LINES PARALLEL TO RADIAL DIR.						LINES PARALLEL TO TANGENTIAL DIR.				
FREQ	THEOR	MTF	REAL	IMAG	PHASE		THEOR	MTF	REAL	IMAG	PHASE
10.	0.983	0.955	0.955	0.0	0.0	*	0.983	0.920	0.891	-0.231	-0.254
20.	0.966	0.871	0.871	0.0	0.0	*	0.966	0.764	0.696	-0.316	-0.427
30.	0.950	0.775	0.775	0.0	0.0	*	0.950	0.621	0.551	-0.288	-0.482
40.	0.933	0.680	0.680	0.0	0.0	*	0.933	0.537	0.478	-0.246	-0.475
50.	0.916	0.591	0.591	0.0	0.0	*	0.916	0.484	0.426	-0.230	-0.494
60.	0.899	0.509	0.509	0.0	0.0	*	0.899	0.425	0.364	-0.219	-0.542
70.	0.883	0.434	0.434	0.0	0.0	*	0.883	0.358	0.301	-0.195	-0.574

RAUL
CYCLE 12

11:24:04 07/29/74

MONOCHROMATIC O.T.F.

WAVELENGTH 0.0005876 FIELD 2.50 0.0

	LINES PARALLEL TO RADIAL DIR.						LINES PARALLEL TO TANGENTIAL DIR.				
FREQ	THEOR	MTF	REAL	IMAG	PHASE		THEOR	MTF	REAL	IMAG	PHASE
10.	0.983	0.962	0.962	0.0	0.0	*	0.983	0.875	0.844	0.228	0.263
20.	0.966	0.888	0.888	0.0	0.0	*	0.966	0.682	0.640	0.235	0.351
30.	0.950	0.787	0.787	0.0	0.0	*	0.950	0.596	0.559	0.206	0.353
40.	0.933	0.669	0.669	0.0	0.0	*	0.933	0.532	0.475	0.239	0.466
50.	0.916	0.545	0.545	0.0	0.0	*	0.916	0.434	0.360	0.241	0.590
60.	0.899	0.426	0.426	0.0	0.0	*	0.899	0.359	0.284	0.220	0.659
70.	0.883	0.318	0.318	0.0	0.0	*	0.882	0.311	0.222	0.218	0.776

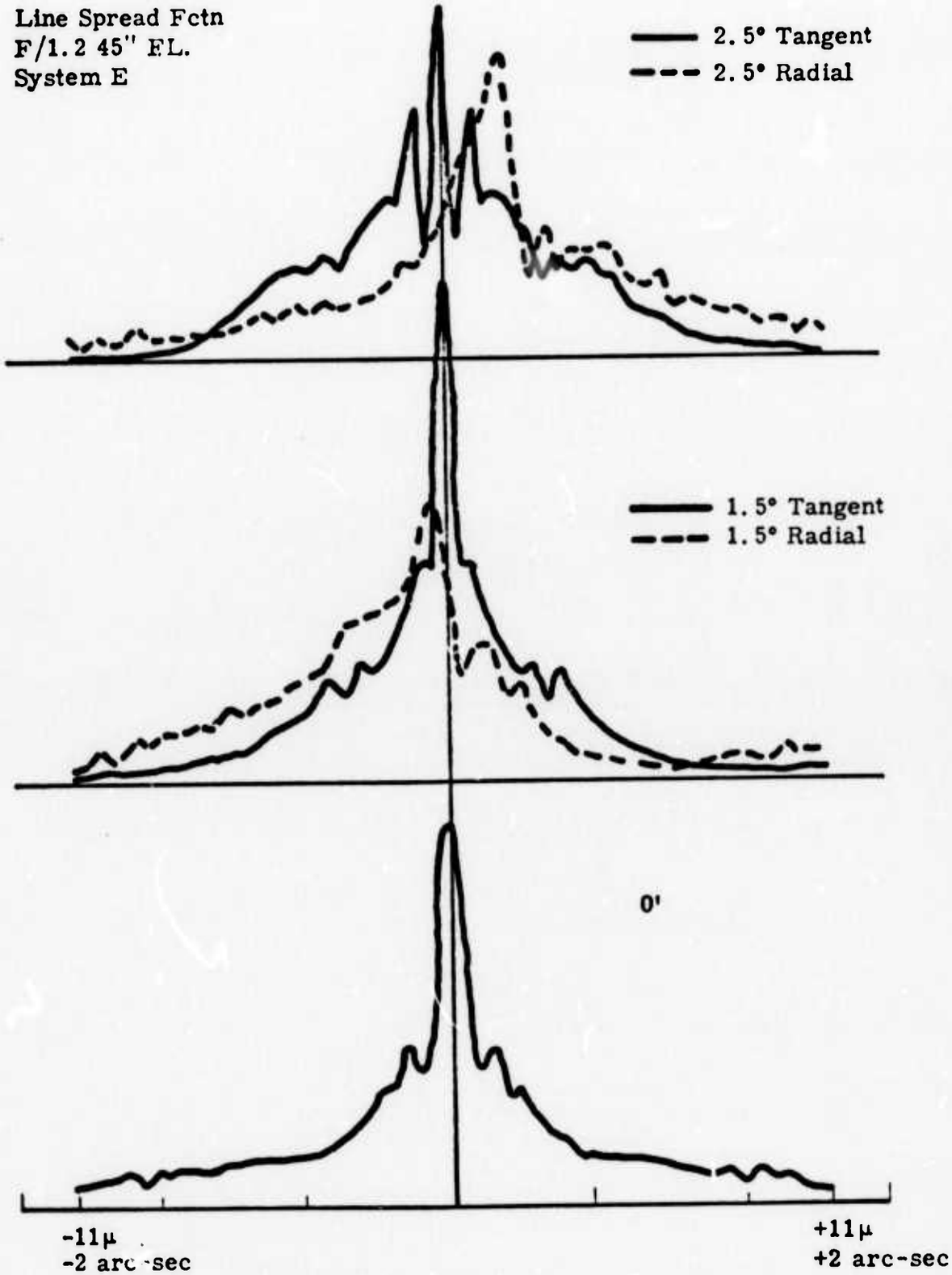
Line Spread Fctn
F/1.2 45" FL.
System E
2.5° Tangent
2.5° Radial
1.5° Tangent
1.5° Radial
0'
-11μ
-2 arc-sec
+11μ
+2 arc-sec

LINE SPREAD FUNCTION

WAVELENGTH 0.0005876 E.F.L. 1143.0 FIELD 0.0

LIM. FREQ. 1418.16 CYCLES/MM NORMALIZING FACTOR 3.058

TANGENTIAL SCAN

NO.	Z	I	DE
-130	-0.01146	0.0164	0.0067
-125	-0.01102	0.0165	0.0072
-120	-0.01058	0.0181	0.0071
-115	-0.01014	0.0180	0.0085
-110	-0.00970	0.0214	0.0074
-105	-0.00925	0.0165	0.0080
-100	-0.00881	0.0220	0.0085
-95	-0.00837	0.0190	0.0080
-90	-0.00793	0.0218	0.0095
-85	-0.00749	0.0228	0.0088
-80	-0.00705	0.0220	0.0096
-75	-0.00661	0.0245	0.0107
-70	-0.00617	0.0280	0.0113
-65	-0.00573	0.0271	0.0114
-60	-0.00529	0.0279	0.0112
-55	-0.00485	0.0286	0.0124
-50	-0.00441	0.0300	0.0119
-45	-0.00397	0.0303	0.0147
-40	-0.00353	0.0419	0.0180
-35	-0.00309	0.0446	0.0202
-30	-0.00264	0.0592	0.0286
-25	-0.00220	0.0750	0.0294
-20	-0.00176	0.0741	0.0398
-15	-0.00132	0.1232	0.0504
-10	-0.00088	0.1100	0.0493
-5	-0.00044	0.1623	0.0942
0	0.0	0.2739	0.0942
5	0.00044	0.1623	0.0493
10	0.00088	0.1100	0.0504
15	0.00132	0.1232	0.0399
20	0.00176	0.0741	0.0294
25	0.00220	0.0750	0.0286
30	0.00264	0.0592	0.0202
35	0.00309	0.0446	0.0180
40	0.00353	0.0419	0.0147
45	0.00397	0.0303	0.0119
50	0.00441	0.0300	0.0124
55	0.00485	0.0286	0.0112
60	0.00529	0.0279	0.0114
65	0.00573	0.0271	0.0113
70	0.00617	0.0280	0.0107
75	0.00661	0.0245	0.0096
80	0.00705	0.0220	0.0088
85	0.00749	0.0228	0.0095
90	0.00793	0.0218	0.0080
95	0.00837	0.0190	0.0085
100	0.00881	0.0220	0.0080
105	0.00925	0.0165	0.0074
110	0.00970	0.0214	0.0085
115	0.01014	0.0180	0.0071
120	0.01058	0.0181	0.0072
125	0.01102	0.0165	0.0067
130	0.01146	0.0164	0.0070

[illegible] SPREAD FUNCTION

WAVELENGTH 0.0005876 E.F.L. 1143.0 FIELD 1.50

LIN. FREQ. 1416.71 CYCLES/MM NORMALIZING FACTOR 3.058

RADIAL SCAN

NO.	Y	I	DE
-130	-0.01147	0.0190	0.0068
-125	-0.01103	0.0173	0.0087
-120	-0.01059	0.0219	0.0073
-115	-0.01015	0.0162	0.0075
-110	-0.00971	0.0205	0.0093
-105	-0.00926	0.0247	0.0097
-100	-0.00882	0.0225	0.0104
-95	-0.00838	0.0294	0.0122
-90	-0.00794	0.0298	0.0131
-85	-0.00750	0.0342	0.0138
-80	-0.00706	0.0338	0.0158
-75	-0.00662	0.0443	0.0180
-70	-0.00618	0.0417	0.0179
-65	-0.00574	0.0483	0.0205
-60	-0.00529	0.0498	0.0214
-55	-0.00485	0.0573	0.0249
-50	-0.00441	0.0632	0.0274
-45	-0.00397	0.0723	0.0318
-40	-0.00353	0.0837	0.0376
-35	-0.00309	0.1004	0.0425
-30	-0.00265	0.1035	0.0427
-25	-0.00221	0.1092	0.0464
-20	-0.00176	0.1140	0.0468
-15	-0.00132	0.1211	0.0506
-10	-0.00088	0.1508	0.0696
-5	-0.00044	0.1784	0.0674
0	0.0	0.1380	0.0400
5	0.00044	0.0653	0.0278
10	0.00088	0.0828	0.0367
15	0.00132	0.0843	0.0278
20	0.00176	0.0575	0.0250
25	0.00221	0.0654	0.0232
30	0.00265	0.0434	0.0147
35	0.00309	0.0342	0.0130
40	0.00353	0.0257	0.0082
45	0.00397	0.0167	0.0065
50	0.00441	0.0155	0.0062
55	0.00485	0.0138	0.0053
60	0.00529	0.0141	0.0060
65	0.00574	0.0137	0.0055
70	0.00618	0.0146	0.0055
75	0.00662	0.0111	0.0045
80	0.00706	0.0118	0.0049
85	0.00750	0.0123	0.0055
90	0.00794	0.0136	0.0052
95	0.00838	0.0135	0.0060
100	0.00882	0.0139	0.0054
105	0.00926	0.0153	0.0069
110	0.00971	0.0161	0.0068
115	0.01015	0.0191	0.0078
120	0.01059	0.0176	0.0076
125	0.01103	0.0198	0.0071
130	0.01147	0.0159	0.0082

[illegible] SPHERICAL ABERRATION

WAVELENGTH 0.0005876 E.F.L. 1143.0 FIELD 1.50

LIM. FREQ. 1417.63 CYCLES/MM NORMALIZING FACTOR 3.058

TANGENTIAL SCAN

NO.	Z	I	DE
-130	-0.01146	0.0071	0.0029
-125	-0.01102	0.0074	0.0030
-120	-0.01058	0.0071	0.0030
-115	-0.01014	0.0078	0.0031
-110	-0.00970	0.0077	0.0033
-105	-0.00926	0.0079	0.0034
-100	-0.00882	0.0090	0.0037
-95	-0.00838	0.0093	0.0043
-90	-0.00794	0.0111	0.0043
-85	-0.00749	0.0102	0.0048
-80	-0.00705	0.0135	0.0066
-75	-0.00661	0.0141	0.0073
-70	-0.00617	0.0174	0.0076
-65	-0.00573	0.0202	0.0098
-60	-0.00529	0.0290	0.0132
-55	-0.00485	0.0346	0.0163
-50	-0.00441	0.0461	0.0200
-45	-0.00397	0.0520	0.0250
-40	-0.00353	0.0686	0.0255
-35	-0.00309	0.0560	0.0270
-30	-0.00265	0.0790	0.0318
-25	-0.00220	0.0731	0.0323
-20	-0.00176	0.0855	0.0365
-15	-0.00132	0.1044	0.0546
-10	-0.00088	0.1413	0.0498
-5	-0.00044	0.1413	0.1024
0	0.0	0.3305	0.1024
5	0.00044	0.1413	0.0498
10	0.00088	0.1413	0.0546
15	0.00132	0.1044	0.0365
20	0.00176	0.0855	0.0323
25	0.00220	0.0731	0.0318
30	0.00265	0.0790	0.0270
35	0.00309	0.0560	0.0255
40	0.00353	0.0686	0.0250
45	0.00397	0.0520	0.0200
50	0.00441	0.0461	0.0163
55	0.00485	0.0346	0.0132
60	0.00529	0.0290	0.0098
65	0.00573	0.0202	0.0076
70	0.00617	0.0174	0.0073
75	0.00661	0.0141	0.0066
80	0.00705	0.0135	0.0048
85	0.00749	0.0102	0.0043
90	0.00794	0.0111	0.0043
95	0.00838	0.0093	0.0037
100	0.00882	0.0090	0.0034
105	0.00926	0.0079	0.0033
110	0.00970	0.0077	0.0031
115	0.01014	0.0078	0.0030
120	0.01058	0.0071	0.0030
125	0.01102	0.0074	0.0029
130	0.01146	0.0071	0.0030

IE S D F ION

WAVELENGTH 0.0005876 E.F.L. 1143.0 FIELD 2.50

LIM. FREQ. 1414.64 CYCLES/MM NORMALIZING FACTOR 3.058

RADIAL SCAN

NO.	Y	I	DE
-130	-0.01149	0.0188	0.0065
-125	-0.01105	0.0133	0.0057
-120	-0.01060	0.0160	0.0072
-115	-0.01016	0.0167	0.0054
-110	-0.00972	0.0117	0.0063
-105	-0.00928	0.0185	0.0066
-100	-0.00884	0.0124	0.0049
-95	-0.00839	0.0144	0.0067
-90	-0.00795	0.0162	0.0061
-85	-0.00751	0.0148	0.0062
-80	-0.00707	0.0155	0.0068
-75	-0.00663	0.0177	0.0075
-70	-0.00619	0.0195	0.0085
-65	-0.00574	0.0218	0.0100
-60	-0.00530	0.0276	0.0106
-55	-0.00486	0.0233	0.0110
-50	-0.00442	0.0327	0.0130
-45	-0.00398	0.0288	0.0125
-40	-0.00353	0.0343	0.0138
-35	-0.00309	0.0315	0.0137
-30	-0.00265	0.0384	0.0159
-25	-0.00221	0.0406	0.0160
-20	-0.00177	0.0423	0.0213
-15	-0.00133	0.0594	0.0239
-10	-0.00088	0.0588	0.0279
-5	-0.00044	0.0778	0.0328
0	0.0	0.0824	0.0402
5	0.00044	0.1204	0.0564
10	0.00088	0.1482	0.0621
15	0.00133	0.1602	0.0735
20	0.00177	0.1954	0.0690
25	0.00221	0.1191	0.0289
30	0.00265	0.0489	0.0308
35	0.00309	0.1024	0.0393
40	0.00353	0.0785	0.0309
45	0.00398	0.0865	0.0378
50	0.00442	0.0834	0.0265
55	0.00486	0.0560	0.0264
60	0.00530	0.0716	0.0264
65	0.00574	0.0529	0.0183
70	0.00619	0.0438	0.0202
75	0.00663	0.0507	0.0167
80	0.00707	0.0317	0.0136
85	0.00751	0.0364	0.0143
90	0.00795	0.0287	0.0096
95	0.00839	0.0229	0.0101
100	0.00884	0.0245	0.0092
105	0.00928	0.0212	0.0080
110	0.00972	0.0187	0.0085
115	0.01016	0.0216	0.0071
120	0.01060	0.0142	0.0069
125	0.01105	0.0152	0.0059
130	0.01149	0.0140	0.0055

[illegible] ENERGY SUM 1.0111

[illegible] SPREAD FUNCTION

WAVELENGTH 0.0005876 E.F.L. 1143.0 FIELD 2.50

LIM. FREQ. 1416.72 CYCLES/MM NORMALIZING FACTOR 3.058

TANGENTIAL SCAN

NO.	Z	I	DE
-130	-0.01147	0.0030	0.0011
-125	-0.01103	0.0034	0.0013
-120	-0.01059	0.0026	0.0014
-115	-0.01015	0.0043	0.0015
-110	-0.00971	0.0034	0.0015
-105	-0.00926	0.0034	0.0016
-100	-0.00882	0.0051	0.0022
-95	-0.00838	0.0061	0.0033
-90	-0.00794	0.0092	0.0038
-85	-0.00750	0.0104	0.0050
-80	-0.00706	0.0140	0.0075
-75	-0.00662	0.0226	0.0099
-70	-0.00618	0.0265	0.0131
-65	-0.00574	0.0374	0.0177
-60	-0.00529	0.0499	0.0216
-55	-0.00485	0.0548	0.0239
-50	-0.00441	0.0604	0.0233
-45	-0.00397	0.0565	0.0259
-40	-0.00353	0.0669	0.0242
-35	-0.00309	0.0539	0.0266
-30	-0.00265	0.0791	0.0342
-25	-0.00221	0.0877	0.0417
-20	-0.00176	0.1121	0.0421
-15	-0.00132	0.1069	0.0606
-10	-0.00088	0.1646	0.0418
-5	-0.00044	0.0668	0.0635
0	0.0	0.2305	0.0635
5	0.00044	0.0668	0.0418
10	0.00088	0.1646	0.0606
15	0.00132	0.1069	0.0421
20	0.00176	0.1121	0.0417
25	0.00221	0.0877	0.0342
30	0.00265	0.0791	0.0266
35	0.00309	0.0539	0.0242
40	0.00353	0.0669	0.0259
45	0.00397	0.0565	0.0233
50	0.00441	0.0604	0.0239
55	0.00485	0.0548	0.0216
60	0.00529	0.0499	0.0177
65	0.00574	0.0374	0.0131
70	0.00618	0.0265	0.0099
75	0.00662	0.0226	0.0075
80	0.00706	0.0140	0.0050
85	0.00750	0.0104	0.0038
90	0.00794	0.0092	0.0033
95	0.00838	0.0061	0.0022
100	0.00882	0.0051	0.0016
105	0.00926	0.0034	0.0015
110	0.00971	0.0034	0.0015
115	0.01015	0.0043	0.0014
120	0.01059	0.0026	0.0013
125	0.01103	0.0034	0.0011
130	0.01147	0.0030	0.0014

APPENDIX II

IMAGE SECTION DISTORTION ANALYSIS FOR PANORAMIC SCANNING CAMERA

TABLE OF CONTENTS

LIST OF ILLUSTRATIONS

APPENDIX II

IMAGE SECTION DISTORTION ANALYSIS FOR PANORAMIC SCANNING CAMERA

II.1. INTRODUCTION

(U) In determining the camera configuration for use in this application, the advantages and disadvantages of a drum type vs. tape transport type camera must be considered. Such factors as reliability, camera size vs. total storage area, image distortion and image degradation must be considered in selecting the type of transport. As part of this study, an image section distortion analysis has been made for a drum type camera. The purpose of this analysis is to identify the factors contributing to image distortion and degradation in such a configuration and to determine the magnitude of the distortion associated with each factor.

(U) While only the drum-type configuration is considered in this analysis, many of the results and conclusions from this analysis are directly applicable to an analysis of a tape transport camera where tape flexure rather than drum curvature must be considered.

II.2. FACTORS CONTRIBUTING TO IMAGE DISTORTION AND DEGRADATION

(U) Mounting the storage tape onto the surface of a drum introduces certain factors which will tend to distort and degrade the electron image as

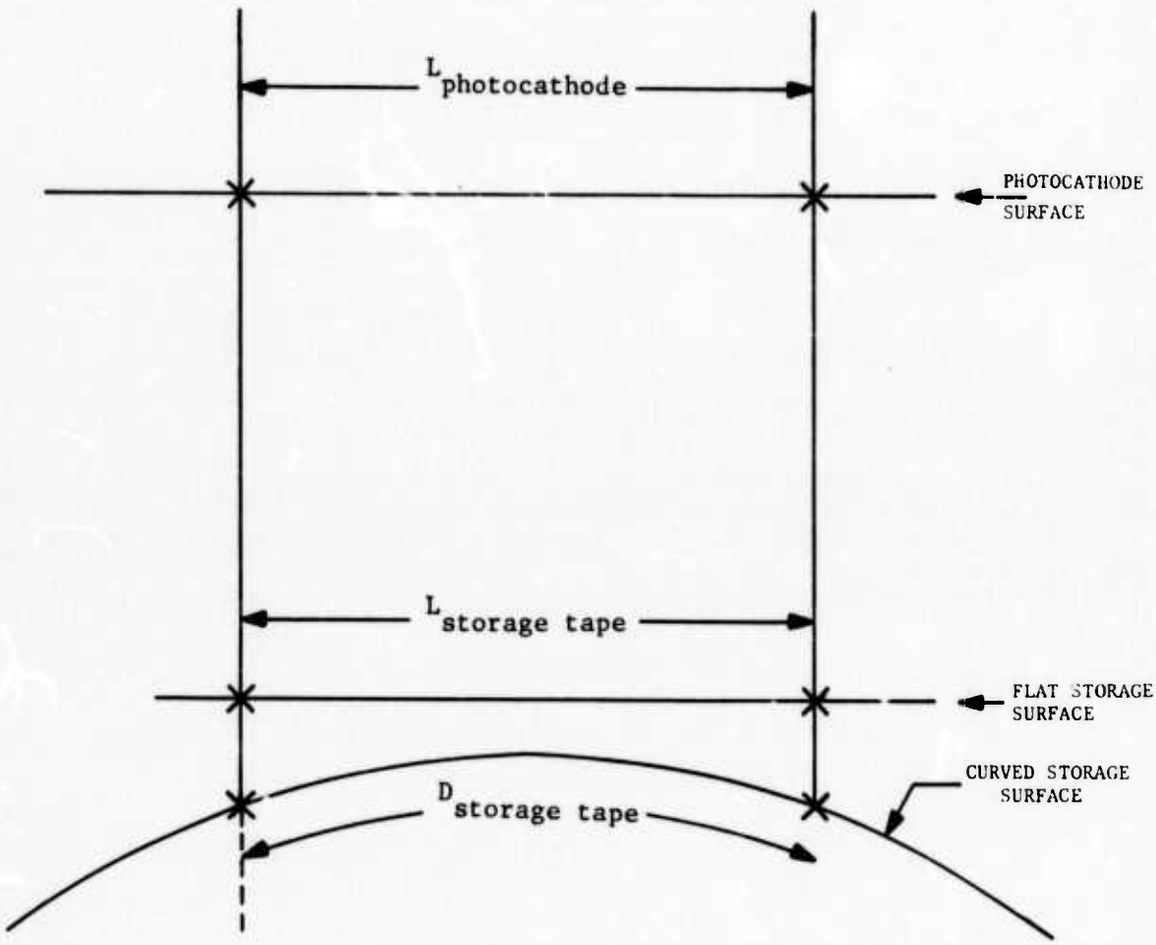

Figure 1. MAPPING GEOMETRY

it is transferred from the photocathode to the storage tape. These factors include mapping errors, sagittal errors and non-uniform electric and magnetic field errors. Each of these factors is described in detail below.

II.3. MAPPING A PLANE SURFACE ONTO A CURVED SURFACE

(U) In the electromagnetic image section being proposed for this camera, the photoelectrons which do not exit normal to the photocathode plane describe helical paths in going from the photocathode to the storage tape. However, the guiding center of each of these paths, as well as the actual trajectories of those electrons exiting normal to the photocathode surface, are assumed to follow paths which are themselves normal to that surface. This assumption is valid except for those factors discussed separately in Sections II.5 and II.6. Consequently, as shown in Figure 1, if the storage surface were a plane, parallel to the photocathode, dimensional integrity would be preserved in mapping the photocathode image onto the storage surface ($L_{\text{photocathode}} = L_{\text{storage tape}}$). However, the curved storage surface results in a "stretching" of the image in the direction of the curvature ($L_{\text{photocathode}} \rightarrow D_{\text{storage tape}}$). In the case where the camera is operated in an integrating mode (i.e., panoramic scan) the tangential velocity of the drum is matched to the apparent velocity of the object being observed. Under these conditions, this stretching will be observed as a smearing of the image in the direction of the drum curvature.

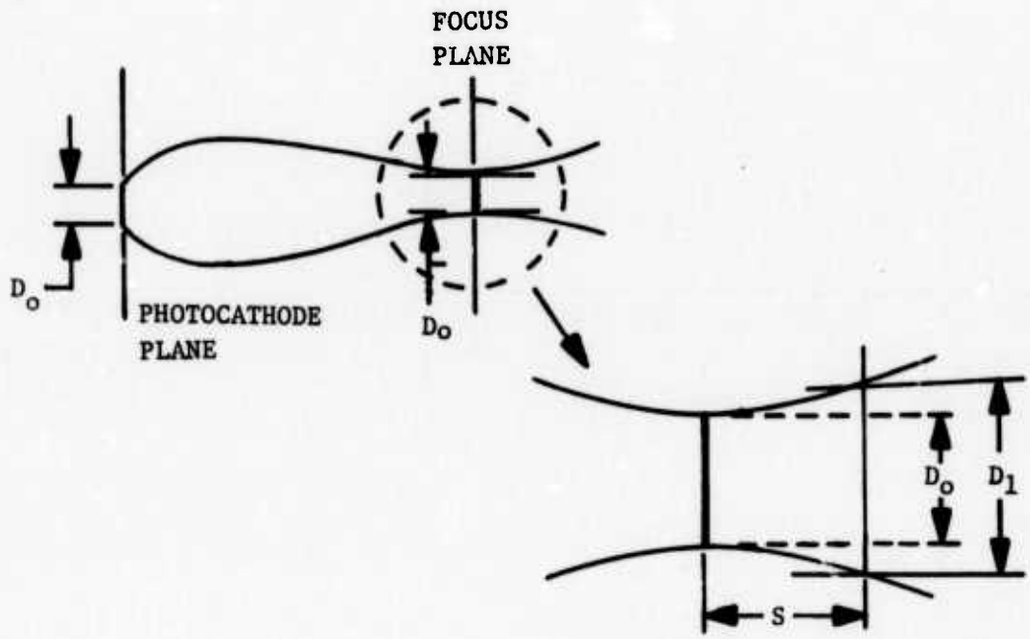

S= SAGITTAL DISTANCE

D_1-D_o= INCREASE IN BUNDLE SIZE

Figure 2. DEFOCUSING DUE TO SAGITTAL ERROR

II.4. SAGITTAL DISTANCE OF DRUM

(U) In an electromagnetic image section, the magnetic field strength and length of the image section length are selected so that the photoelectrons complete an integral number of helical paths in going from the photocathode to the storage surface during their transit time. However, in a drum camera, the length of the image section varies over the format as a result of the sagittal distance of the drum. Consequently, while focus can be achieved in parts of the format, a slightly defocussed image will exist in other parts of the format. Figure 2 illustrates the case where the image is a blur circle resulting from a point object. As shown in this figure, the photoelectron bundle having a diameter 'D_o' at the photocathode will have the same diameter 'D_o' at the focus plane. However, as the image section length increases due to the sagittal distance 'S', the diameter of the electron bundle will increase D_o to D_1.

II.5. BENDING OF THE ELECTRIC FIELD IN THE DRUM REGION

(U) In the previous sections, the assumption has been made that the electric and magnetic fields are both parallel to the optical axis of the camera. While this is true for a uniform magnetic field, it is not true for the electric field in the region of the drum. Since the primed storage tape forms an equipotential surface, the electric field just above the tape surface will be normal to that surface. Consequently, near the drum surface the electric field will bend towards the optical axis as shown in Figure 3. This, in turn, will cause a bending of the photoelectron paths towards the optical

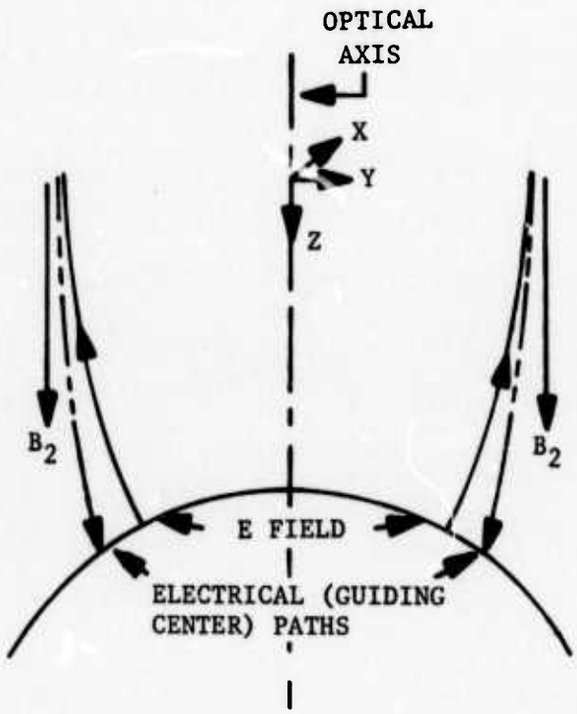

Figure 3 ELECTROSTATIC FIELD DISTORTION

axis. That is, the velocity '$\vec{v}$' acquired by the photoelectrons as a result of the electric field components parallel to the y-axis is also parallel to the y-axis (i.e. $\vec{v} \rightarrow v_y$ and $-v_y$). In the presence of the magnetic field B, this velocity results in an additional Lorentz force ($-e\vec{v} \times \vec{B}$) acting on the photoelectrons. This additional force has the effect of increasing the radii of the helixes being described by the electrons and at the same time imparting a drift velocity to the guiding center of each helical path. This drift velocity is perpendicular to the YZ plane.

(U) This bending of the electric field and its subsequent effect on the photoelectron paths is greatest at the edges of the format width and reaches a minimum at the optical axis. The degree of image distortion is thus a function of position within the format. In the case where the camera is operated in an integrating mode, this distortion will also have a smearing effect on the image.

II.6. NON-UNIFORM MAGNETIC FIELD

(U) All of the factors causing image distortion and degradation which have so far been discussed have resulted from imaging onto a curved surface. Another important factor that will exist in any type of camera utilizing an electromagnetic image section is magnetic field non-uniformity. Since the divergence of the magnetic field must be zero, variations in the strength of the magnetic field parallel to the optical axis (B_z in Figure 3) are

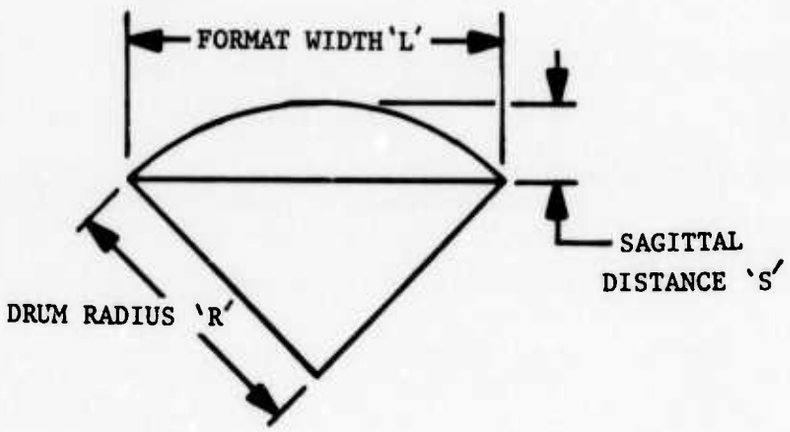

$$R = \frac{4S^2 + L^2}{8S}$$

Figure 4. SAGITTAL ERROR CALCULATION

accompanied by magnetic field gradients in the XY plane. These gradients act as a magnetic lens, and as a result, photoelectrons in different locations in the image section are deflected in different amounts. This results in additional image distortion, and, in the case of a camera operated in an integrating mode, additional smear.

II.7. METHOD OF ANALYSIS AND FORMAT LIMITATIONS

(U) In this study, an analysis was conducted on the factors described in Sections II.3 through II.5 to determine the extent that each factor would distort and degrade the image. In this analysis, a format width of 0.79 inches, corresponding to a slit width of 1 degree and an optical focal length of 45 inches, was selected. In addition, the drum radius was fixed by requiring that the sagittal distance due to the drum be less than or equal to 0.010 inches over the format width. This part of the analysis is also applicable to a tape transport camera, since tape flexures of up to 0.010 inches might be expected. From the trigonometric relationship given in Figure 4, sagittal distance requirement corresponds to a minimum drum radius of about 8 inches.

II.8. IMAGE SECTION PARAMETERS

An image section length of about 9 cm has been selected on the basis of voltage gradient considerations. For optimum storage tape performance, the required photoelectron landing energy is expected to be 15 KeV.

The required strength of the image section magnetic field for single-loop focus can be calculated from

$$B = \frac{\pi}{L'} \frac{(2mV)^{1/2}}{e}, \qquad (1)$$

where

B = magnetic field strength

L' = image section length

V = potential difference between photocathode and storage tape

m = electron mass

e = electronic charge

This results in a required field strength of approximately 150 gauss.

(U) The greatest amount of distortion resulting from each of the factors discussed in Sections II.3 through II.5 occurs at the extremes of the format width. Consequently, the following analyses concentrate on determining the magnitude of the image distortion in these areas.

II.9. ANALYSIS OF THE IMAGE DISTORTIONS RESULTING FROM MAPPING A PLANE SURFACE ONTO A CYLINDRICAL SURFACE

(U) As discussed in Section II.3, mapping a plane photocathode surface onto a cylindrical storage drum results in a stretching of the image in the direction of the drum curvature. Thus, this analysis consists of determining the difference between the format width at the photocathode (L), and the

format width on the curved storage surface (D). Figure 5 shows the mapping geometry and the resulting trigonometric relationships.

Thus,

$$D = \frac{\pi R}{90} \arcsin (L/2R)$$

$$\boxed{D - L = \frac{\pi R}{90} \arcsin (L/2R) - L} \qquad (2)$$

Using R = 8 inches and L = 0.79 inches,

$$D - L = 3.21 \times 10^{-4} \text{ inches}$$

$$= 8.2 \text{ microns}$$

(U) Thus the image from the photocathode will be stretched by up to 8.2 microns when it is mapped onto the drum surface. In the case where the camera is operated in an integrating mode, the entire photocathode image will experience an 8.2 micron smear in the direction of the drum curvature.

II.10. ANALYSIS OF THE IMAGE DEGRADATION RESULTING FROM THE CURVATURE OF THE DRUM

(U) As discussed in Section II.3, the photoelectrons not exiting normal to the photocathode will describe helical paths in going from the photocathode to the storage surface. The image section length and magnetic field strength are selected such that these electrons will complete a single loop during the transit time (Section II.7). However, in those areas where the added sagittal distance effectively increases the image section length, the electrons begin a second loop. The purpose of this analysis is to determine the extent to which this results in a defocused image.

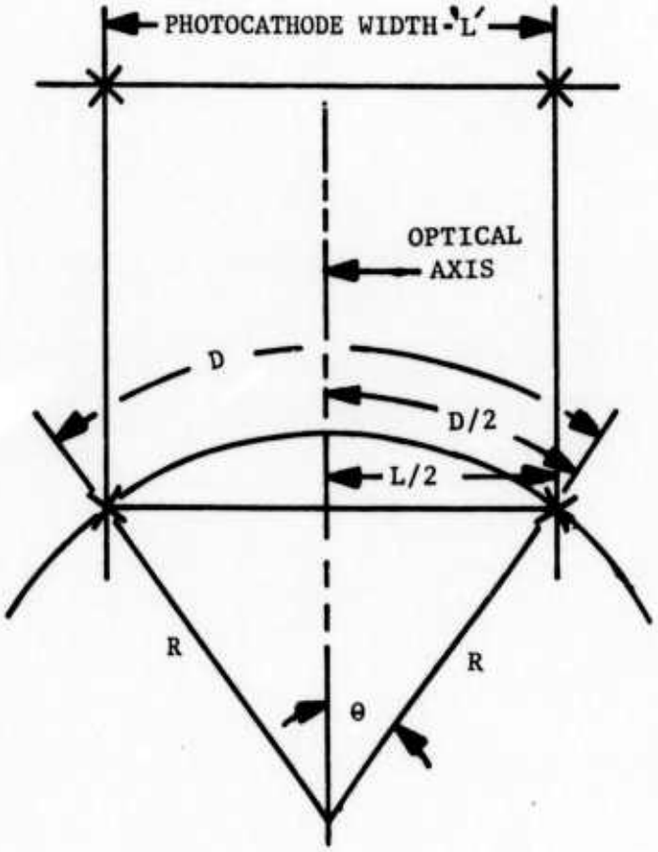

Figure 5. MAPPING ERROR ANALYSIS

(U) For this analysis, a set of worst-case conditions have been selected and applied to the case where the electron image at both the photocathode and the focus plane of the drum is an electron bundle of diameter D_o [resulting from an optical blur circle of diameter D_o being imaged onto the photocathode].

(U) These worst-case conditions are the following:

A. The photoelectrons are assumed to exit <u>parallel</u> to the photocathode with an initial energy (in that direction) of 0.5 eV (the peak of typical photoelectron energy curves occurs at ~0.2 eV when using a 2870°K incandescent source).

*B. The initial velocities of these photoelectrons are assumed to be from the blur circle.

*NOTE: 'B' is a worst-case condition only if the electrons complete only a small fraction of their second helix during the time required to transit the sagittal distance. However, this will be established by the end of the analysis.

(U) As a result of condition 'A', these electrons have a velocity component '$v_\perp$' in the plane perpendicular to the optical axis with a magnitude of $4.2 \times 10^{+7}$ cm/sec.

$$\text{i.e. } v_\perp = \left(\frac{2E}{m}\right)^{1/2} = 4.2 \times 10^{+7} \text{ cm/sec} \qquad (3)$$

where

E = electron energy

m = electron mass

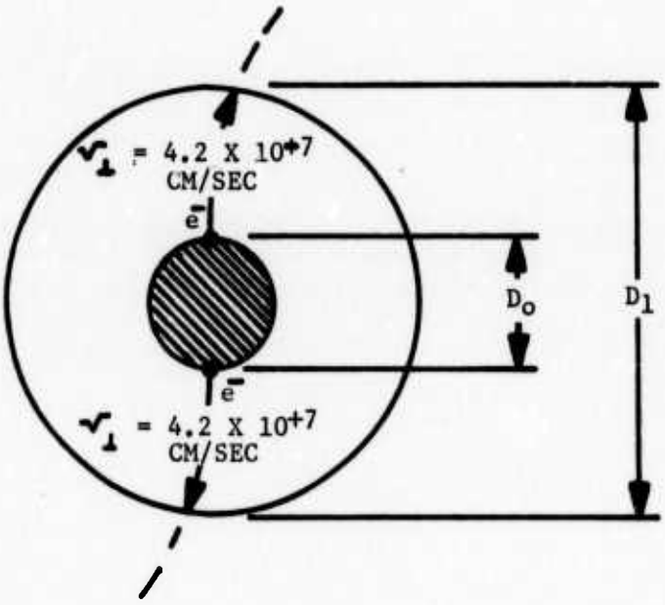

Figure 6. ELECTRON MOTION DURING ADDED SAGITTAL DISTANCE

(U) Since the Lorentz force resulting from the magnetic field is perpendicular to this velocity component, the magnitude of '$v_{\perp}$' does not change as the electrons are accelerated from the photocathode to the storage tape. Consequently at the focus plane of the drum, '$v_{\perp}$' is still $4.2 \times 10^{+7}$ cm/sec. In addition, condition 'B' also exists at the focus plane.

(U) Figure 6 shows the paths that two such photoelectrons on the circumference of the blur circle will take in the plane perpendicular to the optical axis during the time required to transit the added sagittal distance.

(U) The increase in the size of the electron bundle ($D_1 - D_o$) is simply twice the distance traveled by one of these electrons (in this plane) during the time t_s required to transit the sagittal distance.

$$\text{i.e., } \Delta D - D_1 - D_o = 2v_{\perp} t_s \qquad (4)$$

(U) Since the landing energy of these photoelectrons was selected to be 15 KeV, their velocity '$v_{//}$' parallel to the optical axis in vicinity of the drum is approximately $7.3 \times 10^{+9}$ cm/sec using equation (3) above. The time 't_s' required to transit the 0.010 inch (2.5×10^{-2} cm) sagittal distance 'S' can thus be calculated:

$$t_s = \frac{S}{v_{//}} = 3.48 \times 10^{-12} \text{ sec} \qquad (5)$$

Substituting back into equation (4) results in

$$\Delta D = 2(4.2 \times 10^{+7})\ (3.48 \times 10^{-12})$$

$$= 2.9 \times 10^{-4} \text{ cm}$$

$$= 2.9 \text{ microns}$$

(U) It should be noted that this value for D can be reduced by a factor of 2 by selecting the focus plane to be 0.050 inches below the "top" of the drum. In that case, an effective sagittal distance of $\pm$ 0.005 inches exists which will result in a D of approximately 1.45 microns - both in the center of the format and at the edges of the format width.

(U) The amount of electron travel in the record helix during the transit of the sagittal distance will now be calculated. The radius, R, of the helix can be calculated using the expression

$$R = \frac{mv_{\perp}}{eB} \qquad (6)$$

where

m = electron mass

e = electronic charge

B = magnetic field strength

(U) Using 100 gauss for the magnetic field strength results in a radius of 2.39×10^{-2} cm or 239 microns.

(U) Consequently, the distance that each electron travels in the plane perpendicular to the optical axis during one loop of the helix is 1503 microns ($2\pi R$). Therefore, since the electrons in this analysis only travel (0.0019) (2.9 microns/1503 microns) of their second helix during the time required to transit the sagittal distance, condition B can be considered a "worst-case" condition.

II.11. ANALYSIS OF IMAGE DISTORTION RESULTING FROM BENDING OF THE ELECTRIC FIELD IN THE DRUM REGION

(U) As described in Section II.5, the bending of the electric field in the drum region results in an initial bending of the photoelectron toward the optical axis. In the presence of the magnetic field, the added velocity associated with this bending results in an additional Lorentz force acting on the photoelectrons.

(U) In general, the motion of an electron under these conditions can be described by the following differential equations. The coordinate system is illustrated in Figure 7.

$$\frac{d^2x}{dt^2} = \frac{-eB_s}{m} \frac{dy}{dt} \tag{7}$$

$$\frac{d^2y}{dt^2} = \frac{-eE_y}{m} + \frac{eB_z}{m} \frac{dx}{dt} \tag{8}$$

$$\frac{d^2z}{dt^2} = z - \frac{eE_z}{m} \tag{9}$$

$$x = x^o + \underbrace{\frac{mv_y^o}{eB_z}\left[\cos\left(\frac{eB_z t}{m}\right) - 1\right] + \frac{mv_x^o}{eB_z}\sin\left(\frac{eB_z t}{m}\right)}_{*} - \frac{mE_y}{eB_z^2}\sin\left(\frac{eB_2 t}{m}\right) + \frac{E_y t}{B_z} \tag{10}$$

$$y = y^o + \underbrace{\frac{mv_y^o}{eB_z}\sin\left(\frac{eB_2 t}{m}\right) + \frac{mv_x^o}{eB_z}\left[1 - \cos\left(\frac{eB_z t}{m}\right)\right]}_{*} + \frac{mE_y}{eB_z^2}\left[\cos\frac{eB_z t}{m} - 1\right] \tag{11}$$

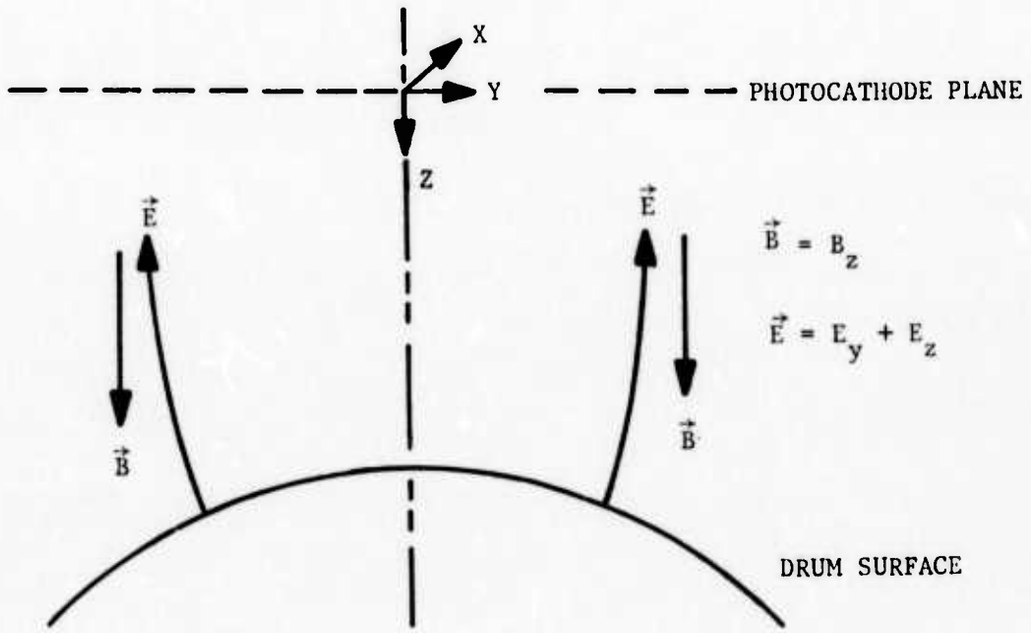

Figure 7. ELECTROSTATIC AND MAGNETIC FIELD GEOMETRY

$$z = \underbrace{z^{o} + v_z{}^{o} t - \frac{eE_z t^2}{2m}}_{*} \qquad (12)$$

(U) In these equations, x^o, y^o and z^o define the position of the electron at time 't' = 0 and $v_x{}^o$, $v_y{}^o$ define the velocity of the electron at t = 0.

(U) The portions of equations 10, 11 and 12 that are marked with an asterisk describe the behavior of the electron when both the electric and magnetic fields are parallel to the optical axis (i.e., $\vec{E} \rightarrow E_z$, $\vec{B} \rightarrow B_z$). As discussed in Section II.7, the values of $\vec{E}$ and $\vec{B}$ were selected such that at the focus plane of the drum, $x = x_o$ and $y = y_o$ at the single-loop focus point. Therefore, if the assumption is made that the magnitude of E_z does not significantly change as a result of the field curvature towards the optical axis, the extent of the distortion can be established by determining the magnitudes of the remaining terms in equations (10) and (11) as shown below.

$$\Delta x = -\frac{mE_y}{eB_z{}^2} \sin\left(\frac{eB_z t}{m}\right) + \frac{E_y t}{B_z} \qquad (13)$$

$$\Delta y = +\frac{mE_y}{eB_z{}^2}\left[\cos\left(\frac{eB_z t}{m}\right) - 1\right] \qquad (14)$$

(The assumption that the magnitude of E_z does not change significantly is valid provided that the angle between the electric field and the z axis remains small. This will be verified later.)

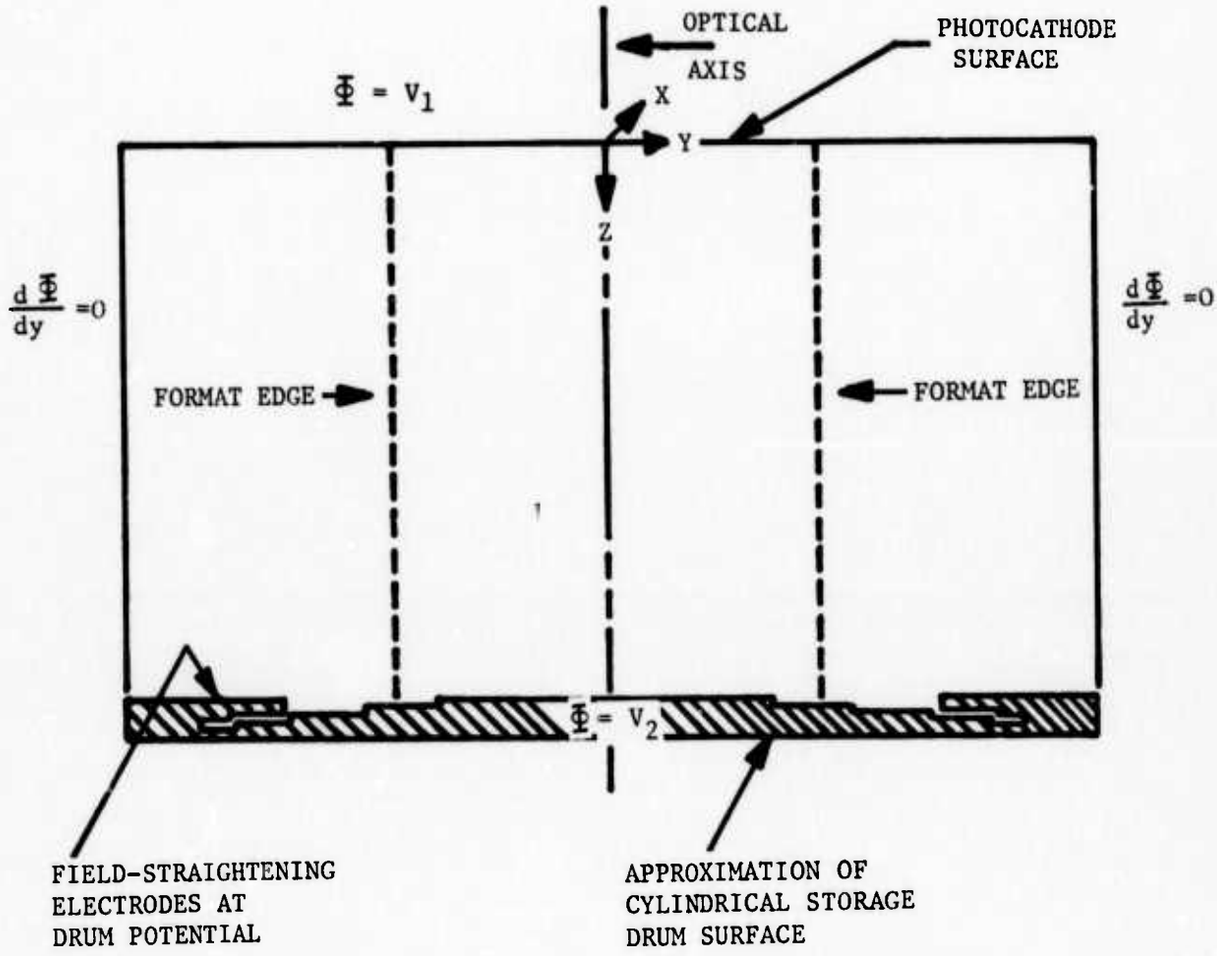

Figure 8. BOUNDARIES INPUTED TO COMPUTER PROGRAM

(U) To determine the magnitude of E_y as a function of location within the image section, the potentials at various points within the image section have been determined by an iterative computer solution of the Laplace equation. The boundary conditions that approximate the actual image section geometry, but also fall on a square numerical mesh were selected and are shown in Figure 8.

(U) The computer program prints out potential values on a square array of points 0.2 mm apart. From this array of potentials, the magnitude and direction of the electric field in any region of interest can be determined. Calculations indicate that the electric field at the edge of the format can be characterized in the following way:

1. The electric field begins bending toward the optical axis at a point approximately 1.5 cm above the drum surface.

2. In the region between the drum surface and the point where the field first begins bending, the average electric field '$\vec{E}_{Ave}$' (as defined in Figure 9) makes an angle of 0 degrees, 34 minutes with the z-axis. This confirms the assumption that E_z does not change significantly in value as a result of the field bending toward the optical axis.

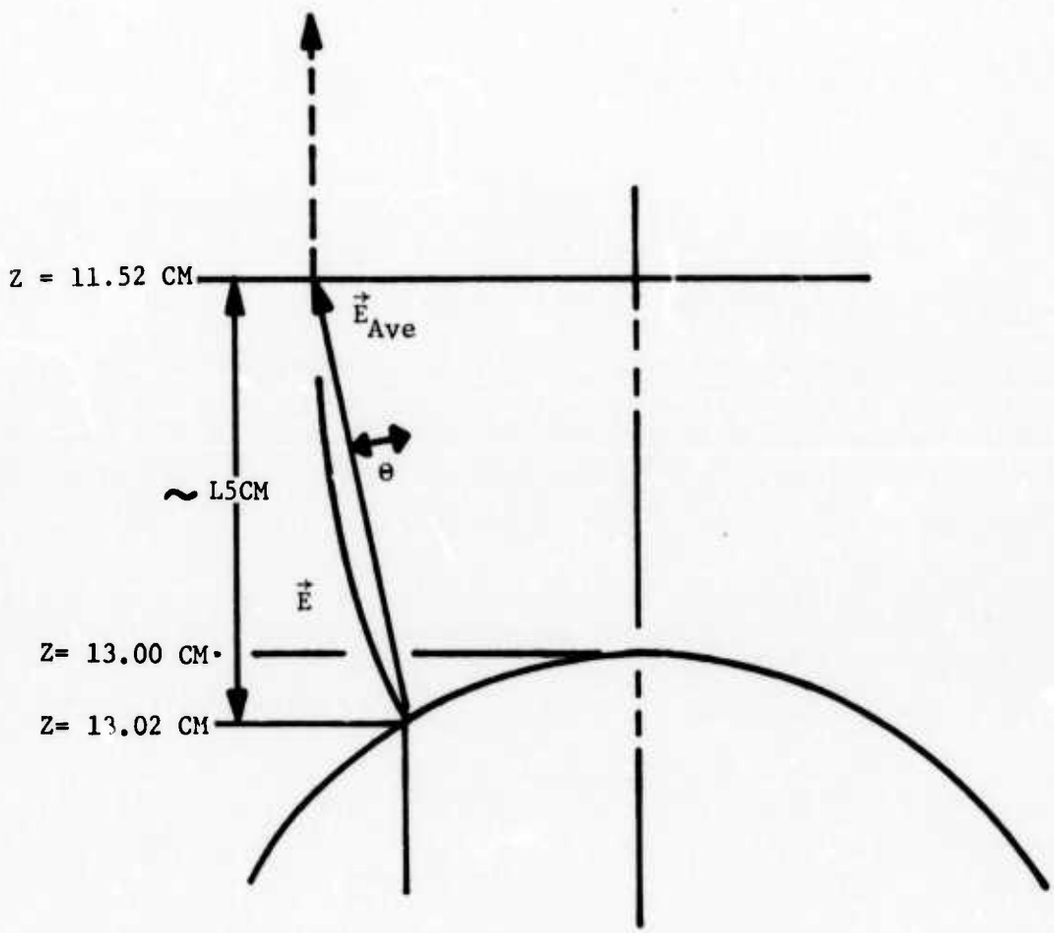

Figure 9. ELECTRIC FIELD DISTORTION

(U) The extent of the distortion due to the field curvature can now be calculated using equations (13) and (14). The average value of E_y associated with E_{Ave} was used for these calculations as shown below.

$$E_{y_{Ave}} = E_{Ave} \tan 34'$$

where

$$E_{Ave} = 1.15 \times 10^{+11} \text{ abvolts/cm}$$

Thus, $$E_{y_{Ave}} = (\pm)\ 1.14 \times 10^{+9} \text{ abvolts/cm}$$

(U) The sign of $E_{y_{Ave}}$ designates which edge of the format width is being considered.

(U) This $E_{y_{Ave}}$ acts on the electrons during the time required for them to transit the last 1.5 centimeters of the image section. This transit time has been calculated to be approximately 2.13×10^{-10} seconds.

(U) Using these values for $E_{y_{Ave}}$ and the transit time equations (13) and (14) have been used to calculate the amount of distortion at the edge of the format resulting from the bending of the electric field. The results of the calculations are as follows:

$x = +0.6$ microns (for $y_o > 0$)

$x = -0.6$ microns (for $y_o < 0$)

$y = -4.5$ microns (for $y_o > 0$)

$y = +4.5$ microns (for $y_o < 0$)

(U) As in the cases of the other distortions analyzed, the magnitudes of Δx and Δy decrease nearer the optical axis, except in the case where the drum surface is moved closer to reduce the distortion at the edge of the format as discussed in Section II.10.

(U) It should be noted that Δy distortion due to this bending of the electric field is opposite in direction to the Δy distortion caused by mapping the plane photocathode surface onto the curved drum surface as shown in Section II.9. Thus, these two distortions tend to cancel each other.

(U) The net magnitudes (at the edge of the format) of the distortions discussed in Sections II.9 through II.11 are summarized in the table below:

Cause of Distortion	Magnitude	Direction
Spot Growth	1.45 microns	radial
Mapping and Field Bending Combined	- 0.6 microns ($y < 0$)	x-direction
	+ 0.6 microns ($y > 0$)	x-direction
	+ 0.4 microns ($y < 0$)	y-direction
	- 0.4 microns ($y > 0$)	y-direction

(U) In the case where the camera is operated in an integrating mode and the electron image at the photocathode is an electron bundle of diameter D_o, the total effect of all these distortions will be to:

1. Increase D_o to D_o + 2.65 microns along the x axis, and
2. Increase D_o to D_o + 2.25 microns along the y axis.

APPENDIX III

STORAGE TARGET ANALYSIS

TABLE OF CONTENTS

LIST OF ILLUSTRATIONS

LIST OF TABLES

APPENDIX III

STORAGE TARGET ANALYSIS

III.1 INTRODUCTION

(U) Study effort has been directed towards determining whether or not the format size and electrical discharge sensitivity (drop in surface potential per unit of input photoelectron charge density) of the presently-available storage targets can be increased to the level required by a Teal Amber tape transport camera with unity image section magnification. The transport design necessitates a stainless steel foil tape 110 mm wide and 1.2 m long covered with a Silicon Dioxide film. The electrical discharge sensitivity required is anticipated to be on the order of 10^{+11} volt-cm^2/coulomb. The largest stainless steel foil storage targets presently being fabricated by CBS Laboratories are 76 mm wide and 510 mm long, with an electrical discharge sensitivity of approximately $5 \times 10^{+9}$ volt-cm^2/coulomb. Thus, a threefold increase in area and a twentyfold increase in sensitivity over the present targets are necessary for the Teal Amber application.

(U) From the Table I it can be seen that the highest experimentally verified sensitivity achieved in the current program was 6.4×10^{10} volt-cm^2/coulomb. This is a 13-fold increase over that of the present targets. Although this is not sufficient for a unity magnification image section, it can be employed in conjunction with a framing camera demagnifying image section to provide more than adequate sensitivity for the Teal Amber application. The target size required for a framing camera is also easier to fabricate than the large area surface required for a tape storage camera.

TABLE I

SUMMARY OF INITIAL WRITE-IN CHARACTERISTIC MEASUREMENTS

Film Thickness	Initial Prime Voltage	Landing Energy	Input Charge Density (Q_{in})	Change in Surface Potential (ΔV)	Electrical Discharge Sensitivity ($\Delta V/Q_{in}$)
7,200 Å	-205V	10 kev	5×10^{-10} coul/cm^2	16V	$3.2 \times 10^{+10}$ $\frac{\text{volt-cm}^2}{\text{coulomb}}$
9,700 Å	-293V	13 kev	5×10^{-10} coul/cm^2	23V	$4.6 \times 10^{+10}$ $\frac{\text{volt-cm}^2}{\text{coulomb}}$
13,500 Å	-409V	16 kev	5×10^{-10} coul/cm^2	32V	$6.4 \times 10^{+10}$ $\frac{\text{volt-cm}^2}{\text{coulomb}}$

III.2 STORAGE TARGET FABRICATION

(U) The storage target fabrication process involves three operations: cleaning; firing; and coating the stainless steel target substrate. In order to fabricate larger targets, the fixtures which support the target substrate during these operatings have to be changed. Experiments have been performed with the sputtering system used for coating the tape substrates, but only conceptual studies of the revised cleaning and firing processes have been made, since the proper fixtures were not available.

III.2.1 Cleaning and Firing of Target Substrates

(U) Storage target substrates of stainless steel foil up to 800 mm long have been cleaned and fired using the current support fixture, a cylinder approximately 10" in diameter and 2" high made of a molybdenum wire screen. The stainless steel foil is wrapped once around the screen cylinder and tack-welded in place. The foil and supporting screen subsequently undergo both cleaning and firing operations together.

(U) The volume occupied by the foil and support fixture is limited to a cube 10 inches on a side, representing the inside dimensions of the furnace. In addition to the space requirement, other considerations include: ease of loading and removing the substrate to avoid dents and scratches; no two areas of foil to be in contact in order to avoid welding; and minimum contact between the foil and support in order to avoid uncleaned areas. It has been found from experience that the firing process induces a permanent set according to the curvature of the foil during the firing.

(U) Based on these limitations, the best method of supporting the Teal Amber tape appears to be a spiral configuration with space between adjacent wraps.

III.2.2 Target Substrate Coating Process

(U) The storage target substrates are coated with SiO_2 using a radial rf sputtering system. Stainless steel substrate foils up to about 750 mm long are presently being coated. The foil is formed against the inside of an 8-inch diameter pyrex cylinder and spot-welded together. The foil and pyrex cylinder assembly is then placed within the sputtering system concentric to the quartz electrode. Coating the substrate with SiO_2 to a thickness of 2300 Å takes approximately three hours. In order to accommodate a substrate foil 1.2 m long, the foil must be located against the inside of the pyrex vacuum jar (1.4 m perimeter) used to enclose the sputtering system.

(U) An experiment has been performed to establish whether storage targets coated at the inner surface of the pyrex vacuum jar are equivalent to those coated on the present fixture. For this experiment, a substrate foil about 750 mm long was fabricated using the standard cleaning and firing processes. The substrate was then located on the inside surface of the pyrex vacuum jar and coated to the standard 2300 Å SiO_2 thickness. The resulting coating appeared very uniform over the tape surface. EBIC gain was comparable to that of the standard storage targets (approximately 90), but the charge storage was not as good. It ranged from a 2-volt to a 17-volt drop as opposed to a maximum 2-volt drop in the present targets. However, the results of this experiment clearly demonstrate the feasibility of preparing storage targets with the larger format.

III.3 STORAGE TARGET EVALUATION

(U) In addition to the storage target fabrication development activities, the electrical characteristics of the standard format storage targets having

various SiO_2 film thicknesses were investigated to determine the optimum thickness range for a subsequent camera hardware program. Film thicknesses of 7200 Å, 9700 Å, 13,500 Å and 17,000 Å were investigated. These tapes were fabricated using the same procedures and processes as for the present targets having a 2000 Å film thickness.

(U) An attempt was made to heat the tape samples to 385°C (under vacuum) for a period of approximately 16 hours to simulate the thermal cycles in the camera tube processing schedule. At this temperature, a good vacuum (1×10^{-6} torr) was achieved using a relatively high-speed diffusion pump. However, extensive outgassing was observed at temperatures greater than 300°C when using an ion pump vacuum system with a considerably lower pumping speed. Consequently, in those thermal cycles where the smaller ion pump system was used, the temperature was limited to about 275°C. The exact temperatures for the tape samples in the specific tests are specified in the discussion of each test.

(U) At the conclusion of the test effort, the thermal cycling was accomplished using a second ion pump system equipped with a residual gas analyzer (RGA). No outgassing was observed in these runs, nor were any unusual peaks noted on the RGA traces. This suggests that the previously-observed outgassing was not from the tape samples but was due to a contaminated ion pump.

(U) The following electrical characteristics of the storage targets were evaluated:

1. DC EBIC Gain - The electron-bombardment-induced conductivity exhibited by the storage target when exposed to a steady state (dc) high-energy electron beam and a low-energy surface potential stabilization beam.

TABLE II

OPTIMUM LANDING ENERGIES

Storage Target Film Thickness (Angstroms)	Landing Energy for Peak dc EBIC Gain
7,200	10 kev
9,700	13 kev
13,500	16 kev
17,000	19 kev

2. Write-in Characteristic - The relationship between a given high-energy input charge density and the resultant change in surface potential of a primed storage target.

3. Charge storage - The ability of the storage target to retain a surface charge as demonstrated by the surface potential vs. time characteristic.

III.3.1 DC EBIC Gain Measurements

(U) Samples from each of the four storage target tapes were thermally cycled at 385°C for approximately 16 hours. They were subsequently mounted on holders and placed in a vacuum system for dc EBIC gain measurements.

(U) In making these measurements, however, a high leakage current from the potential stabilization gun was observed in the target circuit which tended to mask the EBIC gain current. Due to the existence of this high leakage current, it was doubtful that the surface potentials of the samples were in fact being stabilized at grid potential. Consequently, these dc gain measurements were only used to identify the location of peaks in the dc gain vs. landing energy curves for each of the tapes. The landing energy associated with each of these peaks is presented in Table II.

III.3.2 Write-In Characteristic Measurements

(U) Samples from each of the four storage target tapes were thermally cycled at 250°C for about 22 hours and mounted on the drum of the write-in characteristic test fixture. Write-in characteristic measurements were made on all of the tapes shown in Table II except the 17,000 Å tape, due to difficulties in priming that tape to the proper level. Table I summarizes the results of these measurements.

(U) An effort was also made to obtain write-in characteristic data at lower input charge densities, (down to 9×10^{-11} coul/cm^2), although it was difficult to obtain a good writing beam spot at the required beam current levels. It was felt that the poor spot geometry resulted in a non-uniform deposition of charge from the writing beam which, in turn, affected the shape of the write-in characteristic curve in that region.

(U) When the test samples were removed from the evaluation system, it was observed that each sample had blotches on the surface. Later tests indicated that these spots were the result of contaminants present on the substrates prior to depositing the SiO_2 coating.

III.3.3 Additional Write-In Characteristic Measurements

(U) Due to the difficulties experienced in making write-in characteristic measurements at the lower input charge densities, some modifications were made to both the write-in characteristic evaluation system and to the test procedure in an effort to improve the accuracy of these measurements. Write-in characteristic measurements were made on a second 7200 Å target sample for an initial prime level of -206 volts and for input charge densities

in the range of 2.7×10^{-11} coul/cm^2 to 1.27×10^{-9} coul/cm^2. Next, the effect of increasing the prime level to -312 volts investigated. Finally, a recheck of the write-in characteristic at the -206 volt prime level was made. After making these measurements, the sample was removed from the evaluation system. A visual inspection of the sample showed that this sample had also acquired spots and blotches on its surface.

(U) The results of these measurements are presented in Figure 1 and can be summarized as follows:

1. The relationship between input charge density and the resultant change in surface potential is approximately linear over the range of input charge densities investigated.

2. The slope of this curve represents the electrical discharge sensitivity, and is approximately

$$3.3 \times 10^{+10} \frac{\text{volt-cm}^2}{\text{coulomb}}$$

for the -206 volt initial prime level.

3. This slope increased from 17% to 31% in going from the -206 volt to the -312 volt initial prime level.

4. The uncertainty in the amount of increase in this slope is due to an apparent "aging" process; that is, the slope of the -206 volt (repeated) curve is 11% less than the slope associated with the data obtained at the original -206 volt prime. The extent of this aging process and its causes, such as time, electrical stress, or electron bombardment, have yet to be determined.

(U) Subsequently, a target sample from an additional tape also having a 7500 Å film was installed in the evaluation system. This second tape had been fabricated using a different stainless steel substrate and a different substrate preparation procedure. Write-in characteristic measurements were made on this sample for a number of different initial prime levels and also

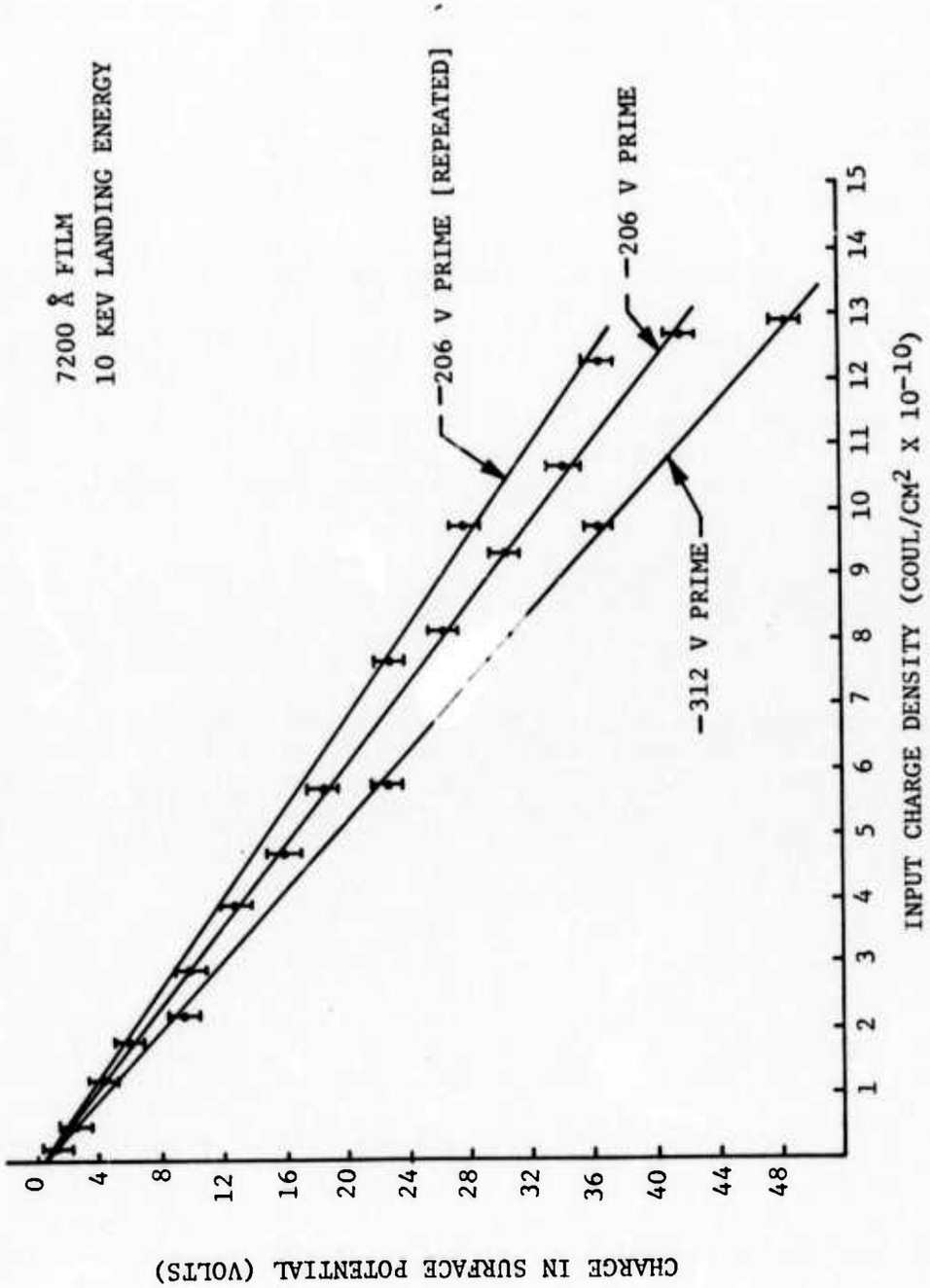

FIGURE 1. STORAGE TAPE WRITE-IN CHARACTERISTICS

a number of different writing beam landing energies. The data obtained are presented in Figure 2. The following observations were made:

1. The slope of the write-in characteristics curve has its peak value when the landing energy of the writing beam is approximately 7 kev. This fact appears to contradict the early dc EBIC gain measurements on the 7200 Å tape that showed that the gain peaked at 10 kev.

2. As a function of target priming level, the slope of the write-in characteristic curve appears to peak (or saturate) somewhat between -410 V and -510 V.

(U) After taking the data presented in Figure 2, the write-in characteristic of the target at the -205 V prime level and 9 kev landing energy was remeasured to check for possible target aging. No such effect was observed. In addition, no spots or blotches were observed on the surface of the tape after taking the above data. It was, therefore, concluded that the spots observed on the previous target samples were the result of contaminants present on the substrates prior to depositing the SiO_2.

III.3.4 Charge Storage Measurements

(U) While the main goal of the target evaluation work was to determine the write-in characteristics of the storage target tapes, charge storage measurements were also made on several of the tapes. The change in surface potential as a function of time was used to measure the charge storage ability. The results of these measurements are summarized in Table III. Since in the proposed camera the time between write-in and readout is on the order of one minute, these measured charge storage characteristics are more than satisfactory.

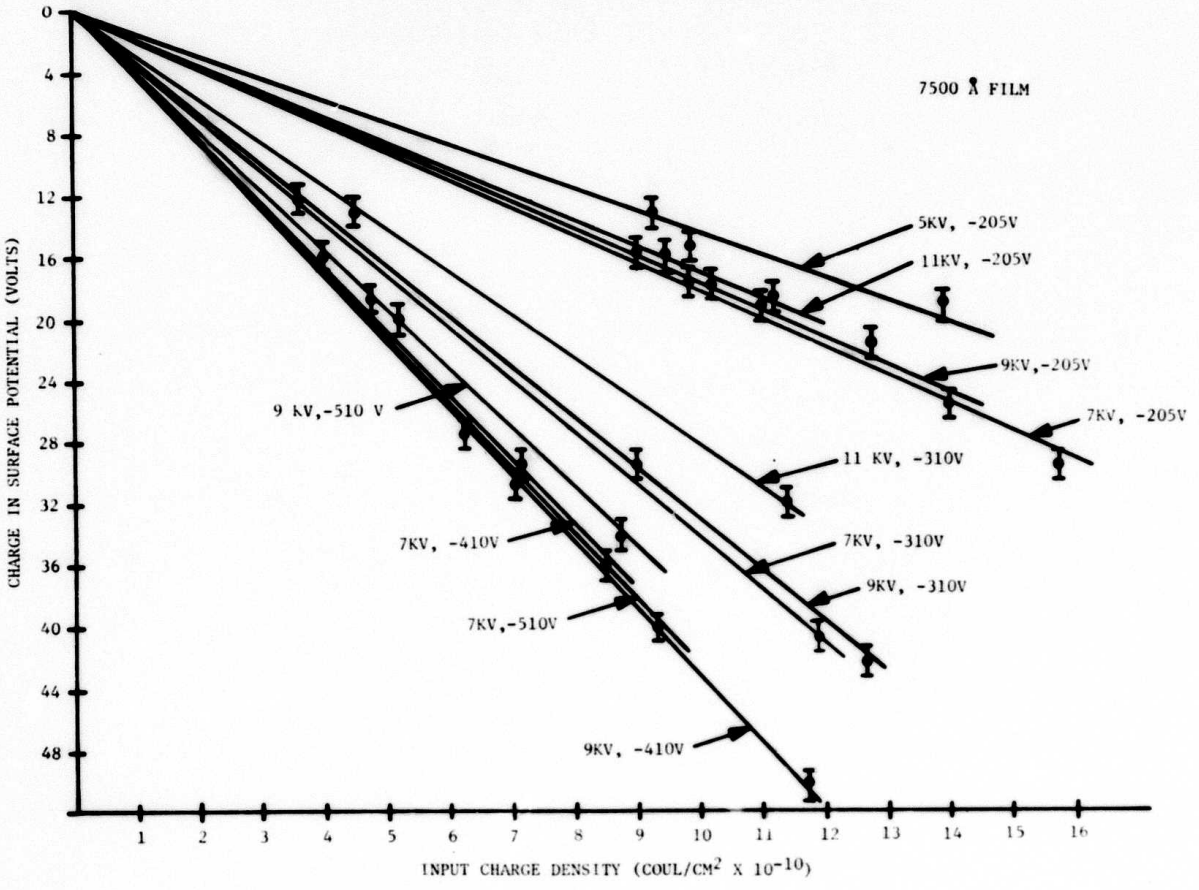

Figure 2. STORAGE TAPE WRITE-IN CHARACTERISTICS FOR TAPE USING ALTERNATE SUBSTRATE PREPARATION PROCEDURES

TABLE III

CHARGE STORAGE TEST RESULTS

Film Thickness	Initial Surface Potential	Storage Time	Change in Surface Potential During the Storage Time
7200	-213 Volts	16 hrs	6 Volts
7500	-210 Volts	23 hrs	4½ Volts
9700	-211 Volts	16 hrs	2½ Volts

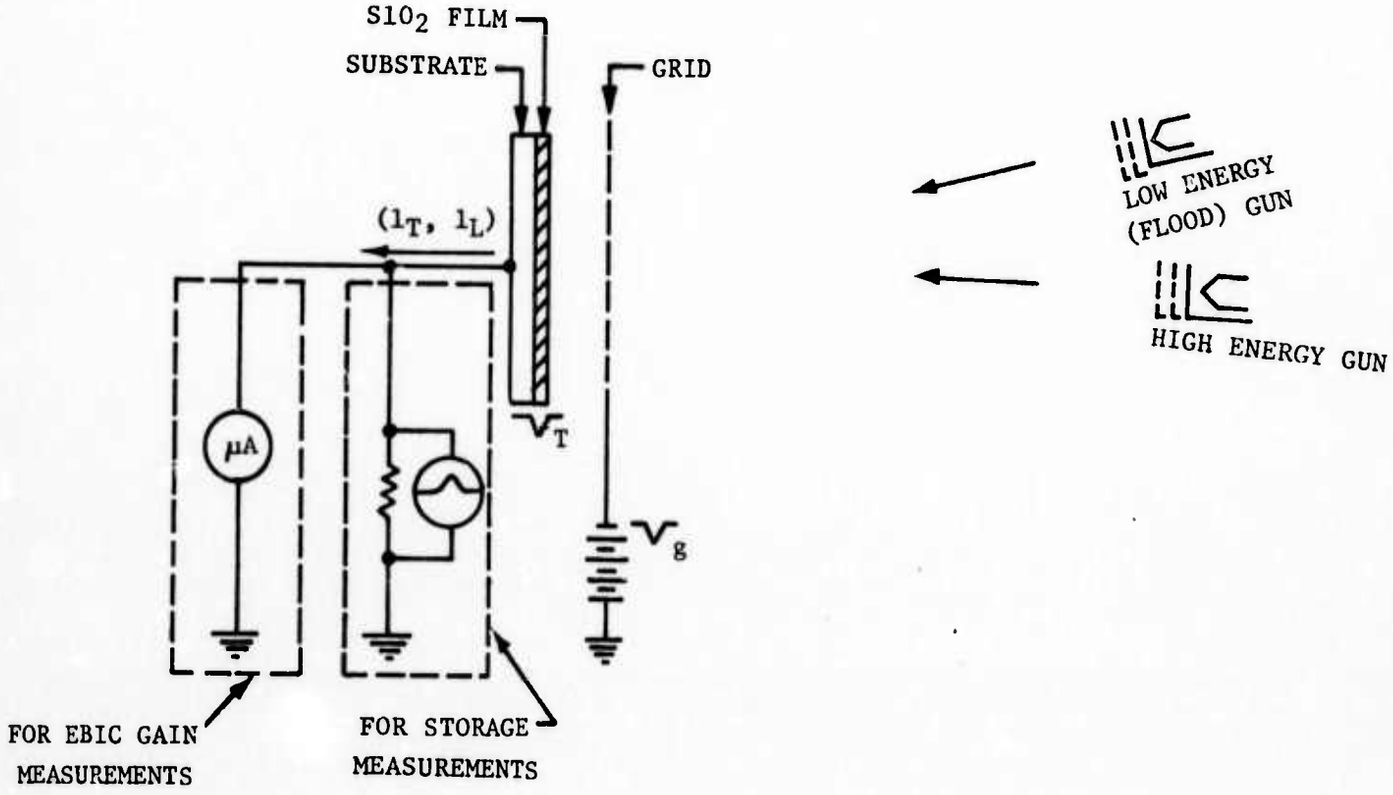

Figure 3. EXPERIMENTAL ARRANGEMENT EBIC GAIN AND STORAGE MEASUREMENTS

III.4 STORAGE TARGET MEASUREMENT TECHNIQUES

(U)

III.4.1 EBIC Gain Measurement Procedure

(U) EBIC gain measurements of the storage targets are made in a demountable vacuum system which can evaluate eight tape samples simultaneously. The measurement is made by first priming the target surface to the potential of the grid positioned in front of the sample by flooding the surface with electrons having an energy above the first secondary emission crossover for SiO_2 but below the threshold energy for EBIC gain.

(U) A second electron beam of known current I_B whose electron energy can be varied from 2.5 kev to 25 kev, is then focused on the sample. The current I_T through the sample is then measured. The flood beam remains on in order to maintain the proper surface potential. After I_T has been measured, the high energy beam is biased off and the leakage current I_L due to flood beam is measured. The EBIC gain (η) of the tape sample is then calculated using the formula

$$\eta = \frac{I_T - I_L}{I_B} \qquad (1)$$

The EBIC gains measured by this technique are estimated to be accurate to within $\pm 5\%$. A schematic diagram of the experimental apparatus is shown in Figure 3.

III.5 WRITE-IN CHARACTERISTIC MEASUREMENT PROCEDURE

(U) Write-in characteristic measurements on the storage target are made in a second demountable vacuum system, consisting of a rotatable drum on which the tape samples are mounted, a prime/erase gun, a high-energy writing gun

operated in a vertical line-scan mode, and a low-energy gun for making surface potential measurements. The measurement is made by first priming the sample to the desired potential using the prime/erase gun. Then, with the drum rotating, the high-energy writing gun (5 kev - 20 kev) operated in a line scan mode is used to incrementally discharge the tape sample. The current in the high-energy beam is measured during the discharge process in order to determine the charge density delivered to the samples. The surface potential of the sample is then measured as described previously, the sample is reprimed, and the procedure is repeated for other write-in charge densities.

III.6 CHARGE STORAGE CHARACTERISTIC MEASUREMENT PROCEDURE

(U) Charge storage measurements can be made using either the EBIC gain test apparatus or the write-in characteristic apparatus. A tape sample is first primed to the grid potential, and the surface potential is measured. After a number of hours, the surface potential is again measured. The difference in potential is a measure of the storage property of the target.

(U) To determine the value of the surface potential, the beam from a low-energy (300 eV - 800 eV) electron gun is pulsed on for 10 μsec and the resulting current passing through the sample is monitored on an oscilloscope. Since the energy of the electrons from this gun is above the first crossover for secondary electron emission from SiO_2, the potential difference between the grid and sample surface determines the direction of the current. Neglecting the energy distribution of the secondary electrons,

$$\text{for } |V_g| > |V_T|, \quad I_T = I_{LB} \tag{1}$$

$$|V_g| < |V_T|, \quad I_T = (1-\delta)\, I_{LB} \tag{2}$$

$$|V_g| = |V_T|, \quad I_T = 0 \tag{3}$$

Where:

V_g = grid potential,

V_T = target potential,

I_T = current through the target,

I_{LB} = low-energy beam current, (all potentials are negative with respect to ground).

(U) As a result, the surface potential of the tape sample can be determined by varying the grid voltage until the current through the sample drops to zero. Since the total charge delivered to the sample during a single 10 μsec pulse is very small - on the order to 10^{-11} coulombs - this measurement can be made without appreciably changing the surface potential. This measurement is estimated to be accurate to within ± 0.25 volts.

APPENDIX IV

CBS ELECTROSTATIC CAMERA

ANALYTICAL MODEL

TABLE OF CONTENTS

APPENDIX IV

CBS ELECTROSTATIC CAMERA

ANALYTICAL MODEL

IV.1. INTRODUCTION

(U) An analytical signal-to-noise model has been developed for the CBS electrostatic camera that takes into consideration both internal and externally-generated noise sources and MTFs [1]. The following version of the model is specifically tailored for the star magnitude inputs of the Teal Amber I Design Study, but the signal and noise expressions are unchanged.

The description of the model will start with the various MTF terms, and then continue with the input parameters, the signal term and the noise terms. Finally, the signal expression will be combined with the MTF terms and the rms noise to yield the complete signal-to-noise expression. A glossary of variables is also included.

IV.2. MTF TERMS

(U) The modulation transfer function, or MTF, describes the amplitude response of a system or device to a sine wave input of a given frequency. In equation form,

$$\tau(K) = \frac{M_o(K)}{M_i(K)} , \qquad (1)$$

where

$\tau(K)$ is the MTF at spatial frequency K,

$M_o(K)$ is the modulation at the output at spatial frequency K

$M_i(K)$ is the modulation of the input at spatial frequency K.

Since the MTF is a simple ratio of modulation amplitudes, the MTF of a system composed of many components is simply the product of the MTFs of the individual components.

The modulation of a sine wave signal on top of a DC offset is given by

$$M_o = \frac{E_{max} - E_{min}}{E_{max} + E_{min}} , \qquad (2)$$

where E_{max} is the peak value of the sine wave, and E_{min} is the minimum value (offset) of the sine wave.

A graphical representation of these values is shown below.

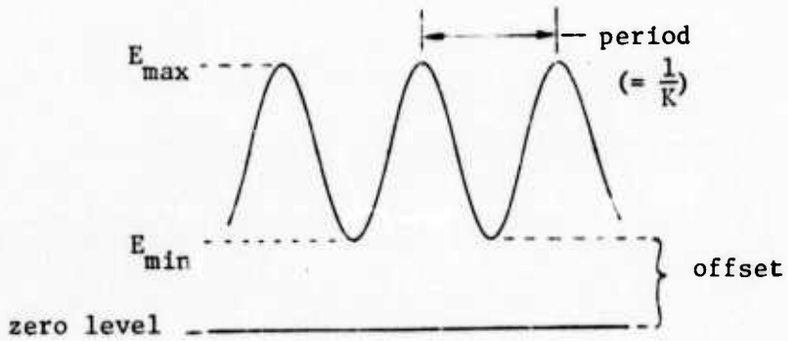

The various MTF terms comprising the total system MTF will be described in the paragraphs that follow.

IV.2.1 Image Motion MTF

(U) The image motion MTF is due to the shifting of the scene light over the photocathode surface. This can be due to telesccpe tracking errors, mount vibration, image mapping errors, or atmospheric refraction. The MTF is different depending on whether the image motion is linear, parabolic, sinuscidal or random. An equation for the MTF due to each type of motion is given below[2].

Linear Motion MTF is given by

$$\tau(K) = \frac{\sin(\pi AK)}{\pi AK} \tag{3}$$

where A is the magnitude of the image motion and K is the spatial frequency.

Parabolic Motion MTF is given by

$$\tau(K) = \frac{1}{2\sqrt{AK}} \left[\int_0^{2\sqrt{AK}} \left[\cos\left(\frac{\pi}{2} x^2 \right) + \sin\left(\frac{\pi}{2} x^2 \right) \right] dx \right]^{\frac{1}{2}} \tag{4}$$

where A and K are already defined, and x is a dummy variable used in the integration.

Sinusoidal Motion MTF is given by

$$\tau(K) = J_o\ (\pi AK) \tag{5}$$

where

$$J_o(x) = \frac{1}{\pi} \int_0^{\pi} \cos\ (x \sin \theta) d\theta \tag{6}$$

is the zero-order Bessel function, and A and K are already defined. Here, however, A represents the peak-to-peak amplitude of the sinusoidal motion.

Random Motion MTF is given by

$$\tau(K) = e^{-2(\pi AK)^2} \tag{7}$$

where A and K are already defined, and A is the rms amplitude of the random motion.

The image motion MTF term used in the model may be only one of the above terms or the product of two or more of the terms, depending on the amplitude and waveform of each component of image motion. For instance, the telescope mount vibration might be sinusoidal with some amplitude, while the tracking error might be linear with a different amplitude. In this case, the total image motion MTF due to both of these terms would be the product of equations (5) and (3), with the proper amplitude in each case.

IV.2.2 Scene Modulation

(U) The Scene Modulation is due to the contrast ratio of the light received from the scene. It assumes that this light is sinusoidal, although this is rarely the case, especially in the Teal Amber I application. However, the resulting error is usually justified by the simplicity of the MTF calculations. The contrast ratio of the light from the scene is given by

$$C_R = \frac{E_{max}}{E_{min}} \tag{8}$$

where E_{max} and E_{min} are defined in equation (2). The scene modulation is then given by

$$\tau_{scene} = \frac{C_R - 1}{C_R + 1} \tag{9}$$

IV.2.3 Image Section MTF

(U) The analytical expression for the MTF of the image section is too complicated to use in this model. A table of experimental values will be used instead.

IV.2.4 Telescope MTF

(U) The analytical expression for the MTF of the telescope is also too complicated to use in this model. A table of values for a particular telescope, or the MTF of a diffraction-limited lens can be used instead. The equation for the lens MTF is given below[3].

$$\tau_{lens} = \frac{2}{\pi}\left[\cos^{-1}\left(\frac{\pi K}{b}\right) - \left(\frac{\pi K}{b}\right)\sqrt{1 - \left(\frac{\pi K}{b}\right)^2}\right] \tag{10}$$

where

$$b = \frac{\pi D}{F\lambda} \tag{11}$$

D is the aperture diameter,

F is the focal length,

λ is the wavelength

K is the spatial frequency

In this case, however, the calculated MTF for the particular telescope will be used.

IV.2.5 Target MTF

(U) The MTF of the Silicon Dioxide storage target in the electrostatic camera has been derived by Knittman[4]. It is given below.

$$\tau_{target} = \frac{1 - e^{-4\pi Kt}}{4\pi Kt}\left[\frac{2k}{(k+1) + (k-1)e^{-4\pi Kt}}\right] \tag{12}$$

where

K is the spatial frequency

k is the dielectric constant

t is the dielectric thickness.

IV.2.6 Read Beam MTF

(U) The MTF of the read beam can be calculated assuming that the intensity distribution of the beam is Gaussian[3]. The expression for the MTF is then the Fourier transform of the Gaussian distribution,

$$\tau_{\text{read beam}} = e^{-2(\pi K\sigma)^2} \tag{13}$$

where σ is the standard deviation of the beam. For this study, it has been assumed that the diameter of the read beam spot is equivalent to 4σ.

IV.3 INPUT PARAMETERS

(U) The Teal Amber inputs are usually given in terms of equivalent stellar visual magnitudes, which must be converted to exposure in electrons per pixel before they can be input to the model. This is done by comparing the visual magnitude of the object (or background) to that of the sun over the spectral range of interest. The resulting intensity in watts per square centimeter is then multiplied by the area of the collecting aperture and optics transmission to get the total watts, and then converted from watts to electrons per pixel. This is shown below.

$$n_T = C_T\left(\frac{\pi}{4} D_c^2\right) t_o \left(\frac{d_{bc}}{v_T}\right)\left(\frac{R_p}{e}\right) \tag{14}$$

where

$$C_T = 74.2 \times 10^{-3} \cdot t_A \cdot 2.512^{(-26.7 - m_{v_T})} \tag{15}$$

and

n_T is the number of target electrons per pixel

m_{v_T} is the visual magnitude of the target

t_A is the atmospheric transmission

C_T is the watts/cm^2 given off by the target

D_c is the collecting aperture diameter

t_o is the transmission of the optics

d_{bc} is the optics blur circle diameter

v_T is the target velocity

R_p is the photocathode responsivity

e is the electron charge.

If the term $\frac{d_{bc}}{v_T}$ is larger than the exposure time, it should be replaced by the exposure time T_e.

In a similar manner, the number of background electrons per pixel can be calculated given the background visual magnitude per unit of solid angle (usually square arc-seconds).

$$n_B = C_B\left(\frac{\pi}{4} D_c^2\right)\left(\frac{\pi}{4} d_{bc}^2\right)\ t_o\ \left(\frac{R_p}{e}\right)\ T_e \tag{16}$$

where

$$C_B = 74.2 \times 10^{-3} \cdot t_A \cdot 2.512^{(-26.7 - m_{v_B})} \tag{17}$$

and

n_B is the number of background electrons per pixel,

C_B is the watts/cm^2/$\widehat{\text{sec}}^2$ given off by the background,

T_e is the exposure time.

The rest of the parameters are identical to those in the previous expression for n_T.

IV.4 SIGNAL TERM

(U) The input signal current from a scene with infinite contrast is given by

$$I_{scene} = 2\varepsilon M_k G_t Q_D \tag{18}$$

where

$$M_k = \frac{G_m m \delta_t I_b}{C^*} \tag{19}$$

$$Q_D = \frac{(n_T/2 + n_B)e}{A_P} \tag{20}$$

and

M_k is a multiplying factor,

Q_D is the average input charge density

ε is the return beam collection ratio,

G_t is the storage tape gain,

G_m is the electron multiplier gain,

m is the slope of the readout characteristic,

δ_t is the secondary emission ratio of the storage tube,

I_b is the read beam current,

C^* is the capacitance per unit area of the storage tape,

n_T is the number of target electrons per pixel

n_B is the number of background electrons per pixel

e is the electron charge

A_p is the pixel area

This signal term must also be modified by the MTF terms to get the actual output signal.

IV.4.1 Output Signal Calculation

(U) The signal remaining at the output of the camera is the product of the input scene current, the scene modulation, and the MTF terms of the camera components at the frequency of interest.

$$I_{signal} = \tau_{\substack{image \\ motion}} \tau_{target} \tau_{\substack{image \\ section}} \tau_{\substack{read \\ beam}} \tau_{telescope} \tau_{scene} I_{scene} \qquad (21)$$

IV.5 NOISE TERMS

(U) The major noise terms affecting the camera output are the scene noise, dielectric noise, read beam noise, thermal noise and amplifier noise. Each of these will be considered separately.

IV.5.1 Scene Noise

(U) The scene noise, or quantum noise, is due to the rms fluctuations in the input signal and the randomness of the target gain process. The current at the output due to this noise is given by

$$I_{scene} = \left[\frac{2\epsilon^2}{A_p^2} M_k^2 \beta^2 (G_t+1)(\sigma G_t A_p C_D) \right]^{\frac{1}{2}} \quad (22)$$

where

$$\beta = \frac{1}{K} \int_0^K |\tau_{target}(K)\ \tau_{read\ beam}(K)|^2\ dK \quad (23)$$

is a noise correction factor described by Schade[5], and the other variables were previously described in Section IV.

IV.5.2 Dielectric Noise

(U) This noise is due to the target charging during readout. The equivalent current at the output due to the dielectric (or target) noise is

$$I_{dielectric} = \left[\frac{\epsilon^2}{A_p^2} M_k^2 \left(\frac{eI_b(1+(\kappa-2))\delta_t}{2B} \right) \right]^{\frac{1}{2}} \quad (24)$$

where

κ is a noise characteristic of the target[6],

B is the bandwidth,

and the rest of the terms have been previously described.

IV.5.3 Read Beam Noise

(U) This noise is due to the shot noise in the read beam, modified by the electron multiplier noise, the secondary emission noise of the dielectric, and the energy analyzer partition noise. The equivalent current is given by

$$I_{read} = \left[G_m^2 2eI_b B\left(\frac{\varepsilon a \delta_t}{\delta_m - 1}\right) + (a\varepsilon\delta_t)^2 + a^2\varepsilon^2(\kappa - \delta_t)\delta_t + a(1-a)\varepsilon\delta_t \right]^{\frac{1}{2}} \quad (25)$$

where

G_m is the electron multiplier gain

δ_m is the secondary emission ratio of the first dynode of the electron multiplier

a is the fraction of the return beam passing through the energy analyzer,

and the rest of the terms have already been described.

IV.5.4 FET Noise

(U) The preamplifier chosen for this sensor model incorporates a low-noise junction field effect transistor. The shot noise current due to the channel current of the FET is given by

$$I_{FET} = \left[\frac{8eI_F B^3 C^2}{g_m^2} \right]^{\frac{1}{2}} \quad (26)$$

where

I_F is the FET channel current

C is the shunt capacitance to ground

g_m is the FET transconductance

and the rest of the terms have previously been described.

IV.5.5 Thermal Noise

(U) The thermal noise current generated by the output load impedance of the sensor is given by

$$I_{thermal} = \left[\frac{4k_B TB}{R_L}\right]^{\frac{1}{2}} \quad (27)$$

where

k_B is Boltzmann's constant

T is the absolute temperature

R_L is the load impedance

B is the bandwidth.

IV.5.6 Total Noise Calculation

(U) The total noise due to each of the individual noise terms is the rms sum of these terms as shown below, where the quantum noise correction factor is calculated for the frequency of interest.

$$I_{total\ noise} = \left[I_{quantum}^2 + I_{dielectric}^2 + I_{read}^2 + I_{FET}^2 + I_{thermal}^2\right]^{\frac{1}{2}} \quad (28)$$

IV.6 SIGNAL-TO-NOISE RATIO CALCULATIONS

(U) The signal-to-noise ratio at the camera output is given by the ratio of the signal current in equation (21) to the total noise current in equation (28),

$$SNR = \frac{I_{signal}}{I_{total\ noise}} \tag{29}$$

This can be compared to the quantum-limited signal-to-noise ratio available at the input to get a quantitative measure of the amount of signal degradation and noise introduced by the camera. The quantum-limited signal-to-noise ratio is given by

$$SNR_{Q.L.} = \frac{n_T}{\sqrt{n_T + n_B}} \tag{30}$$

where n_T and n_B are the numbers of target and background electrons, respectively.

The camera signal-to-noise ratio can be improved by altering the size of the read beam with respect to the pixel size. As the read beam diameter decreases, the effective camera signal-to-noise ratio increases due to the area correlation in the output signal. This increase in the signal-to-noise ratio is shown below:

$$SNR_{eff.} = \frac{I_{signal}}{I_{total\ noise}} \sqrt{\frac{4A_p}{\pi d^2}} \tag{31}$$

where A_p is the pixel area and d is the diameter of the read beam.

However, the effect of decreasing the read beam diameter is often offset by consequent increases in the bandwidth and the beam current.

IV.7 EQUIVALENT INPUT NOISE

(U) It is sometimes desirable to equate the noise current at the output of the camera to an equivalent number of "noise" photoelectrons at the photocathode. A simplified calculation of this can be performed by examining how the camera degrades the quantum-limited signal-to-noise ratio. Referring to equation (30), the signal term is degraded by all the MTF terms (except the scene modulation), while the noise term is increased by the equivalent number of noise photoelectrons. This is shown below.

$$SNR_{\substack{\text{camera}\\\text{output}}} = \frac{\tau_{system} n_T}{\sqrt{n_T + n_B + n_N}} \qquad (32)$$

where

$$\tau_{system} = \tau_{\substack{\text{image}\\\text{motion}}} \tau_{target} \tau_{\substack{\text{image}\\\text{section}}} \tau_{\substack{\text{read}\\\text{beam}}} \tau_{telescope},$$

and the SNR is given in equation (31).

Thus, to find the number of equivalent noise electrons at the photocathode, use equation (31) to get the signal-to-noise ratio at the camera output, and then solve equation (32) for n_N.

IV.8 CAMERA NOISE BANDWIDTH

(U) In order to be able to find the total noise by taking the rum sum of the individual noise terms, each of the terms must have a normal distribution. This represents white noise, where the noise power per unit bandwidth is constant. Although not all of the noise terms have a normal distribution, such as the scene noise, for example, it is close enough for this type of calculation. Hence, the noise bandwidth is limited only by the transfer processes that follow each noise source.

IV.9. GLOSSARY

(U) A complete listing of the parameters used in the analytical model is given below.

PARAMETER	DESCRIPTION	UNITS
a	energy analyzer transmission	-
A	image motion magnitude, eq. (3) - eq. (7)	-
A_p	pixel area	cm^2
b	product of terms, eq. (10)	-
B	bandwidth	Hz
C	FET shunt capacitance	Farad
C*	Target capacitance per unit area	F/cm^2
C_B	background irradiance	$watts/cm^2/\widehat{sec}^2$
C_R	contrast ratio, eq. (8)	-
C_T	target irradiance	$watts/cm^2$
d	read beam diameter	μm
d_{bc}	telescope blur circle diameter	$\widehat{sec}$
D_c	collection aperture diameter	inches
e	electron charge	1.6×10^{-19} coul.
F	telescope focal length	inches
g_m	FET transconductance	mhos
G_m	electron multiplier gain	-
G_t	target gain	-
I_b	read beam current	amps
I_F	FET channel current	amps
k	target dielectric constant	3.8

PARAMETER	DESCRIPTION	UNITS
k_B	Boltzmann's constant	1.38×10^{-23} J/°K
K	spatial frequency	lp/mm
m	readout slope	amp/amp/volt
M_K	multiplying factor, eq. (19)	-
n_B	number of background electrons, eq. (16)	-
n_T	number of target electrons, eq. (14)	-
Q_D	input charge density, eq. (20)	coul/cm^2
R_L	camera load resistance	ohms
R_P	photocathode responsivity (S-20)	amp/watt
t	target thickness	angstroms
t_a	atmospheric transmission (average)	-
t_o	optics transmission	-
T	absolute temperature	°Kelvin
T_e	exposure time	seconds
v_T	target velocity	arc-sec/sec
β	noise correction factor, eq. (23)	-
δ_m	electron multiplier secondary emission ratio	-
δ_t	target secondary emission ratio	-
ε	return beam collection ratio	-
κ	target noise characteristic	-
λ	wavelength of light through lens	angstroms
σ	standard deviation of the beam	-

PARAMETER	DESCRIPTION	UNITS
$\tau_{\text{image motion}}$	image motion MTF, eq. (3) - eq. (7)	-
$\tau_{\text{image section}}$	image section MTF (at 11 lp/mm)	-
τ_{lens}	lens MTF, eq. (10)	-
$\tau_{\text{read beam}}$	read beam MTF, eq. (13)	-
τ_{scene}	scene modulation, eq. (9)	-
τ_{target}	target MTF, eq. (12)	-
$\tau_{\text{telescope}}$	telescope MTF (at 11 lp/mm)	-

REFERENCES

1.) R. Botticelli, R. Johnson, J. Wallmark, "The Applicability of Frame Imaging from a Spinning Spacecraft", NASA CR 114637, June 30, 1973, pp. 209 ff.

2.) Milton D. Rosenau, Jr., "Image-Motion Modulation Transfer Functions", Perkin-Elmer Corp. symposium on March 6, 1963.

3.) Niels Jensen, "Optical and Photographic Reconnaissance Systems", John Wiley and Sons, 1967, pp. 73-76.

4.) Irwin Krittman, "Resolution of Electrostatic Storage Targets", IEEE Trans. on Electron Devices, Vol. ED-10, No. 6, Nov. 1963, pp. 404-409.

5.) Otto H. Schade, "Resolving Power Functions and Integrals of High-Definition Television and Photographic Cameras - A New Concept of Image Evaluation", RCA Review, Vol. 32, December 1971.

6.) G. W. Timm and A. Van der Ziel, "Noise in Various Electron Multiplication Methods Used in Imaging Devices", IEEE Trans. on Electron Devices, Vol. ED-15, No. 5, May 1968, pp. 314-320.

7.) R. Botticelli, R. Johnson, J. Wallmark, op. cit., pp. 47-48.

APPENDIX V

ASTRONOMICAL DATA AND CONVERSION FACTORS

Visual magnitude of sun	$-26.7\ m_v$
Total solar irradiance (outside atmosphere)	.1353 Watts/cm^2
Solar irradiance between 300 and 800 nm (outside atmosphere)	74.16×10^{-3} W/cm^2
Solar irradiance between 300 and 800 nm (at sea level)	44.17×10^{-3} W/cm^2
Atmospheric light transmission, 300 to 800 nm	0.60

1 sphere =	4π steradians
1 steradian =	4.2545×10^{10} square arc seconds ($\widehat{sec}^2$)
1 radian =	57.296 degrees
1 degree =	60 minutes of arc
1 minute of arc =	60 arc-seconds
1 nautical mile (nmi) =	1852 meters
1 statute mile =	1609 meters
1 meter =	39.37 inches
1 micron (μ) =	10^{-6} meters
1 nanometer (nm) =	10^{-9} meters
1 Angstrom ($\mathring{A}$) =	10^{-10} meters
1 electron charge =	1.602×10^{-19} Coulombs